2002

Buffer layers for YBCO superconducting films on single crystal YSZ substrates and cubic textured Ni substrates

Dongqi Shi
University of Wollongong

Buffer layers for YBCO superconducting films on single crystal YSZ substrates and cubic textured Ni substrates

A thesis submitted in fulfillment of the requirements for

the award of the degree of

Doctor of Philosophy

from

University of Wollongong

By

Dongqi Shi, M. Sc.

Institute for Superconducting and Electronic Materials

Faculty of Engineering

2002

Candidate's Certificate

This is to certify that the work presented in this thesis is original and it was carried out by the candidate in the laboratories of Institute for Superconducting and Electronic Materials at the University of Wollongong, NSW, Australia, and has not been submitted for a degree to any other institution of higher education.

Dongqi Shi

Acknowledgement

I would like to express my deep gratitude to my supervisors, Professor S. X. Dou and Dr. M. Ionescu for their professional guidance and moral support during this project. I would like to thank the Department of Training and Youth Affairs of Australia, the University of Wollongong and the Institute for Superconducting and Electronic Materials for offering me the OPRS scholarship and the Postgraduate Awards.

I wish to thank Professor H. K. Liu and Professor W. M. Chen for their valuable advices. Thanks to Mr. J. McKinnon, my classmate, for good cooperation and valuable discussion. Also, special thanks are given to Dr. Tania Silver for providing great help in proofreading my papers and this thesis.

I am grateful to all members of the Institute for Superconducting and Electronic Materials, as well as all members of the Department of Materials Engineering.

Finally, I wish to thank my wife, Lin Lu for her encouragement, patience and support, my mother-in-law Suzhen Jin for her support in my home, and my son Weizhi Shi for bringing me a great deal of happiness during this work.

Content

Objective of the Thesis

The objective of this thesis was to study buffer layers for YBCO superconducting thin films on single crystal substrates and coated conductors. Two kinds of buffer layers were chose in this research: CeO_2 film and NiO film. Different from other majority researchers who mainly concerned about the texture of buffer layers, this thesis made a contribution in the relationship of buffer layer texture, surface morphology and growth process. This work is very helpful to fully understand and accurately control the growth process of buffer layers.

The study of CeO_2 films on YSZ single crystal substrates was focused on the four aspects: deposition conditions; orientation and crystallization (including out-of-plane orientation, in-plane orientation, and crystallization); surface morphology (including surface topography, outgrowth on surfaces, and roughness); and growth modes. This thesis tried to give a clear picture and a relatively complete theory of the growth modes of CeO_2 thin films.

Some fundamental studies have been done to deposit buffer layers of CeO_2 and YSZ on cubic textured Ni substrate for fabricating coated conductors. The purpose of these works is to obtain the optimum deposition conditions through serial experiments. Addition to these works, the surface morphology including the microcracks and surface roughness which have significant effects on coated conductors was analyzed.

Abstract

The aim of this thesis was to study buffer layers for YBCO superconducting thin films on single crystal substrates and coated conductors. The work was divided into two parts: CeO_2 films on single crystal yttrium stabilized zirconia (YSZ) substrates; and CeO films and NiO films on cubic textured Ni substrates.

In the first part, the focus was on a deep understanding of the growth processes and mechanisms of CeO_2 films in order to better control the film properties, such as crystallinity, orientation, and surface morphology. The systematic study of CeO_2 films deposited by the pulsed laser deposition (PLD) on YSZ substrates has shown that the degree of a c-axis orientation is related to the morphology of the CeO_2 grains; the more spherical the shape of the grains is, the better the c-axis orientation and the smoothness of the CeO_2 film surface are. This correlation appears to be an intrinsic feature of the CeO_2 film, independent of the type of substrate or the deposition method.

By studying the orientation and the surface morphology of CeO_2 films deposited at different temperatures, the relationship between epitaxial quality and growth mode could be analysed. The optimum epitaxial growth of a CeO_2 film is layer-by-layer growth from the beginning to the end. The lower quality epitaxial growth is layer-by-layer and then island growth, and the growth mode of an imperfectly c-axis oriented film is island growth throughout. As the islands grow larger and become large outgrowths, the outgrowths prefer to connect to each other to form a network on the

surface. For a low quality CeO_2 film which was far from epitaxial, the growth of the film was characterized by the typical terrace-ledge-kink growth mode of cubic crystal.

The effects of an Ar + 10% H_2 atmosphere on the CeO_2 films were investigated. The Ar + 10% H_2 atmosphere used for deposition can enlarge the epitaxial temperature range, and furthermore, significantly reduce the epitaxial temperature. Pure c-axis oriented CeO_2 films were obtained with substrate temperatures between 350°C and 775°C using an Ar+10%H_2 atmosphere. At the same time, the surface roughness and the number of larger outgrowths were decreased compared to using an O_2 atmosphere. There is a reason to believe that the mobility of the species during deposition of a CeO_2 film is smaller using Ar + 10% H_2 than using O_2.

In the second part, the research relates to CeO_2 and NiO buffer layers which were employed in coated conductors. The Ar + 10% H_2 reducing gas was chosen in the deposition of CeO_2 films by PLD on the cubic textured Ni. The optimum deposition conditions are: deposition temperature 395°C; pulsed laser at 3Hz and 500mJ; Ar + 10% H_2 pressure of 100mTorr. The substrate-target distance is also an important parameter for the epitaxial growth of CeO_2 films. The optimum out-of-plane and in-plane textures as evaluated by the FWHMs of an XRD ω-scan and a ϕ-scan of for optimum CeO_2 film are 4.9° and 12° respectively. ϕ-scans of the CeO_2 film and the underlying Ni substrate showed that the growth of the CeO_2 film on the cubic textured Ni (100) substrate is in agreement with near-coincidence site lattice match modes, e.g. <110> CeO_2//<100>Ni. Some modifications have been made to eliminate the microcracks in CeO_2 films. The deposition procedure of first depositing CeO_2 film up to 10nm at 3Hz,

then depositing CeO_2 film at 1Hz up to 100nm can reduce the density of cracks and make the cracks narrow.

Three atmospheres, air, flowing oxygen, and flowing Ar +8%O_2, were used to fabricate biaxially textured NiO films by the surface oxidation epitaxy(SOE). The optimum deposition process is in flowing oxygen (P_{O2}~ 1 atm) at an oxidation temperature of 1075°C for 10min. NiO films have strong c-axis and a-b plane orientations, and the degree of the c-axis orientation is about 98%. XRD pole figures and ϕ-scans were used to investigate the a-b plane texture, and the FWHM value of a ϕ-scan for the (111) peak of an optimum NiO film was 12°. The morphologies and microdefects of NiO films were systematically investigated. The more (100) oriented the grains are, the smoother the surface of the NiO films is. The high roughness of NiO film can also be caused by clusters of relatively large NiO grains which form numerous circular spots on the surface of the NiO film. Decreasing the thickness of NiO films by shortening the oxidation time can reduce the density of these coarse spots on the surface of the NiO films.

List of Figures

List of Tables

Chapter 1. Introduction

Since the discovery of the first high-temperature superconductor (HTS) by Bednorz and Müller in 1986 [1], significant efforts have been made world-wide to realize the potential for practical applications offered by these materials. However, it has been found that the work of fabricating HTS materials into useful forms with acceptable superconducting properties is a daunting task due to the intrinsic properties of these ceramic oxides. Two major problems related to these properties are weak links at the grain boundaries and the creep of the magnetic flux lines.

The early studies of critical current density in HTS materials revealed that supercurrent transport across grain boundaries for a polycrystalline material is much lower than that for a single crystal because HTS materials have extremely small coherence lengths. These atomic-sized coherence lengths cause most high-angle grain boundaries to act as Josephson-coupled weak links. The weak links caused by the large-angle ($\geq 10°$) grain boundaries heavily degrade the critical current density through the boundaries and, moreover, determine its dependence on applied magnetic field and temperature. A strongly magnetic-field-dependent J_{ct} can be decreased by more than an order of magnitude in even weak fields of a few millitesla [2]. So controlling the grain boundary misorientation is important for fabricating high-J_c HTS materials, regardless of whether they are formed into thin film, wire or bulk.

HTS materials constitute a broad basis for technological applications, with an emphasis on electronic devices and superconducting wire. For HTS electronic devices, HTS thin

films with high-quality superconducting properties must have correct stoichiometry of elements, proper phases, a highly aligned texture, and a suitable oxygen concentration. Moreover, the surface of HTS thin films is another important factor in microwave applications that require a small microwave surface resistance R_s. HTS thin films are mostly made from $ReBa_2Cu_3O_{7-\delta}$ materials (Re = Y or rare earth element, typical transition temperature T_c = 90-95 K). Typical candidate substrates for $YBa_2Cu_3O_{7-\delta}$ (YBCO) films are $LaAlO_3$, $SrTiO_3$, MgO and yttrium stabilized zirconia (YSZ). Even though the YBCO films on $SrTiO_3$, MgO and $LaAlO_3$ have suitable superconducting properties, it is still highly desirable and even necessary for some applications to deposit an YBCO film on particular substrates, such as Si, GaAs and Al_2O_3, which have low dielectric constants and losses, high mechanical strengths, large size, or lower costs. However, the deposition of an YBCO film on these substrates requires a buffer layer which makes a barrier between the substrate and the film, or improves the lattice match, or makes a template plane for growing a film with a desirable orientation.

One of the most important steps towards the development of conducting wires was the fabrication of high-J_c Bi-based tapes (BSCCO) by using a silver-sheathed, powder-in-tube (PIT) technique [3]. Several manufacturers can now fabricate kilometer lengths of $Bi_2Sr_2Ca_2Cu_3O_{10}$ or Bi-2223 tapes with critical currents greater than 50 A and with an engineering current density (J_e) above 10000 A/cm^2 at 77 K and zero magnetic field [4]. These Bi-based conductors, however, have intrinsically weak pinning properties, precluding operation in substantial magnetic fields at liquid nitrogen temperature. Applications of these superconductors have been limited to those areas where operations are conducted at 35 K and in a magnetic field of 1 T, or at 65 K in a field of

~0.1 T [5]. Moreover, unless the amount of Ag can be substantially reduced, the cost of Bi-2223 tapes will remain high.

YBCO superconductor has a higher irreversibility field compared to BSCCO and thus behaves better than BSCCO in the presence of a magnetic fiel, so YBCO coated conductors can give a very attractive alternative to BSCCO tapes. Instead of using ceramic substrates, metallic substrates are used for YBCO coated conductors in order to obtain flexible tapes. The problems for fabrication of YBCO films on metallic substrates are almost the same as on single crystal substrates; it is necessary to have a biaxially texture for a high quality YBCO superconducting film. The YBCO coated conductors can be fabricated by successively forming a thin buffer layer such as CeO_2, YSZ, or MgO, then a relatively thick YBCO superconducting film on a metallic tape, usually a Ni alloy. Two competing methods for fabricating coated conductors have recently been developed [4]: one is the ionised beam-assisted deposition (IBAD) process with the main architectures of YBCO/YSZ/Ni-alloy (no biaxial texture) and YBCO/CeO_2/YSZ/Ni-alloy (no biaxial texture); another is the rolling-assisted biaxially textured substrate (RABiTS) process with the main architectures of YBCO/CeO_2/YSZ/CeO_2/(biaxially textured Ni or Ni-alloy) and YBCO/YSZ/CeO_2/(biaxially textured Ni or Ni-alloy).

The buffer layers play an important role in both HTS thin films and coated conductors. CeO_2 film has proven to be one of the most effective buffer layers because of its favourable thin film growth characteristics, small chemical interaction and good lattice match with most HTS materials. As a buffer layer, CeO_2 film should have the proper

orientation, a high crystallisation and a smooth surface. In most cases, CeO_2 films are required to be epitaxial. Currently, research on CeO_2 films has commonly just focused on the relationship between orientation and deposition conditions [6, 7, 8]. There are only a few reports that involve in depth studies of the relationship between orientation, surface morphology, and growth modes of CeO_2 films [9]. In fact, all the properties of CeO_2 films such as the orientation, the crystallinity, and the surface morphology are decided by the growth modes, as well as the deposition conditions. In this thesis, the study of CeO_2 films was focused on four aspects: deposition conditions; orientation and crystallization (including out-of-plane orientation, in-plane orientation, and crystallization); surface morphology (including surface topography, outgrowth on surfaces and roughness); and growth modes. The reason why YSZ substrate was chosen as a substrate material is that the relationship between the deposition temperature and the epitaxial quality of CeO_2 films can be studied because of a relatively wider range of epitaxial temperatures on YSZ. This thesis makes a contribution to the relationship between the orientation, the surface morphology and the roughness, and the growth modes of CeO_2 films.

Typically, CeO_2 films used as buffer layers on single crystal substrates are deposited using an O_2 atmosphere [10, 11]. However, for YBCO coated conductors, the RABiTS method uses a CeO_2 buffer layer deposited on a cubic textured Nickel in an Ar + 4-10% H_2 atmosphere to suppress the formation of NiO [12, 13]. To the best of my knowledge, other effects of an H_2 atmosphere on a CeO_2 film have not been reported. We deposited CeO_2 films on single crystal YSZ substrates under Ar + 10% H_2 and studied the influence of H_2 on the morphology and the orientation of the CeO_2 films.

Taking another approach, A {100}<001>NiO film can be positively utilised as a buffer layer for coated conductors on top of a cubic textured Ni. The surface-oxidation epitaxy (SOE) was invented by Matsumoto et al [14, 15]. This method is very simple compared with other methods, such as IBAD and RABiTS, and is useful for speeding up tape manufacturing because the SOE process installed in an electric furnace can easily and continuously form a biaxially textured NiO layer. The resultant simplicity and effectiveness make this method most advantageous for scaling up to long tapes. However, the J_c of coated conductors fabricated by SOE is still not as high as that attained by IBAD and RABiTS. The most important reason for this is that the NiO buffer layer is not good enough, especially with respect to the surface quality. In this thesis we investigated the thermal oxidation process in three atmospheres (air, flowing oxygen, and flowing Ar + 8% O_2) in order to achieve a highly biaxially textured NiO film on cubic textured Ni substrates. The surface morphology including the microcracks and surface roughness was analysed in detail.

This thesis is organised following: Chapter 2 is a literature review on HTS materials, HTS thin films, substrates, buffer layers, and coated conductors, and also gives some brief descriptions of the main thin film deposition methods; Chapter 3 is about the experimental system and characterization techniques employed in this thesis, with the emphasis on the pulsed laser deposition (PLD) and atomic force microscopy (AFM) techniques. A study of epitaxial CeO_2 films deposited on single crystal YSZ substrates was put into Chapter 4. The research was mainly focused on the surface morphology and growth modes of CeO_2 films. Following the CeO_2 films on YSZ substrates, Chapter

5 contains a study of CeO_2 films deposited by PLD on cubic textured Ni substrates in an Ar + 10% H_2 atmosphere. In Chapter 6, in addition to the PLD method for film deposition, the surface oxidation epitaxy (SOE) was used to form biaxially textured NiO films on cubic textured Ni substrates as buffer layers for coated conductors. This chapter not only deals with the optimum oxidation conditions, but also contains a detailed analysis of the morphologies and microdefects of NiO films. Finally, Chapter 7 gives the summary and the conclusions of this thesis. References follow each individual chapter.

Chapter 1. references

1. H.Kamerlingh Onnes, Leiden Communication 120b, 122b, 124c (1911).
2. R Wordenweber, Supercond. Sci. Technol. 12 (1999) R86.
3. N.Sonnenburg, A. S. Longo, M. J. Cima, B. P. Chang, K. G. Ressler, P. C. McIntyre, and Y. P. Liu, J. Appl. Phys. 74 (1993) 1027.
4. D. K. Finnemore, K. E. Gray, M. P. Maley, D. O. Welch, D. K. Christen, and D. M. Kroeger, Physica C 320 (1999) 1.
5. A. Goyal, D. P. Norton, J. D. Budai, M. Paranthaman, E. D. Specht, D. M. Kroeger, D. K. Christen, Q. He, B. Saffian, F. A. List, D. F. Lee, P. M. Martin, C. E. Klabunde, E. Hartfield, and V. K. Sikka, Appl. Phys. Lett. 69 (1996) 1795.
6. M. K. Wu, J. R. Ashburn, C. J. Torng, P. H. Hor, R. L. Meng, L. Gao, Z. J. Huang, Y. Q. Wang, and C. W. Chu, Phys. Rev. Lett. 58 (1987) 908.
7. Z. Z. Sheng and A. M. Hermann, Nature 322 (1988) 138.
8. H. Maeda, Y. Tanaka, M. Fukutomi, and T. Asano, Jpn. J. Appl. Phys., 27 (1988) 209.

9. Frank J. Owens and Charles P. Poole, Jr. The new superconductors, Plenum Press, New York and London,1996, p98.

10. S. R. Foltyn, R. E. Muenchausen, R. C. Dye, X. D. Wu, L. Luo, and D. W. Cooke, Appl. Phys. Lett 59 (1991) 1374.

11. B. F. Cole, G. C. Liang, N. Newman, K. Char, and G. Zaharchuk, Appl. Phys. Lett. 61 (1992) 1727.

12. A. Goyal, R. Feestra, F. A. List, M. Paranthaman, D. F. Lee, D. M. Kroeger, D. B. Beach, J. S. Morrell, T. G. Chirayil, D. T. Verebelyi, X. Cui, E. D. Specht, D. K. Christen, and P. M. Martin, JOM (1999) 19.

13. D. P. Norton, A. Goyal, J. D. Budai, D. K. Christen, D. M. Kroeger, E. D. Specht, Q. He, B. Saffian, M. Paranthaman, C. E. Klabunde, D. F. Lee, B. C. Sales, and F. A. List, Science, 274 (1996) 755

14. K. Maatsumoto, Y. Niiori, I. Hirabayashi, N. Koshizuka, T. Watanabe, Y. Tanaka and M. Ikeda, Advances in Superconductivity, Vol 10, ed K Osamura and I Hirabayashi (Tokyo:Springger 1998) 611.

15. K. Maatsumoto, S. B. Kim, J. G. Wen, I. Hirabayashi, T. Watanabe, N. Uno and M. Ikeda, IEEE Trans. Appl. Supercond. 9 (1999)1539

Chapter 2. Review of high-T_c thin films, buffer layers, substrates, and coated conductors

2.1. Development of high temperature superconductors

In 1911, Onnes [1] discovered superconductivity, the ability of a material to carry electricity with no resistance, in mercury when it was cooled to below the critical temperature (T_c) of 4.2 K (Kelvin). In 1933 Meissner and Ochsenfeld [2] discovered the another intrinsic characteristic property of the superconducting state: a superconductor expels the magnetic field from its interior. This effect is called the Meissner effect, and it is independent of the property of zero resistivity. All of the superconductivity applications are based on these two characteristics of superconductors. During the next 75 years, the theory and applications of superconductivity were developed. Many techniques and devices such as powerful magnets built of superconducting materials for medical magnetic resonance imaging (MRI), high energy accelerators, and the very sensitive magnetic field detectors called Superconducting Quantum Interference Devices (SQUIDs) were achieved. However, because of the high cost and inconvenience of liquid helium refrigeration, large scale applications of superconductivty were not considered economically feasible.

In April 1986, Bednorz and Müller [3], researchers at IBM in Switzerland, discovered superconductivity in $(La\text{-}Ba)_2CuO_4$ with a T_c up to 35 K, in contrast to the previous record of 23 K, for which they were subsequently awarded the Nobel Prize. In February 1987, research groups from the University of Houston and University of Alabama, coordinated by Chu and Wu [4], discovered Y-Ba-Cu-O (YBCO) ceramics with T_c =

92K. This was the first superconductor was reported with a transition temperature above the boiling point of liquid nitrogen, which is a much cheaper coolant than liquid helium. Just one year later, bismuth- and thallium-based superconducting systems were discovered. In January 1988, Sheng and Hermann [5] of the University of Arkansas announced the discovery of a Tl-Ba-Cu-O material with T_c = 82K. The same group subsequently added Ca to the compound (TBCCO) and measured the T_c at 125K. At around the same time, Maeda et al [6] from Japan's National Research Institute of Metals announced that they had found at least two different phases in the Bi-Sr-Ca-Cu-O (BSCCO) system with T_c values of about 80K and 110K. These phases were identified as $Bi_2Sr_2Ca_1Cu_2O_8$ and $Bi_2Sr_2Ca_2Cu_3O_{10}$. Mercury-based compounds (HBCCO) were discovered in 1993, with temperatures up to 164 K under pressure. The most commonly and currently studied HTS materials with superconducting transition temperatures T_c above the temperature of liquid nitrogen are $ReBa_2Cu_3O_{7-\delta}$ (Re-123, Re = Y or rare earth element, typical transition temperature T_c = 90-95K), $Bi_2Sr_2Ca_1Cu_2O_8$ (Bi-2212, T_c = 90K), $Bi_2Sr_2Ca_2Cu_3O_{10}$ (Bi-2223, T_c = 120K), $Tl_2Ba_2Ca_1Cu_2O_8$ (Tl-2212, T_c = 110K), $Tl_2Ba_2Ca_2Cu_3O_{10}$ (Tl-2223, T_c = 127K, and $HgBa_2Ca_1Cu_2O_8$ (Hg-1212, T_c = 134K). All such materials belonging to the copper oxide family, many with critical transition temperatures above the boiling point of liquid nitrogen, were called high temperature superconductors (HTS). In contrast, the superconductors belonging to families discovered before 1986 are called low temperature superconductors. **Table 2.1** gives the list of high T_c superconductors.

Table 2.1. High-temperature superconductor transition temperature records since 1986 [7]

Material	T_c, K	Year
$Ba_xLa_{5-x}Cu_5O_y$	30 - 35	1986
$YBa_2Cu_3O_{7-\delta}$	91 - 93	1987
$Bi_2Sr_2Ca_2Cu_3O_{10}$	106 - 110	1988
$Tl_2Ba_2Ca_2Cu_3O_{10}$	125	1988
$Tl_2Ba_2Ca_2Cu_3O_{10}$ (at 7 GPa)	131	1993
$HgBa_2Ca_2Cu_3O_{8+\delta}$	133	1993
$HgBa_2Ca_2Cu_3O_{8+\delta}$ (at 25 GPa)	155	1993
$Hg_{0.8}Pb_{0.2}Ba_2Ca_2Cu_3O_x$	133	1994
$HgBa_2Ca_2Cu_3O_{8+\delta}$ (at 30 GPa)	164	1994

2. 2. Applications of HTS materials and thin films

Even though "the liquid nitrogen barrier" has been broken, many of the great promises of HTS superconductivity technology have not yet been realized. The difficulties with the materials can be attributed to a number of the materials science and engineering problems, e.g. making long HTS wire that can carry large currents without energy loss and can retain excellent superconducting properties over long periods of time without chemical and physical degradation. However, after intensive effort, year after year, commercial applications of HTS materials in fields such as electric power, transportation, electronics, and medicine are now appearing.

Since the discovery of the first high-temperature superconductor, significant efforts have been devoted to the research on high quality HTS films, such as good textured or

epitaxial films. These efforts are prompted largely by the potential applications of thin films in some cryoelectronic devices and by the possibility of studying new physical properties using these unique layered materials. **Table 2.2** lists potential applications of HTS thin films. These applications all require epitaxial HTS films.

Table 2.2. Applications of HTS thin films [8]

Phenomena	Devices	Applications
No resistivity for electrical current: high J_c	Strip lines, patterned layer structures	Passive microwave devices Interconnects in microelectronics
Josephson tunnelling	SQUIDS	In physical measurements: SQUIDS for detection of extremely small magnetic fields, magnetic susceptibilities and voltage measurements Medicine: magnetic encephalography
	Josephson devices	Computers: fast logic and memory circuits; Microwave detectors and mixers
Sharp resistive transition	Bolometer	Plasma and space physics: detection of far-infrared radiation (>20μm)radiation (>20μm)

2. 3. High temperature superconducting thin films

The difficulties in depositing high-quality HTS thin films are the result of a number of special properties of the HTS materials.

1. HTS materials have extremely small coherence lengths. For YBCO, ξ_c = 0.3 - 0.5 nm and ξ_{ab} = 2 - 3 nm, for Bi-2223, values of ξ_c = 0.02 - 0.04 nm and ξ_{ab} = 2 - 2.5 nm [9]. These atomic-sized coherence lengths result in the destruction of the superconducting connection by even very small structural perturbations. The principal problem relates to the supercurrent transport across grain boundaries, which limit the transport critical current density (J_{ct}) and determine its dependence on applied magnetic field and temperature. This problem arises because most high-angle grain boundaries act like Josephson-coupled weak links, due to the small coherence lengths. The weak links caused by the large-angle (≥10°) grain boundaries heavily degrade the critical current density through the boundaries and, more importantly, a strongly magnetic-field-dependent J_{ct} can be decreased by more than an order of magnitude in even weak fields of a few millitesla [10] .
2. The layered structure of HTS materials leads to a large anisotropy in most parameters, such as T_c, J_c, the critical fields (B_{c1} and B_{c2}), penetration depth (λ_L), and the coherence length (ξ) . **Table 2.3** lists the parameters of the anisotropy of HTS materials. In many applications a preferred orientation of thin film is needed for some applications. For example, c-axis YBCO films can be used in microwave applications because of the high J_c along the a-b plane, and a-

axis YBCO films are sometimes needed for the junction devices due to the longer coherence length along the a-b plane.

Table 2.3. The anisotropy of HTS materials [11]

HTS materials	$\Gamma = (\xi_{ab}/\xi_c)^2 = (\lambda_{ab}/\lambda_c)^2$
YBCO	2.5 - 29
BSCCO	3000 - 15000
TlBCCO	$\geq 10^5$

3. The superconducting properties strongly depend on the stoichiometry of HTS materials, especially on the oxygen concentration. The thermodynamic conditions for the formation of phase-pure HTS materials can be divided into two parts. The first part concerns the correct stoichiometry of the metallic constituents, and the second is related to the oxygen content and ordering. For $YBa_2Cu_3O_{7-\delta}$, at an oxygen deficiency $\delta<0.36$, Y-123 turns from a superconductor to an antiferromagnetic insulator. At higher oxygen deficiencies ($\delta\geq0.36$), the superconducting transition temperature increases, rises to a maximum of about 92K around $\delta = 0.88$ and decreases below 88K as $1\geq\delta>0.88$ [12].
4. There are some complex phases in the HTS materials. Even though the stoichiometry of the HTS materials is correct, a large content of the proper phases must also be achieved to obtain high superconducting quality; sometimes the pure phase is necessary. In this respect, BSCCO and TBCCO systems are more complicated than YBCO systems.

Overall, for most applications, epitaxial HTS films are required without large-angle grain boundaries, without secondary phases and out-growths, and with high critical current density J_c. Besides, the surface resistance of HTS thin films is another important factor in some applications that need a small microwave surface resistance R_s.

All cuprate superconductors have a layered structure. The flow of supercurrent takes place in the CuO_2 conduction layers, while the binding layers support and hold together the conduction layers. Various high T_c materials have different numbers of conduction layers. The number of CuO_2 layers decides the superconducting transition temperatures. **Table 2.4** lists the number of CuO_2 layers and superconducting transition temperatures for typical cuprates.

Table 2.4. Number of CuO_2 planes and superconducting transition temperatures of cuprates [13].

Formula	Number of CuO_2 planes		
	1	2	3
$(La_{0.9}Sr_{0.1})_2CuO_4$	35	—	—
$(Nd_{0.9}Ce_{0.1})_2CuO_4$	35	—	—
$Yba_2Cu_3O_7$	—	92	—
$Bi_2Sr_2Ca_{n-1}Cu_nO_{2n+4}$	—	84	110
$Tl_2Ba_2Ca_{n-1}Cu_nO_{2N+4}$	90	110	125
$HgBa_2Ca_{n-1}Cu_nO_{2n+2}$	95	122	133

For HTS cryoelectronic devices, the most successfully obtained and widely used superconducting film so far is YBCO film. The reason is that it is easier to make epitaxial YBCO films than with BSCCO and TBCCO because YBCO material has fewer elements in the compound and the phase diagram is simpler than for the other materials. **Fig.2.1** shows the unit cell of $YBa_2Cu_3O_{7-\delta}$.

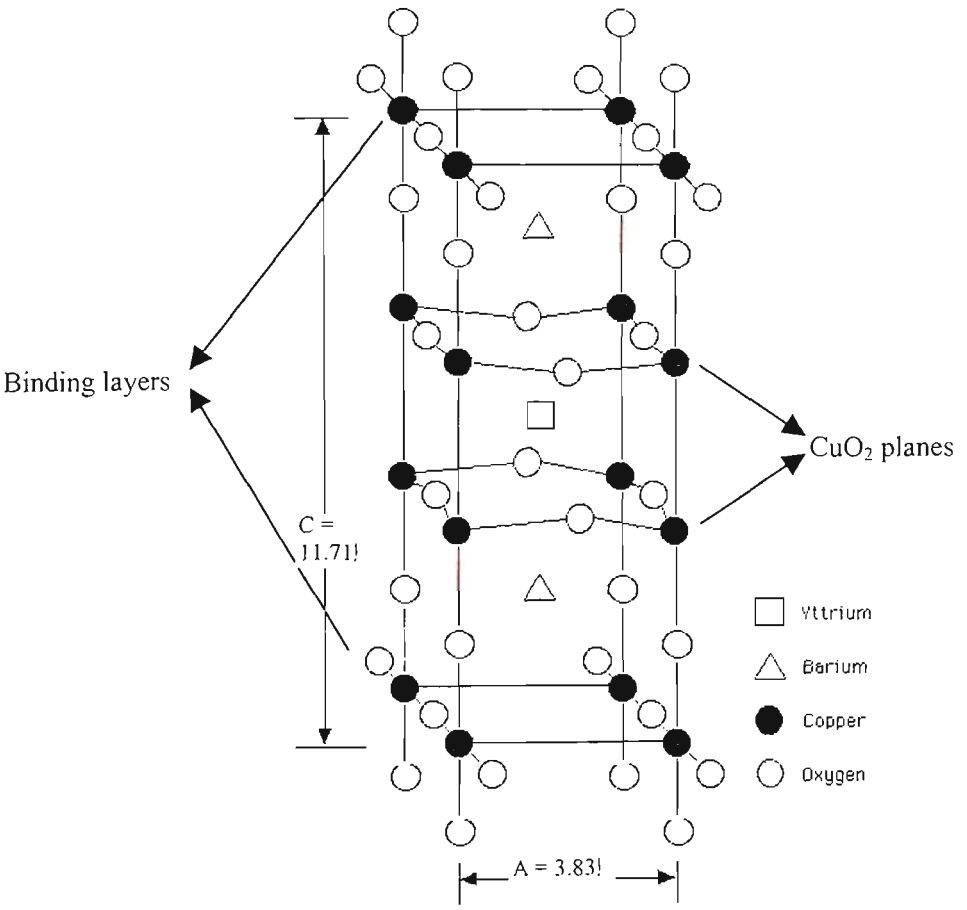

Figure 2.1. The unit cell of $YBa_2Cu_3O_{7-\delta}$[14].

YBCO films have been used for almost every application of HTS thin film, especially in microwave applications, Josephson junctions, and SQUIDs. For massive microwave applications, large-area YBCO superconducting films, two-sided as well in some cases,

are needed. Therefore much research has been done to enable the deposition of YBCO film on single crystal $LaAlO_3$, $SrTiO_3$, MgO, and YSZ substrates.

Large-area, two-sided YBCO films have been deposited on $LaAlO_3$ substrates [15]. YBCO films on 5-cm-diameter $LaAlO_3$ substrate have uniform transition temperatures of ≥90 K on both sides, with a critical current density of 2.5×10^6 A/cm^2. The surface resistance for samples cut from a 5cm wafer is 40-60 μΩ at 10GHz and 4K.

Furthermore, many efforts have been made to improve the quality of YBCO films on sapphire and Si substrates by using different buffer layers (such as CeO_2, YSZ, CeO_2/YSZ, and MgO) between YBCO and the substrates. B. F. Cole et al [16] have reported that YBCO films for microwave applications were deposited on 5-cm diameter M-plane $(10\bar{1}0)$ sapphire with an MgO buffer layer and on R-plane $(1\bar{1}02)$ sapphire with a CeO_2 buffer layer by off axis sputtering. R_s values of 450-620μΩ at 77K and 10GHz were measured across an entire 5-cm diameter YBCO film on M-plane sapphire. For YBCO on R-plane sapphire, R_s values at 77K and 10GHz were 950 μΩ for a whole wafer and 700 μΩ for 1×1 cm^2 samples.

Y. J. Tian et al [17] have prepared YBCO thin films by PLD on naturally oxidized 2 in diameter silicon wafers with CeO_2/YSZ buffer layers. The T_c is 87.5 - 88.2K, and J_c is 1.3MA/cm^2 (77K, 0T) over the whole wafer.

There are two routes for the deposition of HTS thin films: one is *in-situ* deposition; the other is *ex-situ* deposition. *In-situ* deposition means that the desired films are formed at the deposition temperature and do not need post-deposition treatment. The advantage of *in-situ* deposition is that the process is simple and the deposition temperature is lower than for *ex-situ* deposition. There is a significant benefit in using *in-situ* deposition to fabricate HTS film because avoiding the high temperature annealing step can reduce the reaction between the film and substrate, and produce films with good superconducting properties. The efficiency of *in-situ* deposition is higher than that of *ex-situ* deposition. The *in-situ* deposition route is used for the majority of YBCO and BSCCO film preparations.

The *ex-situ* route is widely used for TBCCO, and HBCCO films. Microcrystalline or amorphous films are deposited at very low temperature, even room temperature, in the *ex-situ* route. Superconducting properties are obtained by a following high temperature annealing step, usually in a special furnace. For example, TBCCO films can be formed by deposition of an amorphous precursor film on a room temperature or slightly heated substrate followed by annealing in oxygen and Tl_2O vapour [18]. *In situ* growth of TlBCCO films has only reported by a small number of groups [19].

Besides YBCO, other HTS compounds, especially Tl-2212, are also promising for certain microwave applications. Thin films of Tl-2212 have been used in applications ranging from passive microwave devices to active Josephson-effect devices. The fabrication of Tl-2212 thin films involves a delicate balance between the high

temperatures required to form the superconducting phases and the high volatility of thallium at these temperatures.

The intrinsic Josephson effect (IJE) due to the tunneling of the Cooper pairs between adjacent CuO_2 planes inside the highly anisotropic layered HTS materials was experimentally confirmed by Kleiner et al [20]. Intrinsic Josephson junctions (IJJs) in layered HTS materials such as Bi-2212 have many advantages over artificially fabricated multilayers. Much research has been aimed at depositing Bi-2212 films to make IJE applications.

Stoichiometry control is difficult in Bi-2212 film depositions due to its complicated phases compared to YBCO, and further complicated by the tendency of bismuth to evaporate at temperatures high than 500°C during fabrication. It is very difficult to fabricate high-quality Bi-2223 thin films. All these difficulties often yield films with low T_{c0} (< 77K) and broad transition widths (> 10K) [21].

2. 4. Substrates

For the deposition of high quality HTS thin films, the choice of the substrate material is of primary importance. The basic requirements for the substrates (only considering the quality of HTS superconducting films) can be summarized as following:

a. Crystallographic lattice match between HTS film and substrate;

b. Similar thermal expansivities of HTS thin film and substrate;

c. No chemical interaction at the interface between HTS thin film and substrate at the deposition or post-deposition treatment temperature.

Table 2.5 gives these characteristic parameters for the materials used as substrates for high T_c films.

Besides these essential requirements for obtaining high quality superconducting films, there are others requirements for substrates to be used in HTS thin film applications, such as:

d. Suitable polished surface;

e. stable and reasonably strong;

f. Size availability and low cost.

Table 2.6 gives other characteristic parameters of substrates for HTS applications. Depending on the individual applications of the films, some specific requirements are imposed on the substrate. For example, twinning of the substrates should be avoided for some applications. The dielectric properties are the crucial conditions on substrates for microwave applications.

Table 2.5. Lattice parameters and thermal expansion coefficients of the common substrates for the growth of superconducting thin films [22]

Material	Crystal structure	Lattice parameters (Å)	Thermal expansion (10^{-6}/K)
$LaAlO_3$	Rhombohedral	a = 5.36 c = 13.11	10
$SrTiO_3$	Cubic	a = 3.91	10.08
MgO	Cubic	a = 4.20	13.8
YSZ	Cubic	a = 5.16	10
$LaGaO_3$	Orthorhombic	a = 5.53 b = 5.49 c = 7.77	10.6
$NdGaO_3$	Orthorhombic	a = 5.42 b = 5.50 c = 7.72	11
Si	Cubic	a = 5.43	4.4
Sapphire	Rhombohedral	a = 4.76 c = 12.99	8.3
$Yba_2Cu_3O_x$	Orthorhombic	a = 3.83 b = 3.89 c = 11.71	14 12 25

Table 2.6. Properties of substrate materials for the preparation of YBCO thin films [22]

Substrate materials	Attainable dielectric properties		Twinning of crystallinity	Mechanical strength	Chemical stability	Available substrate size: diameter (mm)	Requirement of buffer layer
	ε	Tan δ at 10 GHz, 77K					
$LaAlO_3$	20.5 -27	7.6×10^{-6} - 3×10^{-4}	Yes	Good	Fair	100	No
$SrTiO_3$	300	~2×10^{-2}	No	Good	Fair	30-50	No
MgO	9.6 - 10	6.2×10^{-6}	No	Good	Poor	>30	Sometimes
YSZ	27-33	>10^{-4}	No	Good	Good	100	Sometimes
R-plane sapphire	9.4-11.6	10^{-8}	No	Good	Good	100	Yes
Si	11.7		No	Good	Good	300	Yes
$LaGaO_3$	25		Yes	Good	Fair	40	No
$NdGaO_3$	23	4×10^{-4}	No	Good	Fair	50	No

So the choice of substrate must be made depending on the applications of HTS films and all the relevant requirements should ideally be met, although in some situations a compromise is necessary.

Typical candidates are $LaAlO_3$, $SrTiO_3$, MgO and YSZ for high T_c film depositions. YBCO thin films grown on single crystal $LaAlO_3$ and $SrTiO_3$ substrates have a good lattice match between the films and the substrates (about 2% and 1.4% respectively) and

have a high critical current density of about 4 - 6×10^6A/cm^2 [23]. The drawbacks of $LaAlO_3$ and $SrTiO_3$ substrates are the difficulty in fabricating large area substrates and the fact that the cost per square millimetre is high. Moreover, $LaAlO_3$ substrate is prone to twinning in its crystal structure, and the strength is very low. The lattice mismatch between YBCO film and single crystal MgO or YSZ substrate is about 9% and 6% respectively, larger than for $LaAlO_3$ and $SrTiO_3$, but the J_c of YBCO films can still be more than 10^6A/cm^2 [24]. In fact, this J_c is large enough for most HTS thin film applications. The drawback of MgO [25] is that it is unstable in air and tends to deliquesce. YSZ substrate is easy to be made into a large size, and it is also strong. The cost of it is lower than for the others. But YSZ reacts with YBCO to form $BaZrO_3$ at the deposition temperature, which degrades the superconducting properties of the YBCO [26].

Even though the YBCO films on $SrTiO_3$, MgO, YSZ and $LaAlO_3$ have excellent or at least suitable properties that make them compatible with superconductivity of HTS thin films, the high dielectric constants and losses, low mechanical strengths, size limits, or high costs of some of these substrates have led to efforts to deposit YBCO thin films on other substrates such as Si and sapphire. The reaction between Si or the Al in sapphire with the YBCO at high temperatures is more serious than that between YSZ and YBCO, so it is impossible to directly deposit YBCO superconducting films on Si and sapphire substrates. This has been the main obstacle to large scale applications of YBCO thin films. Buffer layers must be used between HTS thin films and Si or sapphire substrates to solve this problem. The details will be given in section 2.5.

2. 5. Buffer layers

In HTS thin film deposition for various applications, the purposes of using buffer layers are to make a barrier between substrate and film, or improve the lattice match, or make a template plane to a film with a desirable orientation. Sometimes, a single buffer layer is good enough, but sometimes multi-buffer layers are necessary. **Table 2.7** shows the lattice mismatches and relative basal plane orientations between buffer layers and substrates. **Table 2.8** gives the buffer configurations investigated on single crystals with results for the uppermost layer.

Table 2.7. Lattice mismatches and relative basal plane orientations between buffer layers and substrates [27]

Substrate	Buffer layer			
	YSZ	CeO_2	$SrTiO_3$	$LaAlO_3$
Ni(100)	3.0% (45°)	7.9% (45°)	9.8% (0°)	7.0% (0°)
YSZ		5.0% (0°)	6.9% (45°)	4.1%(45°)
CeO_2	-5.3%(0°)		2.0 %(45°)	-1.%(45°)
$SrTiO_3$	-7.5%(45°)	-2.1%(45°)		-3.0 %(0°)

45° indicates the orientation where the (100) plane of buffer layers is parallel to the (110) plane of substrates.

0° indicates the orientation where the (100) plane of buffer layers is parallel to the (100) plane of substrates.

Table 2.8. Buffer layer configurations investigated on single crystal substrates with results for the uppermost layer [27]

Configuration	Result
CeO_2/YSZ	Biaxial texture
$SrTiO_3$/YSZ	Polycrystalline
$SrTiO_3$/ $LaAlO_3$	Biaxial texture
$SrTiO_3$ /CeO_2/YSZ	Biaxial texture
$LaAlO_3$/YSZ	Amorphous
$LaAlO_3$/$SrTiO_3$	Biaxial texture
$LaAlO_3$/CeO_2/YSZ	Amorphous
$LaAlO_3$/$SrTiO_3$/CeO_2/YSZ	Biaxial texture

2.6. CeO_2 film as buffer layer for HTS thin films

CeO_2 has proven to be one of the most effective buffer layers because of its favourable thin film growth characteristics, small chemical interaction and good lattice match with most HTS materials. CeO_2 has the cubic fluorite crystal structure with a = 5.411Å. **Fig. 2.2** shows the structure of CeO_2 [28]. It has a good lattice match with YBCO unit cells when rotated through 45° with respect to the a-b plane. CeO_2 thin films are used as a buffer layer or as part of multi-buffer layers. **Table 2.9** lists the configurations of multi-buffer layers which include CeO_2 film. CeO_2 films are usually deposited by using PLD, e-beam evaporation or rf Sputtering.

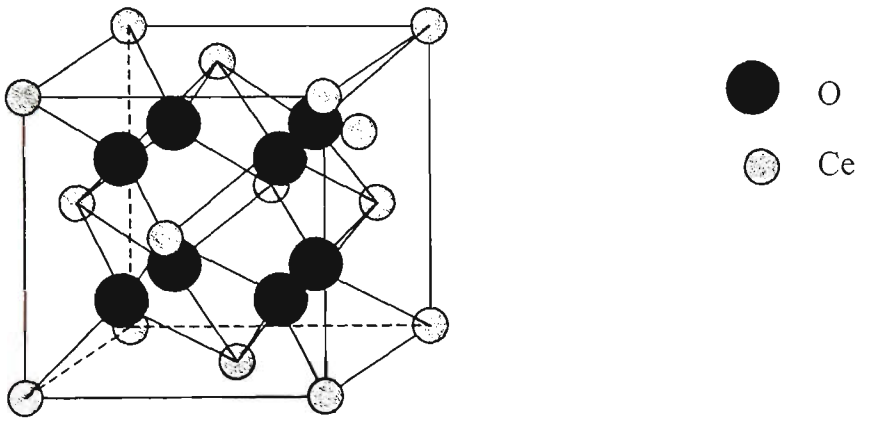

Figure 2.2. The structure of CeO_2.

Table 2.9. CeO_2 films as buffer layer or a part of multi-buffer layers

Buffer layer/substrate	Methods of CeO_2 deposition
CeO_2/Al_2O_3(1-102)	PLD [29-33]
CeO_2/Si (100)	e-beam evaporation [34,35], reactive DC sputtering[36,37]
CeO_2/YSZ(100)	all-coating-pyrolysis (All-CP) process[38],PLD [39,40, 41]
YSZ/CeO_2/Ni (cubic textured)	PLD[39,40, 41]
CeO_2/YSZ/ CeO_2/Ni (cubic textured)	PLD [40,42]
CeO_2/Eu_2O_3/Ni (cubic textured)	PLD[42]
CeO_2/YSZ/Eu_2O_3/Ni	rf sputtering [43]
CeO_2/YSZ/LNO/Ni	PLD[44]
CeO_2/YSZ/CeO_2/Ni-Cr alloy	e-beam evaporation, rf sputtering[45]
CeO_2/IBAD-YSZ/hastelloy alloy (no-texture)	PLD [46]

Epitaxial growth of CeO_2 films is comparably easy on single crystal YSZ substrates. Araki et al [47] successfully obtained a critical current density J_c of 4.1 MA/cm_2 (77K, 0T) for YBCO film on CeO_2 buffered single crystal YSZ substrate. In this case YBCO film was deposited by metalorganic deposition (MOD) using trifluoroacetates.

Abrutis reported [48] CeO_2/YBCO hetreostructures on YSZ deposited by a new pulsed injection chemical vapor deposition (CVD) technique. The CeO_2 buffer layer stopped Zr diffusion from the substrate into the film, improved the YBCO film epitaxy and increased J_c up to $4\text{-}5\times10^6 A/cm^2$ at 77K.

Li et al [49] obtained a J_c of $5MA/cm^2$ for 0.4μm YBCO film deposited by a solution-based method and $2.5MA/cm^2$ for 1.2μm thickness YBCO film on CeO_2 buffered YSZ single crystals.

For microwave passive devices and Josephson junction applications, YBCO films are preferably deposited on sapphire , single crystal Si and GaAs substrates, according to the requirements on the microwave properties, as well as strength, size, and cost. But these substrates all react with YBCO film at the deposition temperature and degrade the superconducting properties, so it is necessary to insert a buffer layer between them.

CeO_2 buffered sapphire is a low-loss buffer layer/substrate combination suitable for the deposition of YBCO films [50]. R-cut sapphire($(1\bar{1}02)$ Al_2O_3), which possesses high crystalline quality, mechanical strength, and low dielectric permittivity ($\varepsilon\approx10$) and

losses ($\tan\delta \approx 10^{-7}$~$10^{-8}$ at 77K, 10GHz), is very suitable as a substrate for YBCO film for microwave applications. But there is a serious interdiffusion of Al into YBCO film which leads to the formation of an uncontrolled $BaAl_2O_4$ interfacial layer that heavily degrades the superconducting properties of the YBCO. Buffer layers, such as CeO_2, MgO, and YSZ, are deposited on $(1\bar{1}02)$ Al_2O_3 in order to solve this problem. CeO_2 has been proven to be one of the most successful buffer layers on $(1\bar{1}02)$ Al_2O_3. (001) CeO_2 buffer layers reduce the lattice mismatch between $(1\bar{1}02)$ Al_2O_3 and (001) YBCO, and a CeO_2 buffer layer having a thickness of only 20nm on R-plane sapphire is sufficient to prevent Al diffusion and thus allow the deposition of high-quality HTS films [51].

Yang et al [52] studied the effects of the post-annealing temperature of CeO_2 buffer layer on the microwave and structural properties of YBCO film deposited on a CeO_2 buffer layer on R-cut sapphire. The TE011 mode Q of a rutile-loaded cavity resonator with YBCO films on CeO_2/Al_2O_3, post annealed at 1000-1050°C, showed the unload Q as high as 1.8×10^5 at 77K at 8.6GHz.

The deposition of YBCO films on Si substrates is of special interest for the integration of superconducting and semiconducting devices. But the high deposition temperature prevents high quality growth of the YBCO film due to the interdiffusion. Many efforts have been successfully made to use buffer layers on Si to prevent the interaction of Si and YBCO. The lattice constant of CeO_2 is 5.411Å, close to the 5.431Å of Si. Moreover, CeO_2 can be an effective interdiffusion barrier because of low chemical

reactivity with Si and YBCO. CeO_2 films have been successfully used as a buffer layer on (100) Si substrates on which c-oriented or a-oriented YBCO films can be fabricated [53].

Another important field where CeO_2 is used as a buffer layer is YBCO coated conductor. It is impossible at present to directly deposit YBCO superconducting film on metal substrates, so buffer layers are necessary. Many types of single buffer layers and multi-buffer layers have been made for coated conductors. The details of buffer layers for coated conductors will be discussed in Sections 2.8 and 2.9.

For microwave applications, an important parameter is the surface resistance (R_s) of YBCO films. which is strongly related to the surface roughness of the YBCO film. There are two causes for worsening the roughness of YBCO films: one is particle formation during deposition, another is the roughness of the substrates and buffer layers. So it is important to control the roughness of CeO_2 films used as buffer layers in microwave applications of YBCO films on Al_2O_3, YSZ and Si substrates.

Develos et al have done intensive research on CeO_2 films deposited on single crystal Al_2O_3 substrates. They studied the surface morphology and orientation of CeO_2 films grown by pulsed laser deposition on R-cut ($1\bar{1}02$) Al_2O_3 substrates and evaluated the effects of the pre-deposition annealing conditions of the Al_2O_3 and the film thickness of CeO_2, The annealing of Al_2O_3 substrates improves the smoothness of the surface, and performing this in high vacuum leads to better crystallinity and orientation of deposited CeO_2 films compared to those annealed in oxygen [54]. A critical value of the film

thickness was found beyond that the surface roughness increases abruptly. Atomic force microscopy (AFM) study showed that the surface of CeO_2 films is characterised by a mazelike pattern [55]. Increasing the film thickness leads to the formation of larger islands which cause an increase in the surface roughness of the films. The areal density and height of these islands increased with film thickness.

In another paper, Develos et al [56] have investigated the effect of the deposition rate, as a direct function of the pulse laser repetition rate, on the surface morphology of CeO_2 films deposited by the pulsed laser deposition (PLD) technique on R-plane Al_2O_3 $(1\bar{1}02)$ substrates. Two regimes of growth were found within the investigated range of deposition rate. It was found out that in the high deposition rate-regime (within 2-4 nm/min), the critical thickness is approximately 90 nm, but in the low deposition rate-regime (less than 1 nm/min), the critical thickness is shifted to approximately 40 nm. Films belonging to these two regimes of crystalline growth were found to have characteristically different formations and surface morphologies. As observed through atomic force microscopy (AFM), the surface morphology is composed of longitudinal islands forming a maze-like pattern in the high deposition rate-regime, while the characteristic morphology was composed of rounded islands in the low deposition rate-regime. Significant reductions in the areal density of large islands and characteristically smoother films were achieved using a low deposition rate.

Develos et al [57] have also examined the effect of varying the CeO_2 buffer layer thickness on the microwave surface resistance R_s and surface morphology of YBCO films deposited by pulsed laser deposition. R_s measured via the sapphire dielectric

resonator technique was significantly lower for YBCO film grown on CeO_2 with thickness less than the critical thickness (d_c). The increase in the R_s value when the buffer layer thickness is greater than d_c is considered to be due to the increased surface outgrowths and presence of a-axis domains in the YBCO film. Changes in the microstructure and orientation of the YBCO films were found to be strongly influenced by the underlying CeO_2 layer.

Surface outgrowths in pulsed-laser-deposited YBCO/CeO_2/Al_2O_3 thin films have been studied by Develos et al [58]. They found that the surface outgrowths are mostly composed of CuO and $YCuO_2$ phases that have segregated at the top of $BaCeO_3$, a product of the interfacial reaction of YBCO with CeO_2. Cross-sectional transmission electron microscopy observations further revealed a $BaAl_2O_4$ phase formed beneath the $BaCeO_3$ phase, down to the CeO_2-Al_2O_3 interface. Despite the presence of these outgrowths, high critical current density J_c values > 2.0×10^6A/cm^2 were obtained.

Wang et al [59] have fabricated smooth, epitaxial CeO_2 thin films in the 450-650°C temperature range on (001) YSZ substrates *in-situ* by metal-organic chemical vapour deposition (MOCVD) using a new fluorine-free liquid Ce precursor. From AFM analysis of CeO_2 films, it was found that the surface consisted of a granular structure. Upon increasing the deposition temperature, the grain diameter remains approximately the same, but the root-mean-square roughness (Rms) of film decreases. At low growth temperature (450°C), the grain size was about 50-110 nm, while the Rms roughness was about 15.5Å. Close observation of the grain particles indicated that the grains are composed of tetragonal-pyramidal shaped hillocks, which were thought to consist of

four (111) planes. At higher temperatures (above 540°C), the surface becomes much smoother (Rms ~ 4.3Å), and hillock features are not detectable.

2. 7. Methods of fabrication of superconducting films and buffer layers

Since the beginning of fabrication of THS thin films, almost every fabrication method has been used to form the films. After several years study, it became evident that some methods were achieving good results, while other methods had disadvantages and were eliminated through selection. Like the superconducting films, buffer layers are made by many fabrication methods. So in this section, we give the description of the fabrication methods for superconducting films and buffer layers together. Some special methods used to fabricate the buffer layers on metallic substrates for coated conductors are described in Sections 2.9 and 2.10.

The fabrication methods used for superconducting films and buffer layers can be roughly separated into three categories: physical vapour deposition (PVD); chemical vapour deposition (CVD); and solution methods. PVD techniques include electron-beam evaporation, thermal evaporation, magnetron sputtering, ion-beam sputtering, molecular beam epitaxy (MBE) and pulsed laser deposition (PLD). Chemical vapour deposition mainly includes hydride CVD, trichloride CVD, and metal-organic CVD (MOCVD). The solution methods mainly include Sol-gel and MOD. The very general features, advantages and disadvantages of the commonly used deposition techniques are described below. Typical preoperational regimes of different techniques for $YBa_2Cu_3O_\delta$ film depositions are indicated in the pressure-temperature (P-T) phase diagram in **Fig.2.3** [60].

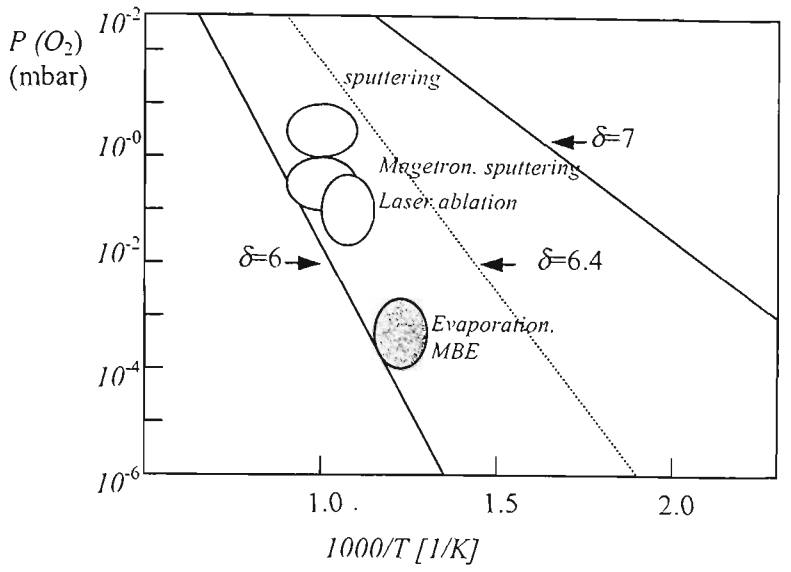

Figure 2.3. The pressure-temperature (P-T) phase diagram of $YBa_2Cu_3O_{7-\delta}$ [60].

2. 7. 1. Vacuum deposition

Magnetron sputtering techniques

Sputtering techniques are perhaps the earliest method used to deposit superconducting films and buffer layers. The equipment is simple, and the cost is low. The process is easy to control. Another advantage is that the deposition process can take place under high oxygen pressure, which is very suitable for depositing YBCO films. The sputtering techniques include DC magnetron sputtering and rf magnetron sputtering. **Fig.2.4** is a schematic diagram of magnetron sputtering deposition. DC magnetron sputtering is used to deposit HTS film, and rf magnetron sputtering is mainly used to deposit insulated buffer layers. For YBCO film deposition, there is resputtering (due to oxygen ions generated in the plasma) is a problem due to the consequent degradation of the superconducting properties and deposition rate. One method to avoid this problem is to set substrates at a angle to the target, which is called off-axis sputtering. With this in

mind, an inverted hollow target or facing target has been used by X. X. Xi et al [61] to obtain large area (typical 1-2 inch diameter)YBCO thin films. **Fig.2.5** is the schematic diagram of inverted hollow target DC magnetron sputtering deposition. The surface of YBCO thin films deposited by this method is smooth, and the surface resistance R_s is small. The main drawback of this method is that the deposition rate is much lower than for e-beam evaporation and PLD, about 2 - 20 nm/min, which limits the sputtering techniques that can be used to deposit thick films, such as YBCO films for coated conductor.

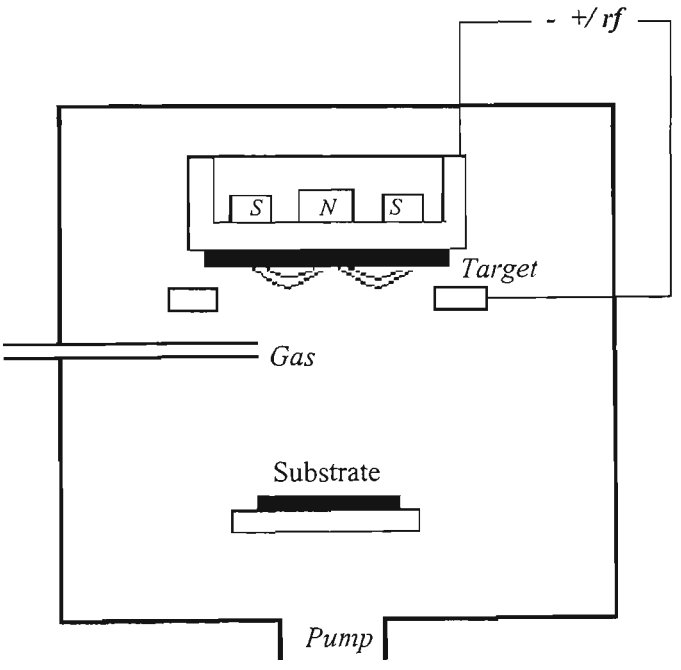

Figure 2.4. Schematic diagram of magnetron sputtering deposition.

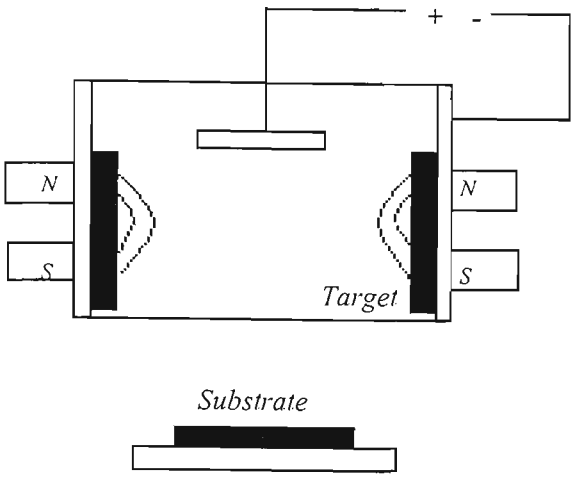

Figure 2.5. Schematic diagram of an inverted hollow target DC magnetron sputtering deposition.

Pulsed laser deposition

The history of PLD can be traced back to the early 1960s, just a few years after the first commercial ruby laser became available, but the development of this method was slow until 1986. During the early 1980s, PLD was used for the first time to deposit high-quality, epitaxial semiconductor films comparable to films grown by MBE [61]. As an example, the first observation of the Quantum Hall effect in a II-VI compound was made on a HgTe/CdTe superlattice grown by PLD. With the advance of industrial lasers with excellent long-term stability, the growth of very thick (tens of microns) semiconductor layers was possible. In this period, depositing oxides and other ceramic films also flourished by PLD. However, the lack of reliable UV lasers, which are the most suitable for the depositing of thin oxide films, limited the materials selection and film quality.

The successful growth of high-temperature superconductor film by PLD accelerated the development of this field. The technique has experienced an explosive growth since 1988. The number of research groups also increased from a handful of teams to several hundred laboratories spread worldwide. The ability to preserve the stoichiometry of a multi-component system, to oxygenate films *in situ* by reactive deposition, and to easily evaporate almost any materials finally brought long overdue recognition and renewed interest in exploring this technique to grow other materials. The latest trends include deposition of ferroelectric ceramic films and even the synthesis of doped and undoped Buckminster fullerenes (i.e. C_{60}) [62].

Conceptually and experimentally, PLD is an extremely simple film growth technique. **Fig.2.6** shows a schematic diagram of this technique. It uses pulsed laser radiation to vaporise materials and to deposit thin films in a vacuum chamber.

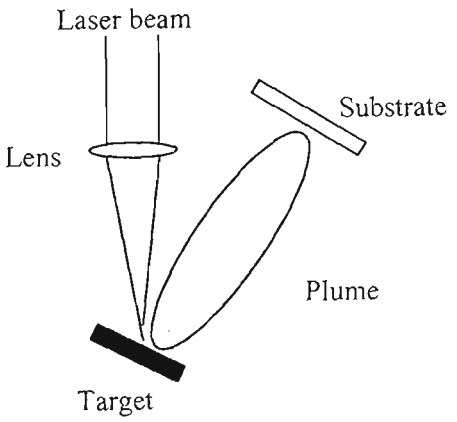

Figure 2.6. Schematic diagram of PLD.

Only a few parameters need to be controlled during the process. The targets used in PLD are small compared with the large size required for other sputtering techniques. It is quite easy to produce a multi-layer film of different materials. Besides, by controlling the number of pulses, fine control of film thickness can be achieved. The most important feature of PLD is that the stoichiometry of the target can be retained in the deposited films. This is the result of the extremely high heating rate of the target surface (108 K/s) due to pulsed laser irradiation. It leads to the congruent evaporation of the target irrespective of the evaporating point of the constituent elements or compounds of the target.

In spite of the said advantages of PLD, some shortcomings have been identified in using this deposition technique. One of the major problems is splashing or particulates deposition on the film. The size of particulates may be as large as a few microns. Such particulates will greatly affect the growth of the subsequent layers as well as the electrical properties of the film and should be eliminated. Another problem is the narrow angular distribution of the ablated species, which is generated by the adiabatic expansion of the laser produced plasma plume and the pitting of the target surface. Recently remedial measures, such as inserting a shadow mask to block off the particulates and rotating both target and substrate in order to produce a larger uniform film, have been developed to minimize some of the PLD problems.

Both YBCO superconducting films and almost every kind of buffer layer have been successfully deposited by the PLD method. For depositing large area films, laser beam

scanning and rotation of substrates are usually used in PLD systems. HTS films can be deposited on substrates up to 3 inch diameter [63].

High-quality YBCO thin films are routinely *in-situ* deposited by PLD from a stoichiometric target onto a lattice-matched substrate held at 700-800°C and positioned ~5-10cm away. Deposition takes place under ~ 100-300 mTorr of oxygen. The deposition rate is ~ 0.5-10Å/s according to the laser parameters. Once deposition is complete, the chamber is filled with oxygen and the substrate is cooled to near-room temperature. The typical transport properties of YBCO films are T_c values of ~ 90K, J_c values of ~4×10^6A/cm^2, and extremely low losses at microwave frequencies (R_s ~ 50-100μΩ at 10GHz, 4.2K) as well as low magnetic flux noise.[64]

Electron beam evaporation technique

In contrast to typical sputtering and PLD techniques using single stoichiometric targets, in the electronic beam evaporation process each material is supplied individually from metallic sources. **Fig.2.7** shows a schematic diagram of electron beam evaporation deposition. This approach is more flexible since the supply rate of the elements of the material can be easily changed. Another advantage is that a large uniform film is easily obtained using this technique. The largest YBCO film (8 inch diameter) reported to date was deposited by this method. However, the difficulty with this method is that calibration and accurate control are complex and difficult, especially for HTS materials with several elements. Moreover, low oxygen partial pressures at the sources have to be achieved during the deposition which also requires high oxygen partial pressures near

the substrate. Usually, e-beam evaporation deposition is used to deposit YBCO superconductor film and rarely used to deposit buffer layers.

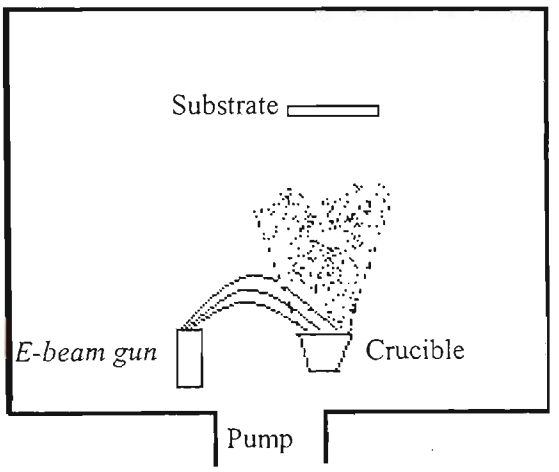

Figure 2.7. Schematic diagram of electron beam evaporation deposition.

Chemical vapour deposition (CVD) and metal-organic chemical vapour deposition (MOCVD)

In the chemical vapour deposition (CVD) process, the deposited phase is produced via chemical reactions. Thin films are deposited from gaseous precursors (typically metal halides), which flow together with a non-metal source gas such as H_2 or an oxidant to the CVD reactor on a heated substrate.

For most groups using MOCVD, three individual sources, typically b-diketone of Y $(thd)_3$, Ba $(thd)_3$, and Cu $(thd)_3$ are used for YBCO material. Sources are heated to suitable temperatures (between 100 - 300°C) to achieve appreciable vaporization.

Films grown by MOCVD have excellent superconducting properties, except for a rougher film surface and larger surface resistance than the best films grown by other techniques. Because of the advantages of MOCVD, such as the capacity for large-area growth and high growth rates, and familiarity in industry, this technique is promising for YBCO coated conductors.

2. 7. 2. Non-vacuum deposition

Solution methods

Solution deposition has been used to fabricate ferrite, high T_c superconductor, and dielectric and antireflection coatings. Solution deposition is a fast, cost-efficient method to ensure extensive ranges of film composition, and it is easy to achieve stoichiomeric control of complex mixed oxides, better than with CVD and MOCVD. The most frequently used solution-preparation approaches can be grouped into three categories [65]:

(1). Sol-gel processes that use 2-methoxyethanol as a reactant and solvent;

(2). Metalorganic decomposition (MOD) approaches that use large, water-insensitive carboxylate compounds;

(3). Hybrid processes that use chelating agents such as acetic acid, or diethanolamine to reduce alkoxide reactivity.

The precursor films are usually deposited by spin-coating, dip-coating, or print coating methods, so that it is easy to make a uniform large area films. The precursor films are very porous because a large fraction of the precursor volume is eliminated during pyrolysis as volatile hydrocarbon gases or water vapour, or both. There are many cracks

left in the precursor films caused by tensile stresses after the films significantly decrease their volume. Post-treatment can improve the density and surface morphology, but it is hard to obtain films as good as with vacuum deposition. So solution deposition methods are not commonly used to deposit the superconducting films and buffer layers that are used in electronic applications. YBCO film on $SrTiO_3$ with a T_c of 90K and J_c of $10^6 A/cm^2$ at 77K, 0T has been obtained by MOD [66].

After several cycles of solution depositions, the thickness of a film can be substantially enlarged, and the deposition rate is high. So, recently more and more researchers are using solution methods for the deposition of YBCO film and buffer layers on the coated conductors. Some remarkable progress in the solution deposition of YBCO films has been made in this field, which includes advances such as the trifluoroacetate metalorganic deposition (TFA-MOD) process and the coating pyrolysis process.

Using CeO_2 buffered YSZ single crystal substrates, YBCO films with J_c values of up to $5MA/cm^2$ for 0.4 μm and 2.5 MA/cm^2 for 1.2 μm films can be obtained by a solution process [67].

YBCO films were deposited on CeO_2/IBAD-YSZ/hastelloy by TFA-MOD. The J_c- B relationship of theseYBCO films shows J_c values of 1.4 MA/cm^2 at 77K, 0T and more than 10^5 A/cm^2 at 77K, 2T [68].

2-inch-diameter double-sided YBCO films deposited on $LaAlO_3$ and $LaAlO_3/Sr_2AlTaO_6$ substrates by the coating-pyrolysis process had an average J_c value great than $10^6 A/cm^2$ at 77K, 0T [56].

Liquid phase epitaxy (LPE)

The LPE technique is an approach that can be used for rapidly fabricating YBCO film with a high speed (about several μm/min). YBCO film is formed in a condition near thermal equilibrium, and the density of crystal defects , such as pinning centres, is low. ISTEC carried out this method to fabricate YBCO film with a thickness of about 10μm on single crystal (100) MgO substrate [69]. A J_c of $1\text{-}2\times10^6 A/cm^2$ was obtained [70]. Although a thick film can be made by LPE, macroscopic defects such as cracks occur. Attempts to form YBCO films by LPE on Ni substrates with an NiO buffer layer have been reported [71]. The LPE method is only used for the fabrication of YBCO film. No buffer layers have been fabricated by this method.

2.8. Advantage of YBCO coated conductors

Besides electronic device applications, for electric power applications such as generators, motors, and superconducting magnets, superconductors must have a high critical current density (J_c) and, equally importantly, they must be available in long lengths and have good flexibility, which mean the HTS materials have to be fabricated into suitable conductors. Single crystal substrates, however, are not suitable for the conductors because of their cost, limitations in size and shape, and lack of flexibility. The first generation of HTS conductors is represented by Bi-2223 tapes. Several manufactures can now fabricate kilometre lengths of Bi-2223 conductor with critical

currents greater than 50A and with an engineering current density, J_e, about 10000A/cm^2 at 77K and zero magnetic field [72]. The primary method used in Bi-2223 tape production is Powder–in–tube (PIT) processing. In PIT processing, the precursor powder is sealed in a silver tube, then mechanically worked and heat treated to form a thin tape of silver (or silver alloy)–sheathed superconductor.

Because BSCCO exhibits poor flux pinning characteristics (i.e., less resistance to the motion of magnetic flux), applications of this superconductor have been limited to those areas where operations are conducted at low temperature (~35 K) and in a magnetic field of 1 T, or at high temperature (~65K) in a field of ~0.1 T [73]. The cost of Bi-2223 tapes is high because of the amount of Ag used in PIT processing. YBCO superconductor with a higher irreversibility field compared to BSCCO behaves better than BSCCO in the presence of a magnetic field. A great deal of research is going on all over the world to find a way to use YBCO material for conductor development. The biggest challenge for the fabrication of YBCO conductor is to overcome the weak-links at large angle grain boundaries. Fabrication of well-aligned YBCO by the PIT technique is very difficult. Although the PIT process produces good uniaxial texture, it has no way to produce biaxial texture, which is necessary to eliminate current barriers due to weak links, especially for YBCO superconductor. **Fig.2.8** illustrates uniaxial and biaxial textures. An alternative approach for depositing YBCO on a textured surface has been developed; this is usually referred to as the "coated-conductor" method. YBCO coated conductors are also called the second generation of HTS conductors. The fundamental aspect of this approach is to prepare a biaxial substrate or buffer layer as template, and

then epitaxially deposit YBCO films that have a biaxial texture consistent with the template.

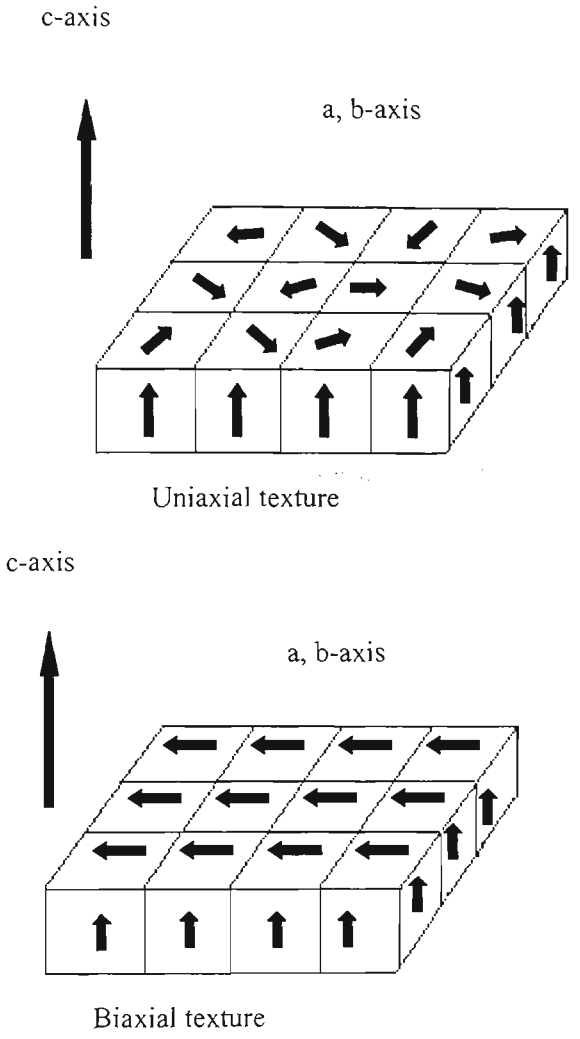

Figure 2.8. Unitexture and biaxial textures. The arrows refer to a axis of the lattice unit cell.

Instead of using ceramic substrates, metallic substrates are used for YBCO coated conductors in order to obtain flexible tapes. The problem of the fabrication of YBCO films on metallic substrates are almost same as with single crystal substrates; it is necessary for obtaining good superconductivity that YBCO film has a biaxial texture. Close control of substrate/buffer layer texture is required to give a good template for the

production of useful coated conductors. Other considerations for coated conductors are the thickness of the YBCO films, deposition rate, and cost. Some deposition methods for YBCO film on single crystal substrates are being gradually abandoned because of the low deposition rate, such as the sputtering method. Meanwhile some high deposition rate processes, such as chemical vapour deposition and solution methods, are being developed for coated conductors. Currently, there are two competing methods, the ionised beam-assisted deposition (IBAD) process, and the rolling-assisted biaxially textured substrate (RABiTS) process. The processing methods are quite different in detail, but the overall final structures are rather similar. **Table 2.10** lists the major achievements in YBCO coated conductors.

Table 2.10. The major achievements in YBCO coated conductors

Method	Group	J_c (A cm^{-2})	Length (cm)	Y-123 deposition	Year	Reference
IBAD	Fujikura/ super-GM	1.1×10^6	1	PLD	1995	[74]
		2.5×10^5	500	PLD	2001	[75]
	LANL	1.3×10^6	1	PLD	1994	[76]
		8.0×10^5	100	PLD	1998	[77]
ISD	Sumitomo/ TEPCO	2×10^5	1	PLD	2001	[78]
RABiTS	ORNL	$>1\times10^6$	1	PLD	1998	[79]
		1×10^5	100	Evaporation	2001	[80]
Rolling-textured Ag	Toshiba	6.1×10^4	100	PLD	1998	[81]
SOE	ISTEC/ Furukawa	3.0×10^5	1	PLD	1999	[82]

2.9. YBCO coated conductors using artificially textured template films

YBCO coated conductors can be fabricated using artificially textured template films as buffer layers on polycrystalline metallic tapes. **Fig. 2.9** schematically illustrates the structure of coated conductor using an artificially textured buffer layer. YBCO coated conductors using artificially textured buffer layers have the advantage of many choices of metal tapes, which means that the mechanical strength and other parameters are more desirable. For example, Hastelloy C276 tapes have a similar bending-strain durability and showed no J_c reductions under tensile strains of over 0.4%. They are quite easy to handle and could be expected to withstand large Lorenz forces for high magnetic field applications. Ionised beam-assisted deposition (IBAD) and inclining substrate deposition (ISD) are mainly the two primary methods for fabrication of artificially textured template films.

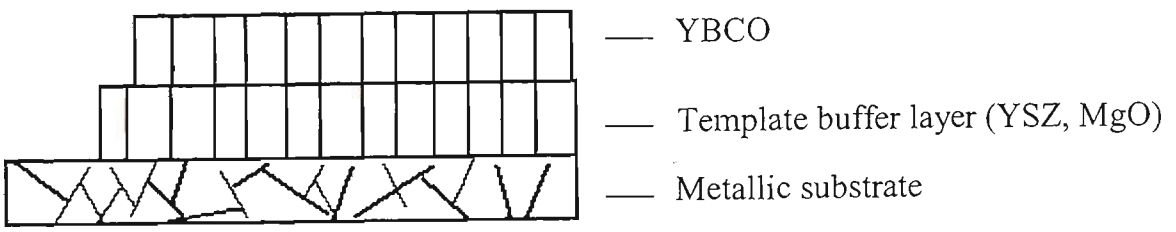

Figure 2.9. Determining the orientation of structure of coated conductor by using an artificially textured template buffer layer on a untextured substrate.

2.9.1. Ionised beam-assisted deposition method (IBAD)

In the development of YBCO conductors, the appearance of the IBAD method represented a milestone. Before that, YBCO films were mainly deposited on non-

biaxially textured metallical substrates such as Ag, and stainless steel. Uniaxially aligned Y-123 films (c-axis ⊥ substrates) are easily grown on polycrystalline substrates, but the superconducting properties are heavily degraded at grain boundaries where the a-axes and b-axes are randomly misaligned. The J_c value is less than $10^5 A/cm^2$ (77K, 0T).

The IBAD method is vacuum deposition using a secondary ion source. The process of IBAD is that while the film is being deposited another Ar^+ ion beam from the ion source is impacting on the films from a particular incident angle. The polycrystalline substrate is at room temperature in the process, and the energy and fluency of Ar^+ ions are 200-300eV and 100μA respectively. The peculiar crystalline alignment depends on both the deposition process and the ion beam bombardment. **Fig.2.10** schematically illustrates the IBAD method.

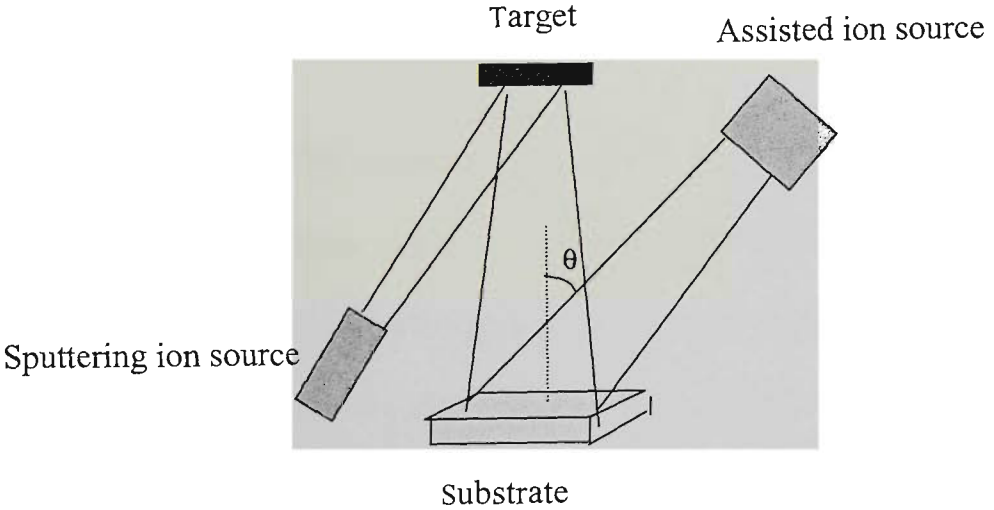

Figure 2.10. Principle of the IBAD method.

In 1991, Iijima et al [83] firstly achieved a sharp biaxial alignments of YSZ thin films on a polycrystalline Ni-alloy deposited by the IBAD method. It showed that IBAD is a successful method, which can obtain the biaxially aligned films without any epitaxial relationships.

A group at Los Alamos National Laboratory (LANL) [84, 85] optimized the deposition conditions and obtained excellent results. The YBCO and YSZ layers were deposited by pulsed laser deposition and ionized beam-assisted deposition, respectively. It was found that the transport critical current density (J_c) was more than 1MA/cm^2 at 75K, 0T, which is the first time that the J_c of HTS films on metallic substrates passed 1MA/cm^2, and about 1×10^7 A/cm^2 at 4K, 0T in a 1μm thick YBCO film. A zero field critical current of 120A at 75K was obtained in a 1μm thick and 1 cm wide YBCO film. Bending tests at 75K showed that the YBCO thick films on the metallic substrates could sustain a strain of 0.4% and over 1% for tension and compression, respectively.

Biaxial YSZ films were successfully fabricated by LANL while the Ar^+ ion beam incident angle was 55° from the normal of the substrate, which corresponds to the [111] axis of the YSZ unit cell. The ion beam divergence also has a significant effect on the film texture. One of the explanations for the origin of the azimuthal alignment is the anisotropy of the radiation damage on YSZ surfaces. Authers showed that the surface binding energy of the (111) plane was stronger than that of other low-index planes and should have lower etching damage. During the ion bombardment, the other plane with a different channel from the [111] channel becomes etched. However, the theory also

leaves some phenomena that could not be explained. The fact is that the surface roughness is quite low, not more than a few nanometers.

The out-of-plane <100> alignment of YSZ film can be quickly established while the thickness is small, but the development of the in-plane alignment is time consuming and costly. The FWHM of a ϕ-scan cannot drop below 20° until 1μm thickness. A reduction of the time constants is obviously beneficial for the mass production of coated conductors. MgO buffer layers deposited by IBAD are quite different from the results obtained for YSZ films. Very thin films with a thickness of 30 nm could be strongly textured by IBAD [86].

For coated conductors, the main problem with the IBAD method is how to increase the deposition speed for the buffer layer. One solution is to investigate other promising cubic oxides to find one that nucleates and develops biaxial texture more rapidly than MgO.

Another method is to develop ion gun systems with reduced beam divergence for large-area assist beams. A large area square-shaped RF-discharge ion source (66 cm×6 cm) was used with the IBAD method [87]. Textured YSZ films with an in-plane texture of 9-15° measured by the ϕ - scan FWHM were obtained in a growth area of 60×8 cm^2 by optimising the beam collimation for the assisting Ar^+ ions. 5.5 m long YSZ textured template layers were formed at 0.1 m/h by IBAD on Ni-Cr alloy tapes with $\Delta\phi$ of 12-13° throughout the whole length. A $\Delta\phi$ of 10.8° was obtained in a short tape moved at

0.3 m/h. Y-123 films were deposited by PLD on YSZ templates at a tape shifting speed of 1.0 m/h. An I_c of 84.0Å and J_c of 0.76 MA/cm^2 were obtained at 77 K, 0 T at a length of 1.0 m, while a $\Delta\phi$ for the Y-123 film was 7°.

2.9.2. Inclined substrate deposition method (ISD)

Inclined substrate deposition (ISD), first reported by Hasegawa et al [88], was developed to introduce in-plane alignment for the buffer layer on a non-textured metal substrate. As shown in **Fig.2.11** the ISD method is quite simple. In the ISD approach, a flexible metallic substrate (usually Ni-alloy tape) is held at an angle to the direction of the plume of the species to be deposited, and texturing is obtained without the assistance of an ion gun. The ISD deposition rate is more than one order of magnitude faster than in IBAD. After depositing the appropriate buffer layers, YBCO layer is developed on the buffer layers. An YBCO films epitaxially deposited on an ISD buffer layer by normal PLD had J_c values over 10^5 A/cm^2 at 77 K. The continuous deposition of over 10 m YBCO thin film tapes was performed with a reel-to-reel substrate transfer system combined with 200 W high power laser equipment [89].

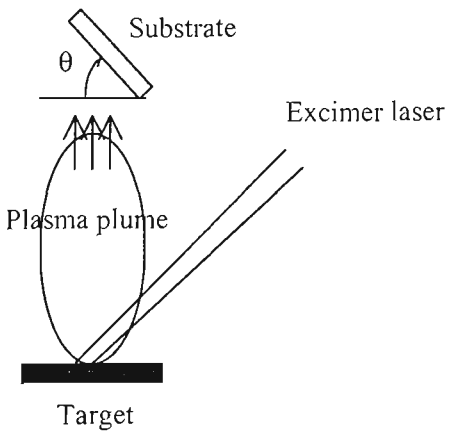

Figure 2.11. Priciple of the ISD deposition.

The mechanism of ISD is different from IBAD. In ISD, the <110> axis of YSZ is aligned towards the direction of the ablation plume, while in IBAD, the <111> axis is aligned towards the direction of the Ar^+ ion beam. Besides biaxial YSZ film, biaxial CeO_2 and MgO films can be obtained by ISD [90]. So far, the J_c of coated conductors made by ISD is lower than for those made by IBAD, but ISD has very high deposition rates and has potential advantages for scaling up to long tapes.

2.10. YBCO coated conductors using textured metallic substrates

2.10.1. Rolling and recrystallization texture

To produce long-length YBCO coated conductors with high J_c, orientation control of the metal substrate itself is a very effective approach. The rolling and heat-treatment process employed on some face-centred cubic (FCC) metallic materials can produce a cubic texture. **Table 2.11** gives the texture of some FCC metals after rolling and recrystallization. Silver and nickel are regarded as biaxially textured substrates for YBCO coated conductors because not only are their lattice constants close to those of YBCO film, but the biaxial texture can be obtained by a simple heat treatment after rolling. Producing a long-length YBCO tape by this method is simply and easy, while furthermore, the cost of manufacture is comparatively low.

Table 2.11. The texture of some FCC metals after rolling and recrystallization [91]

Material	Rolling temperature	Recrystallization texture
Al	cold	{100}<112>, {7 12 22}<845>
Cu	cold	{100}<001>, {122}<212>
Au, Ni	cold	{100}<001>
Ag	cold	{110}<112>, {311}<112>
	130°C	{100}<001>
	800°C	{110}<011>
Fe-Ni	cold	{100}<001>

2.10.2. Textured silver substrates

Silver is perhaps the first metal considered as a biaxially textured substrate because of the benign chemical interaction of silver with all HTS materials. Silver has been used in melt-processing of YBCO and to enhance mechanical properties and reduce processing temperatures [92], and also used as a support material for processing Bi-2223, Bi-2212 and Tl-1223 conductors. {110}<112> was the first preferred orientation for the recrystallization texture achieved by using cold rolling, and an YBCO film on this partial texture substrate had a J_c (4.2K, 0T) > 6×10^5A/cm^2 [37]. A 1 m long YBCO coated conductor produced on the (110) plane of Ag-Cu showed an average J_c of 6.1×10^4A/cm^2 (77K, 0T)[93]. Due to the fact that Ag is very soft, Yoshino et al [94] developed Ag-Cu/Ni/Ag-Cu clad tapes for YBCO coated conductor. 10 m long length tapes have been made by this method, and J_c for a 10cm length sample was 1×10^5A/cm^2 (77K, 0T).

The {100}<001> cubic texture of Ag was fabricated by Doi et al [95] using warm rolling and subsequent annealing at 700-850°C. The YBCO film showed c-axis orientation when the film was directly deposited on the Ag (100) plane, whereas in the a-b plane the crystal grains of 45° in-plane rotation were mixed with grains of 0° orientation which causes a superconducting weak coupling and a dramatically lowering of J_c. A CeO_2 buffer layer was prepared on Ag (100) by PLD. Yuasa et al [96] deposited YBCO film by means of MOCVD on a CeO_2/Ag (100) substrate. The FWHM of the ω-scan for CeO_2 (200) was 5.8°. The FWHM of the ϕ-scan for CeO_2 (220) was 12.3°. The FWHM of the ω-scan for YBCO (103) was 12.6°. The T_{c0} was 83K for YBCO film.

2.10.3. Rolling assisted biaxially textured substrates method (RABiTS)

Rolling assisted biaxially textured substrates (RABiTS), invented by Goyal et al (Oak Ridge National Laboratory in US (ORNL)) in 1994, is a method that allows a biaxially textured buffer layer to be obtained on the surface of nickel or nickel-alloy tapes with {100}<001> orientation. **Fig.2.12** schematically illustrates the RABiTS method. The cube (100) texture in Ni (99.99%) was produced by cold-rolling to over 90% deformation followed by recrystallization at temperatures ranging from 400 to 1000°C. The thickness of the textured Ni tapes was 125μm. Typical long-length Ni substrates have a texture corresponding to a ϕ-scan FWHM of ~6-8°, and more often are closer to 8° than 6°. By controlling the surface condition of the work rolls, it was possible to obtain substrates with surfaces as smooth as those obtained by mechanical and chemical polishing. The average of root mean square roughness (Rms) of the scan area of $50\times50\mu m^2$ is about 10nm [97].

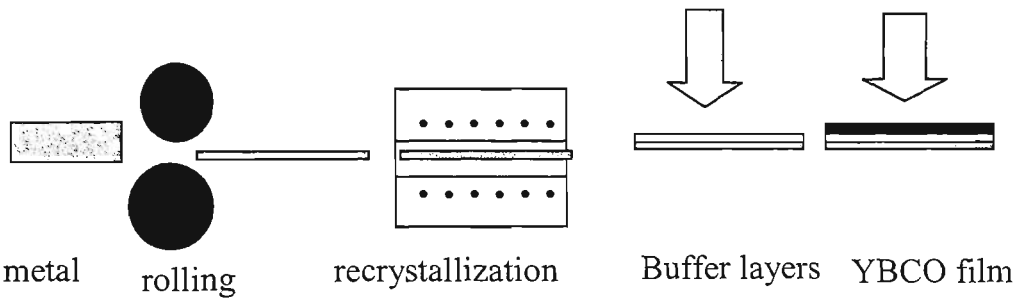

Figure 2.12. Schematic diagram of the RABiST methods.

In order to grow high quality epitaxial superconducting films on biaxially textured Ni substrates, it is necessary to deposit epitaxial buffer layers on the metal surface for improvement of the crystallinity of YBCO film and chemical reaction control between the metal substrate and YBCO film.

Typically, the desirable buffer layers for YBCO film growth are oxides. However, fabricating the oxide buffer layers on Ni for epitaxial deposition of YBCO superconducting films is difficult because of the ease of the surface oxide formation on Ni under the oxidizing atmospheres required for oxide film growth. Usually the orientation of NiO films is not epitaixal and (111) textured NiO is a preferential orientation, which is unsuitable for fabricating high-J_c YBCO films, since many high-angle grain boundaries are present. Two approaches have been found by ORNL to solve this problem [98].

In the first approach, noble metal layers such as Pd, Pt, Ag etc. are epitaxially deposited on metallic substrates, then the oxide buffer layers are epitaxially deposited on the noble metal surface which has a diminished tendency to oxidize.

In the second approach, an epitaxial CeO_2 buffer layer was directly deposited on the Ni by introducing H_2 gas during the initial film growth. Deposition was performed under a partial pressure of hydrogen such that NiO is unstable while CeO_2 is stable. In the experiment at ORNL, Ar + 4% H_2 was used to deposit CeO_2 films. Another effect of using Ar + 4% H_2 is that the epitaxial temperature is 400°C, much lower than that needed using oxygen, and this also reduced the oxidation of Ni.

CeO_2 films on Ni have cracks because of the thermal expansion mismatch between Ni substrate and CeO_2 film. After the CeO_2 film was deposited, a YSZ layer was deposited on CeO_2 film by PLD to alleviate cracking of the CeO_2 film. The CeO_2 and YSZ layers are each ~ 500nm thick. In order to improve the lattice match between buffer layers and the YBCO film a multilayer of CeO_2/YSZ/CeO_2 has been used on Ni. **Fig.2.13** gives the configurations of multi-buffer layers on cubic textured Ni substrate fabricated by ORNL.

So far, the quality of the cubic texture of nickel or nickel-alloy tapes is higher than that of silver. 2 km long length Ni tapes with cubic texture have been fabricated. The best meter long superconducting tape obtained by conversion from the reel-to-reel furnace showed a J_c of 1×10^5A/cm^2 end-to-end using a 1μV/cm criterion at 77K and self-field [80, 99].

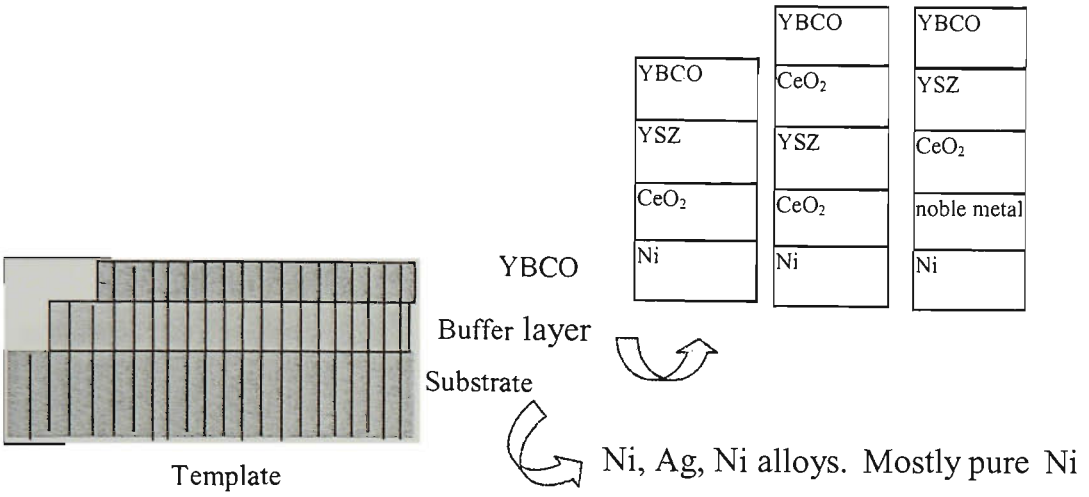

Figure 2.13. The configurations of multi-buffer layers on cubic textured Ni substrate fabricated by ORNL.

For reducing magnetism and increasing the strength of the substrate, Ni-Cr alloy substrates with Cr contents up to 13 at % were fabricated by rolling to deformations greater than 95% followed by annealing at high temperatures to form cubic textured alloy tapes [100]. Among these Ni-Cr alloy tapes, Ni -13at% Cr substrates are essentially non-magnetic to temperatures as low as 4.2K and have yield strengths a factor of 5 higher than pure Ni. A high critical current density (1.4MA/cm^2) has been obtained on the non-magnetic, Ni-13at%Cr alloy substrate.

Some in-depth research has been done on aspect of the RABiTS method, such as thermal grooves in Ni, cracks in CeO_2 film, and grain boundaries. It is important to determine the effects of specific surface features on metallic surfaces, such as slip lines,

grain boundary grooves, and other surface defects, on the buffer layer structure and on J_c of the deposited YBCO films.

Primary issues in the further development and improvement of RABiTS-based conductors include sharpness of the texture distribution along the strip, purity, uniformity of texture in the metal strip, epitaxy, crystallinity, adherence, and integrity of the buffer layers.

2.10.4. Surface-oxidation epitaxy (SOE)

While using the RABiTS method to fabricate YBCO coated conductor on cubic textured Ni substrates, a randomly oriented NiO film formed during deposition of the ceramic oxide buffer layers has a negative effect on the orientation of those buffer layers, and should be avoided as much as possible. However, {100}<001>NiO films can be positively utilised as a buffer layer for coated conductor on top of cubic textured Ni. The surface-oxidation epitaxy (SOE) method was invented by Matsumoto et al (Superconductivity Research Laboratory, ISTEC, Japan) [101, 102], which allows a biaxially textured NiO layer on a nickel tape surface can be made. This method is very simple compared with other methods, such as IBAD and RABiTS. It is useful for speeding up tape manufacturing because the SOE process installed in an electric furnace can easily and continuously form a biaxially textured NiO layer. The Simplification and effectiveness make this method most advantageous for scaling up to long tapes.

In SOE processing, a cubic textured nickel tape is put in an electric furnace heated to 1000-1300°C for metal oxidation. In the beginning of the oxidation process, an

epitaxial relation exists between the crystal orientations of the grown oxide and the underlying metal surface. This relation mainly depends on the crystal structure of the oxide and the underlying metal, and the oxidation conditions. **Fig.2.14** shows the SOE process.

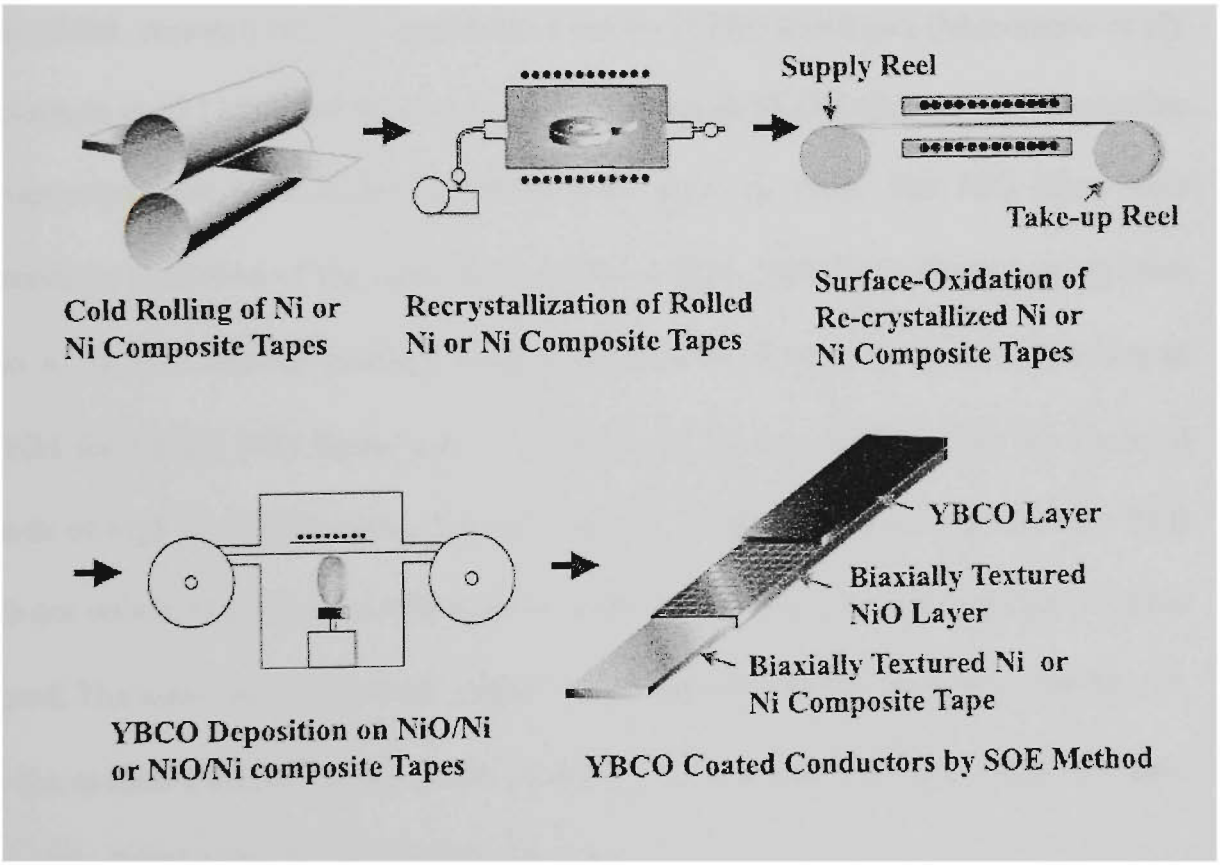

Figure 2.14. The SOE process [103].

The pure nickel tape used as the substrate has low mechanical strength, and the magnetism of nickel is another drawback for superconducting applications. Textured metal substrates that are non-magnetic or have substantially reduced magnetism and

greater strength are desirable. Recently, various approaches to the fabrication of stronger substrates with reduced magnetism have been studied, including the use of some alloys and composite structures.

The following are some representative works and good results obtained with the SOE method:

Most of the research on SOE was carried out by ISTEC/Furukawa (Matsumoto et al). Matsumoto et al [102] had fabricated in-plane aligned YBCO films on polycrystalline Ni tapes buffered with surface-oxidized NiO layers in 1998. The NiO films were prepared by oxidation of the cubic textured Ni at 1000-1300°C for times ranging from 5min to 2h in 1 atm of purified oxygen flowing in an electric furnace. The ϕ-scan FWHM for Ni and NiO layers are 6-8° and 12-14°, almost sufficient for the epitaxial growth of high J_c YBCO films. YBCO films on the NiO/Ni tapes deposited by PLD were not only c-axis oriented with respect to the tape surface, but also strongly in-plane aligned. The x-ray ϕ-scan FWHM of the (103) peak for YBCO film is typically 11-13°, and the ω-scan FWHM of the (005) peak is 2-3°. The YBCO films on NiO/Ni tapes have a T_c of 87K and a J_c of $5\text{-}6\times10^4$(77K, 0T).

In 1999, Matsumoto et al [104] improved the technique and deposited thin oxide cap layers such as YSZ, CeO_2, and MgO on the SOE-grown NIO/Ni to enhance the superconducting properties of the YBCO films. The oxidation of nickel was carried out at 1000-1200°C for 3h in flowing Ar gas at a flow rate of 500cc/min. T_c = 88K and J_c = 3×10^5 A/cm^2 (77K, 0T) and 1×10^4 A/cm^2 (77K, H//c, 4T) were obtained for YBCO film

on MgO/NiO/Ni. The results suggested that a thin MgO layer capped the grain boundaries of NiO, so that the formation of high-angle grain boundaries and nickel contamination in the YBCO film in the vicinity of the NiO grain boundaries was effectively suppressed.

In 2000, Watanabe and Matsumoto et al. [105] had prepared cubic textured Ni-clad Ni-20wt%Cr (Nr/NiCr) and Ni-clad austenitic stainless steel (Ni/SS) tapes as substrates for YBCO coated conductors by cold-rolling and subsequent heat treatment. These tapes have higher strength and lower magnetism than those of pure nickel tape. Highly {100}<001> textured NiO layers were formed on those textured composite tapes by using the SOE method, which was carried out for 30 to 3000 seconds at temperatures of 1000 to 1250°C in air. A thin MgO cap layer deposited on the NiO layer improved the surface qualities of NiO, so that YBCO films with a J_c of 1.0×10^5A/cm^2 (77K,0T) have heen obtained on MgO/Ni/NiCr tapes. A 50 m long biaxially textured NiO buffer layers have been fabricated by the SOE method for YBCO coated conductors. The SOE-NiO layers were highly {100}<001> textured, and ϕ-scan FWHM for the NiO layer was 10-14.5° throughout the whole length. J_c values of 0.3MA/cm^2 (77K,0T) have been obtained for a short sample of YBCO/MgO/NiO/Ni. YBCO films with a J_c of 0.1MA/cm^2 (77k,0T) have been obtained on MgO/NiO/Ni/NiCr short tapes.

Besides the Matsumoto et al (ISTEC/Furukawa) work, some other groups also have done some works in this field. Boffa et al. [106] have prepared YBCO/CeO_2/NiO multilayers on biaxially textured $Ni_{89}V_{11}$ non-magnetic alloy. The role of vanadium is to decrease the Curie temperature of Ni and to favour the formation of oriented NiO.

{100}<001>NiO buffer layer was formed by the controlled oxidation of the Ni-V substrate under 10mTorr oxygen pressure and at 700°C. J_c of 0.6MA/cm^2 (77K,0T) was obtained for 0.7μm thick YBCO films.

Lockman et al [107] studied NiO layers fabricated using SOE method on Ni-based textured substrates. In this work, the high temperature oxidation of NiO was studied under different oxygen partial pressures. Pure Ni, Ni-10%Cr and Cr-coated Ni have been investigated. Pure Ni oxidised at 1250°C for 3h in P_{O_2}~1 atm has shown excellent pure cubic texture. Ni-10%Cr oxidised under the same condition has shown the same texture, but the tape becomes very brittle.

In summary, up to this point the cubic texture of NiO films is not as good as in buffer layers obtained by the IBAD and RABiTS methods, which is the one of reasons why the value of J_c is lower than 1MA/cm^2. Another reason is that other problems with NiO films, such as grain boundaries, cracks and film roughness, degrade the superconducting properties of YBCO films.

2.10.5. YBCO films for coated conductors

The above description of coated conductor methods is mainly focused on the fabrication of the buffer layers for coated conductors whose quality is a critical feature. There is a long way to go before large scale applications of coated conductors become viable. **Fig.2.15** illustrates the likely course of further research on YBCO coated conductors.

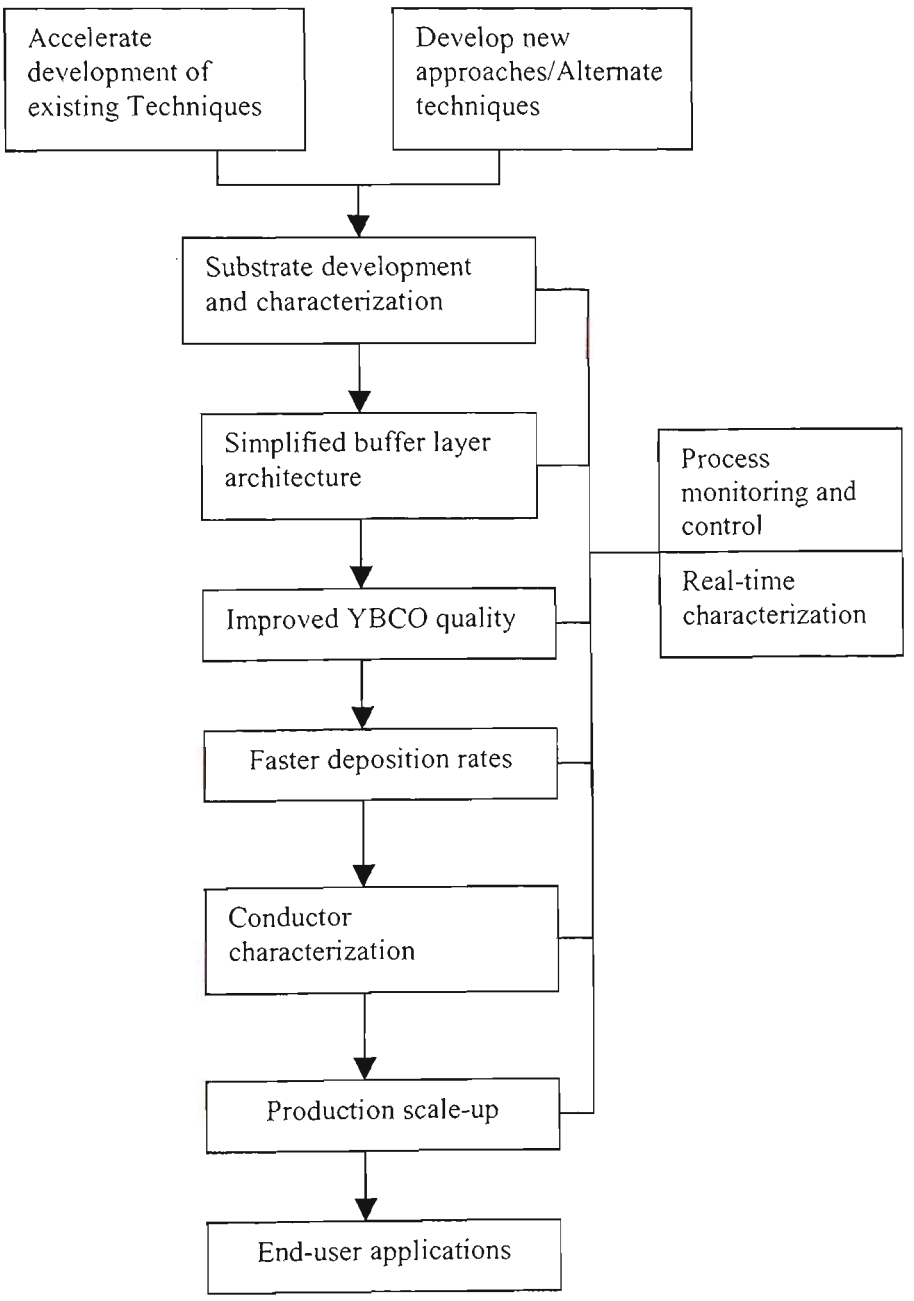

Figure 2.15. Research objectives for YBCO coated conductors.

There are some specific characteristics of YBCO films for coated conductors which are different from those for microelectronic applications. The two important issues of YBCO films for scaled-up production of coated conductors are:

1. Increasing YBCO film thickness while maintaining high current density;
2. Increasing YBCO film deposition rates or mass throughput while maintaining high current density.

The zero field critical current shows a strong initial decrease with increasing film thickness. One possible mechanism is surface pinning or Bean-London surface barriers that will constitute a smaller percentage of the total pinning as the thickness increases. A general investigation of surface and interface flux pinning would be of great merit for coated conductors.

A variety of deposition techniques have been employed to deposit 1-5μm thick YBCO films. The properties of these films depend critically upon the microstructures that develop during the nucleation and growth of the films. These microstructures depend on the substrate properties, the particular deposition technique, the processing conditions and the film thickness. There is as yet little fundamental understanding of the nucleation and growth processes and how specific microstructures develop.

For the first issue, the growth conditions for desirable microstructures should be determined for each deposition process and for the desired layer thicknesses, as well as what is needed for precise control of the optimum deposition conditions, such as film stoichiometry, during the total deposition process. Alternative non-vacuum processes for fast, reliable, and economical deposition of YBCO should be pursued. These include MOCVD, sol - gel and liquid phase epitaxy.

For the second issue, a flux of atomic oxygen can be used to grow YBCO at substantially higher rates. High fluxes of oxygen ($>10^{17}$ O/cm^2 s) can be generated, transported and used to grow films. This is a possible route to a faster, more economical deposition process.

Chapter 2 references

1. H.Kamerlingh Onnes, Leiden Communication 120b, 122b, 124c (1911).

2. W. Meissner and R. Ochenfeld, Naturwiss 21(1933) 787.

3. J. G. Bednortz and K. A. Muller, Z. Phys. B64 (1986) 189.

4. M. K. Wu, J. R. Ashburn, C. J. Torng, P. H. Hor, R. L. Meng, L. Gao, Z. J. Huang, Y. Q. Wang, and C. W. Chu, Phys. Rev. Lett. 58 (1987) 908.

5. Z. Z. Sheng and A. M. Hermann, Nature 322 (1988) 138.

6. H. Maeda, Y. Tanaka, M. Fukutomi, and T. Asano, Jpn. J. Appl. Phys., 27 (1988) 209.

7. Frank J. Owens and Charles P. Poole, Jr.The new superconductors, Plenum Press, New York and London,(1996) p98.

8. Markku Leskela, Heini Molsa and Lauri Niinisto, Supercond. Sci. Technol. 6 (1993) 627.

9. John Gallop, Supercond. Sci. Technol.10 (1997) A120.

10. R Wordenweber, Supercond. Sci. Technol. 12 (1999) R86.

11. Susan E. Babcock, MRS Bulletin, August 1992, 20.

12. M. Hein, High-Temperature Superconducotr thin films at Microwave Frequencies, published by Springer, 1996, p250.

13. Frank J. Owens and Charles P. Poole, Jr. The new superconductors, Plenum Press, New York and London,(1996) p104.

14. A. R. Jha, Applications to mMicrowave, Electro-optics, Electrical Machines, and Propulsion Systems, JOHN WILEY & SONS, INC. p6.

15. S. R. Foltyn, R. E. Muenchausen, R. C. Dye, X. D. Wu, L. Luo, and D. W. Cooke, Appl. Phys. Lett 59 (1991) 1374.

16. B. F. Cole, G. C. Liang, N. Newman, K. Char, and G. Zaharchuk, Appl. Phys. Lett. 61 (1992) 1727.

17. Y. J. Tian, S. Linzen, F. Schmidl, R. Cihar and P. Seidel, Superconduct. Sci. and Tech. 11 (1998) 59.

18. Holstein W L, Parisi L A, Shen Z-Y, Wilker C, Brenner M S, and Martens J S, J. Supercond, 6 (1993) 191.

19. Siegal M. P. ,Venturini E. L. , Overmyer D L and Newcomer P P, J. Supercond. 11 (1998) 135.

20. Kleiner R,Steinmeyer F, Kunkel G and MullerP, Phys. Rev. Lett. 68 (1992) 2394.

21. M. Moriya, T. Okamoto, K. Usami, T. Kobayashi and T. Goto, IEEE transactions on Applied superconductivity , 9 (1999) 2380. Sudershan Y. S., August Yurgens, Dag Winkler, IEEE transactions on Applied superconductivity , 11 (2001) 2703.

22. Markku Leskela, Heini Molsa and Lauri Niinsto, Supercond. Sci. Technol. 6 (1993) 627.

23. R. Gross, P. Chaudhri, M. Kawasaki, M. B. Ketchen, A. Gupta, Appl.Phys. Lett. 57 (1990) 727.

24. J. Geerk, G. Linker and O. Meyer, Materials Science Reports 4 (1989) 193.

25. D. M. Hwang, T. S. Ravi, R. Ramesh, S. W. Chen, C. Y. Chen, X. D. Wu, A. Inam, and T. Venkatesan, Appl. Phys. Lett. 57 (1990) 1690.

26. M. J. Cima, J. S. Schneider, and S. C. Peterson, Appl. Phys. Lett. 53 (1988) 710.

27. C. M. Carlson, J. C. Price, P. A. Parilla, D. S. Ginley, D. Niles, R. D. Blaugher, A. Goyal, M. Paranthaman, D. M. Kroeger and D. K. Christen, Physica C 304 (1998) 82.

28. P. K. Petror, E. F. Carlssom, P. Larsson, M. Friesel, and Z. G. Ivanov, J. Appl. Phys. 84 (1998) 3134.

29. Develos KD. Yamasaki H. Sawa A. Nakagawa Y. Physica C. 361 (2001) 121.

30. Ohshima S. Develos KD. Ehata K. Ali MI. Mukaida M. Physica C. 335 (2000) 207.

31. Develos KD. Kusunoki M. Mukaida M. Ohshima S. Superconductor Science & Technology. 12 (1999) 887.

32. Develos KD. Kusunoki M. Mukaida M. Ohshima S. Physica C. 320 (1999) 21.

33. Develos KD. Kusunoki N. Ohshima S.Japanese Journal of Applied Physics Part 1-Regular Papers Short Notes & Review Papers. 37 (1998) 6161.

34. Kim CG. Kim KP. Yang JH. Park CY. Japanese Journal of Applied Physics Part 1-Regular Papers Short Notes & Review Papers. 40 (2001) 4769.

35. Preisler EJ. Marsh OJ. Beach RA. McGill TC. Journal of Vacuum Science & Technology B. 19 (2001)1611.

36. Pan TM. Chien CH. Lei TF. Chao TS. Huang TY. Electrochemical & Solid-State Letters. 4 (2001) F15.

37. Yoo JH. Nam SW. Kang SK. Jeong YH. Ko DH. Ku JH. Lee HJ. Microelectronic Engineering. 56 (2001) 187.

38. Manabe T. Yamaguchi I. Tsuchiya T. Kondo W. Mizuta S. Kumagai T. Japanese Journal of Applied Physics Part 1-Regular Papers Short Notes & Review Papers. 40 (2001) 4866.

39. Q. Li, W. Zhang, U. Schoop, MW. Rupich, S. Annavarapu, DT. Verebelyi, CLH. Thieme, V. Prunier, X. Cui, MD. Teplitsky, LG. Fritzemeier, GN. Riley, M. Paranthaman, A. Goyal, DF. Lee, TG. Holesinger, Progress in solution-based YBCO coated conductor, Physica C. 357 (2001) 987.

40. MW. Rupich, Q. Li, S. Annavarapu, C. Thieme, W. Zhang, V. Prunier, M. Paranthaman, A. Goyal, DF. Lee, Specht ED. List FA.Low cost Y-Ba-Cu-O coated conductors IEEE Transactions on Applied Superconductivity. 11 (2001) 2927.

41. T. Araki, Y. Takahashi, K. Yamagiwa, T. Yuasa, Y. Iijima, K. Takeda, SB. Kim, Y. Yamada, I. Hirabayashi IEEE Transactions on Applied Superconductivity, 11 (2001) 2869.

42. M. Paranthaman, TG. Chirayil, S. Sathyamurthy, DB. Beach, A. Goyal, FA. List, DF. Lee, X. Cui, SW. Lu, B. Kang, ED. Specht, PM.Martin, DM. Kroeger, R. Feenstra, C. Cantoni, and DK.Christen, IEEE Transactions on Applied Superconductivity. 11(2001) 3146.

43. M. Parathaman, D. F. Lee, A. Goyal, E. D. Specht, P. M. Martin, X. Cui, J. E. Mathis, R. Feenstra, D. K. Christen, and D. M. Kroeger, Supercond. Sci. Technol. 12 (1999) 319.

44. Aytug T. Wu JZ. Kang BW. Verebelyi DT. Cantoni C. Specht ED. Goyal A. Paranthaman M. Christen DK. Physica C. 340 (2000) 33.

45. X. Cui, F. A. List, D. M. Kroeger, A. Goyal, D. F. Lee, J. Mathis, E. D. Specht, P. M. Martin, R. Feenstra, D. T. Verebelyi, D. K. Christen, M. Paranthaman, Physica C 316 (1999) 27.

46. Hiroshi Fuji, Tetsuji Honji, Yuichi Nakamura, Teruo Izumi, Araki Takeshi, Izumi Hirabayashi, Yuh Shiohara, Yasuhiro Iijima, and Kaoru Takeda, Physica C 357-360 (2001) 1011.

47. T. Araki, Y. Takahashi, K. Yamagiwa, T. Yuasa, Y. Iijima, K. Takeda, S. B. Kim, Y. Yamada, and I. Hirabayashi, IEEE Transactions on Applied Superconductivity 11 (2001) 2869.

48. A. Abrutis, Journal de Physique IV. 9 (1999) 683.

49. Q. Li, W. Zhang, U. Schoop, M. W. Rupich, S. Annavarapus, D. T. Verebelyi, C. Thieme, V. Prunier, X. Cui, M. D. Teplitsky, L. G. Fritzemeier, G. N. Riley, M. Paranthaman, A. Goyal, D. F. Lee, and T. G. Holesinger, Physica C 357 (2001) 987.

50. Holstein W L, Parisi L A, Face D W, Wu X D, Foltyn S R, and Muenchausen R E, Appl. Phys. Lett. 61 (1993) 982.

51. Denhoff M W and McCaffrey J P, J. Appl. Phys.70 (1991) 3986.

52. W.I. Yang, J. H. Lee, J. M. Jang, J. S. Ryu, J. Hur, and S. Y. Lee, IEEE Transactions on Applied Superconductivity, 11 (2001) 3419.

53. F. Sanchez, M. Varela, X. Queralt, M. V. Garcia-Cuenca, R. Aguiar and J. L. Morenza, Physica C 195 (1992).

54. Develos KD. Kusunoki N. Ohshima S. Japanese Journal of Applied Physics Part 1-Regular Papers Short Notes & Review Papers. 37 (1998) 6161.

55. S. Ohshima, K. D. Develos, K. Ehata, M. I. Ali, and M. Mukaida, Physica C 335 (2000) 207.

56. KD. Develos, M. Kusunoki, M. Mukaida, S. Ohshima, Physica C. 320(1999) 21

57. KD. Develos, M. Kusunoki, M. Mukaida, S.Ohshima, Superconductor Science & Technology. 12 (1999) 887.

58. K. D. Develos, H. Yamasaki, A. Sawa, Y. Nakagawa, Physica C 361 (2001) 121.

59. A. Wang, J. A. Belot, T. J. Marks, P. R. Markworth, R. P. H. Chang, M. P. Chudzik, and C. R. Kannewurf, Physica C 320 (1999) 154.

60. G. Oya, C. C. Diao, S. Imai, T. Uzawa, Y. Sawada, T. Sugai, and K. Nakajima, J. Appl. Phys. 77 (1995) 5809.

61. X. X. Xi, H. C. Li, J. Geerk, G. Linker, O. Meyer, B. Obst, F. Ratzel, R. Smithey, and F. Weschenfelder, Physica C 153-155 (1988) 794

62. R. F. Curland and R. E. Smalley, Scientific American Oct. (1991) 54.

63. M. Lorenz, H. Hochmuth, D. Natusch, H. Borner, G. Lippold, K. Kreher and W. Schmitz, Appl. Phys. Lett. 68 (1996) 3332.

64. Douglas B. Chrisey and Arun Inam, MRS BULLETIN, (1992) 37.

65. F. F. Lange, Science 273 (1996) 903.

66. Paul C. Mcintyre, Michael J. Cima, and Man Fai Ng, J. Appl. Phys. 68 (1990) 4183.

67. Q. Li, W. Zhang, U. Schoop, M. W. Rupich, S. Annavarapu, D. T. Verebelyi, C. L. H. Thieme, V. Prunier, X. Cui, M. D. Teplitsky, L. G. Fritzemeier, G. N. Riley Jr., M. Paranthaman, A. Goyal, D. F. Lee, and T. G. Holesinger, Physica C 357-360 (2001) 987.

68. T. Kumagai, T. Manabe, I. Yamaguchi, W. Kondo, F. Imai, K. Murayama, S. Mizuta, Physica C 357-360 (2001) 1346.

69. M. Yoshida, T. Nakamoto, T. Kitamura, O. B. Hyun, I. Hirabayashi, S. Tanaka, A. Tsuzuki, Y. Sugawara and Y. Ikuhara, Appl. Phys. Lett., 65 (1994) 1714.

70. S. Miura, K. Hashimoto, F Wang, Y. Enomoto and T. Morishita, Physica C 278 (1997) 201.

71. T.Maeda, S. B. Kim, T. Sugs, H. Kurosaki, T.Yuasa, Y. Yamada, T.Watanabe, K. Matsumoto, and I. Hirabayashi, Physica C 357-360 (2001) 1042.

72. L. Masur, 1999 Long length manufacturing of Bi-2223 wire for motor and cable applications ICMC Conference (Montreal, Canada, 12-16 July 1999).

73. A. Goyal, D. P. Norton, J. D. Budai, M. Paranthaman, E. D. Specht, D. M. Kroeger, D. K. Christen, Q. He, B. Saffian, F. A. List, D. F. Lee, P. M. Martin, C. E. Klabunde, E. Hartfield, and V. K. Sikka, Appl. Phys. Lett. 69 (1996) 1795.

74. Iijima Y, Hosaka K, Tanabe N, Sadakata N, Saitoh T, Kohno O and Toshitomi J, Critical Currents in Superconductivity ed T Matsushita and K Yamafuji (Singapore: World Scientific) p99.

75. Yasuhirio Iijima, Kazuomi Kakimoto, Kaoru Takeda, Physica C 357-360 (2001) 952.

76. Wu X D et al Appl. Phys. Lett. 67 (1995) 2397.

77. S R Foltyn, P N Arendt, C Dowden, R F DePaula, J R Groves, J Y Coulter, Q Jia, M P Maley and D E Peterson, 1999 IEEE Trans. Appl. Supercond. 9.

78. K. Ohmastu, K. Muranaka, S. Hahakura, T. Taneda, K. Fujino, H. Takei, Y. Sato, K. Matsuo, and Y. Takahashi, Physica C 357-360 (2001) 946.

79. J E Mathis, A Goyal, D F Lee, F A List, M Paranthaman, D K Christen, E.D Specht, D M Kroeger and P M Martin, Japan. J. Appl. Phys. 37 (1998) L1379.

80. S. W. Lu, F. A. List, D. F. Lee, X. Cui, M. Paranthaman, B. W. Kang, D. M. Kroeger, A. Goyal, P. M. Martin, and R. E. Ericson, Superconductor Science & Technology, 14 (2001) 218.

81. Yamazaki M, Thanh T D, Kubota H, Kudo Y, Yoshino H, and Nagamura H, Advances in Superconductivity Vol11, ed N Koshizuka and Tajima (Tokyo:Spring) (1999) 789.

82. K. Matsumoto, S. Kim, J. G. Wen, and I. Hirabayashi, IEEE Transaction on Applied Superconductivity, 9 (1999) 1536.

83. Iijima Y, Tanabe N, Kohno O and Ikeno Y, 1992 Appl. Phys. Lett. 60, 769

84. X. D. Wu et al, Appl. Phys. Lett. 67 (1995) 2397.

85. H. C. Freyhardt, J. Weismann, K. Heinemann, J. Hoffmann, J. Dzick. A. Usoskin, F. Garcia-Moreno and S. Sieves, IEEE Trans. Appl. Supercond. 7 (1997) 1426.

86. C P Wang, K B Do, M R Beasley, T H Geballe and R H Hammond, Appl. Phys. Lett. 71(1997) 2955.

87. Yasuhirio Iijima, Kazuomi Kakimoto, Kaoru Takeda, Physica C 357-360 (2001) 952.

88. K. Hasegawa, N. Yoshida, K. Fujino, H. Mukai, K. Hayashi, K. Sato, T. Ohkuma, S. Honjo, H. Ishii and T. Hara, Proc. Icec16/Icmc (Kitakyushu, Japan) ed T Haruyama, T Mitsui and K Yamafuji (Tokyo: Elsevier) (1997)141.

89. K. Ohmatsu, K. Muranaka, S. Hahakura, T. Taneda, K. Fujino, H. Takei, Y. Sato, K. Matsuo and Y. Takahashi,Physica C 357-360 (2001) 946.

90. M. Bauer, J. Schwachulla, J. Egly , P. Berberich and H. Kinder, Advances in Superconductivity 10 (1998) 979.

91. Y. Iijima and K. Matsumoto, Supercond. Sci. Technol. 13 (2000) 68.

92. A. Goyal, P. D. Funkenbusch, D. M. Kroeger and S. J. Burns, Physica C 182 (1991) 203.

93. M. Yamazaki, T. D. Thanh, H. Kubota, Y. Kudo, H. Yoshino, and H. Nagamura, Advances in Superconductivity Vol11, ed N Koshizuka and Tajima (Tokyo:Spring) (1999) 789.

94. H. Yoshino, M. Yamazaki, T. D. Thanh, Y. Kudo and H. Kubota, Physica C 357-360 (2001) 923.

95. T. Doi, N. Sugiyama, T. Yuasa, T. Ozawa, K. Higashiyama, S. Kikuchi, and K. Osamura, Advances in Superconductivity VII (1995).

96. T. Yuasa, H. Kurosaki, S. Kim, T. Maeda, K. Higashiyama and I. Hirabayashi, Physica C 357-360 (2001) 934.

97. A. Goyal, R. Feestra, F. A. List, M. Paranthaman, D. F. Lee, D. M. Kroeger, D. B. Beach, J. S. Morrell, T. G. Chirayil, D. T. Verebelyi, X. Cui, E. D. Specht, D. K. Christen, and P. M. Martin, JOM (1999) 19.

98. D. P. Norton, A. Goyal, J. D. Budai, D. K. Christen, D. M. Kroeger, E. D. Specht, Q. He, B. Saffian, M. Paranthaman, C. E. Klabunde, D. F. Lee, B. C. Sales, and F. A. List, Science, 274 (1996) 755.

99. A Goyal, D. F. Lee, F. A. List, E. D. Specht, R. Feenstra, M. Paranthaman, X. Cui, S. W. Lu, P. M. Martin, D. M. Kroeger, D. K. Christen, B. W. Kang, D. P. Norton,

C. Park, D. T. Verebelyi, J. R. Thompson, R. K. Williams, T. Aytug and C. Cantoni, Physica C 357-360 (2001) 903

100. M. Yamazaki, T. D. Thanh, H. Kubota, Y. Kudo, H. Yoshino, and H. Nagamura, Advances in Superconductivity Vol11, ed N Koshizuka and Tajima (Tokyo:Spring 1999) 789.

101. K. Maatsumoto, Y. Niiori, I. Hirabayashi, N. Koshizuka, T. Watanabe, Y. Tanaka and M. Ikeda, Advances in Superconductivity, Vol 10, ed K Osamura and I Hirabayashi (Tokyo:Springger) (1998) 611.

102. K. Maatsumoto, S. B. Kim, J. G. Wen, I. Hirabayashi, T. Watanabe, N. Uno and M. Ikeda, IEEE trans. Appl. Supercond. 9 (1999)1539.

103. T. Watanabe, K. Matsumoto, T. Maeda, T.Tanigawa, and I. Hirabayashi, Physica C 357-360 (2001) 914.

104. K. Matsumoto, SeokBeom Kim, I Hirabayashi, T. Watanabe, N. Uno and M. Ikeda, Physica C 330 (2000) 150.

105. T. Watanabe, K. Matsumoto, T. Maeda, T. Tanigawa and I. Hirabayashi, Physica C 357-360 (2001) 914.

106. V. Boffa, T. Petrisor, G. Celentano, F. Fabbri, C. Annino, S. Ceresara, L. Ciontea, V. Galluzzi, U. Gambardella, G. Grimald and A. Mancini, Supercond. Sci. Technol. 13 (2000)1467.

107. Z. Lockman, X. Qi, Andrey Berenov, Rainer Nast, Wilfried Goldacker and J. MacManus-Driscoll, Physica 351 (2001) 34.

Chapter 3. Experimental system and characterization techniques

3. 1. Pulsed laser deposition(PLD)

3.1.1. Film deposition process of pulsed layer deposition

Conceptually and experimentally, PLD is an extremely simple film growth technique, and only a few parameters need to be controlled during the process [1- 3]. The principle of pulsed laser deposition, in contrast to the simplicity of the system set-up, involves a very complex physical phenomenon [4]. These include not only the physical process of laser-material interaction due to the impact of high-power pulsed radiation on the solid target, but also the formation of a plasma plume with highly energetic species and even the transfer of the ablated material through the plasma plume onto the heated substrate surface. Thus the thin film formation process in PLD can generally be divided into the following four stages:

1. Laser radiation interaction with the target;
2. Dynamic of the ablation materials;
3. Deposition of the ablation materials with the substrate;
4. Nucleation and growth of a thin film on the substrate surface.

Each stage in PLD is critical to the formation of a high quality thin film that is crystalline, epitaxial, stoichiometric, and uniform and has small surface roughness.

In the first stage, the laser beam is focused onto the surface of the target. At sufficiently high flux densities and short pulse durations, all elements in the target are rapidly heated

up to their evaporation temperature. Materials are dissociated from the target surface and ablated out with the same stoichiometry as in the target. The instantaneous ablation rate is highly dependent on the fluence of the laser shining on the target. The ablation mechanisms involve many complex physical phenomena such as collisional, thermal, and electronic excitation, exfoliation and hydrodynamics.

During the second stage the emitted materials tend to move towards the substrate according to the laws of gas dynamics and show the forward peaking phenomenon. The spot size of the laser and the plasma temperature have significant effects on the deposited film uniformity. The target-to-substrate distance is another parameter that governs the angular spread of the ablated materials.

The third stage is important in determining the quality of the thin film. The ejected high-energy species impinge onto the substrate surface and may induce various type of damage to the substrate. These energetic species sputter some of the surface atoms and a collision region is formed between the incident flow and the sputtered atoms. As film begins to grow after a thermalised region is formed. The region serves as a source for the condensation of particles. When the condensation rate is higher than the rate of particles supplied by the sputtering, thermal equilibrium condition can be reached quickly, and a film grows on the substrate surface at the expense of the direct flow of the ablation particles and the thermal equilibrium obtained.

The nucleation-and-growth of crystalline films depend on many factors such as the density, energy, ionisation degree, and type of the condensing material, as well as the

temperature and the physico-chemical properties of the substrate. The two main thermodynamic parameters for the growth mechanism are the substrate temperature and the supersaturation.

In the PLD process, due to the short laser pulse duration and hence the small temporal spread of the ablated materials, the deposition rate can be enormous. Consequently a layer-by-layer nucleation is favoured and ultra-thin and smooth films can be produced. In addition the rapid deposition of the energetic ablation species helps to raise the substrate surface temperature. In this respect PLD tends to demand a lower substrate temperature for crystalline film growth.

3.1.2. Pulsed laser deposition system

Fig. 3.1 shows a schematic diagram of PLD system in this work.

The main features are the following:

1. Spherical chamber with best vacuum of 1×10^{-7} Torr
2. Turbo molecular pump
3. Compex 301 KrF excimer laser with a wavelength of 248nm, 25 ns pulse duration and a frequency of 1~10 Hz
4. Six target holders allowing multi-layer deposition
5. Targets rotation by an external motor
6. Substrate temperature up to 900°C, adjustable by a digital controller
7. Two gauges measure the pressure from 1 atm to 10^{-9} Torr

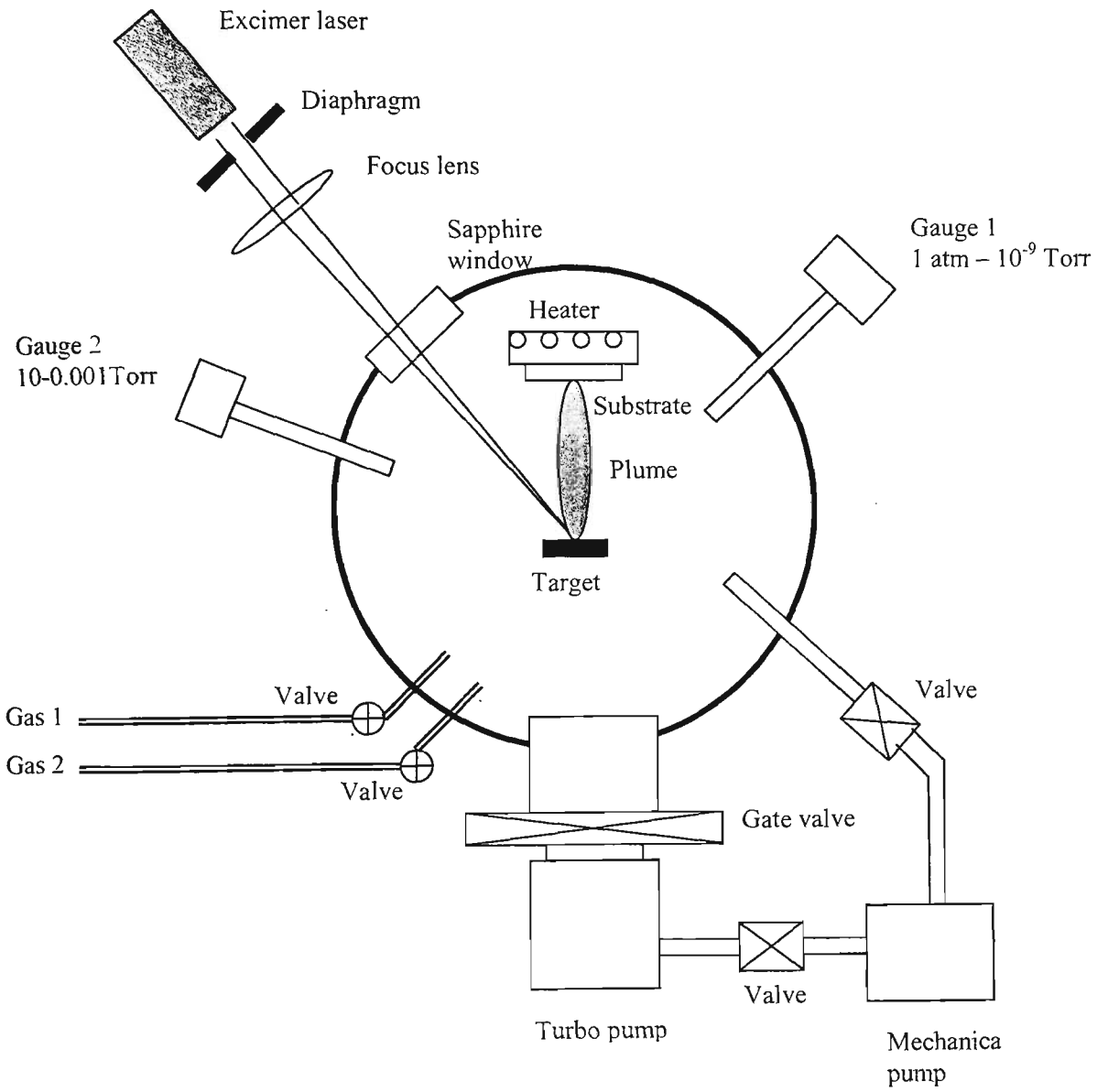

Figure 3.1. Schematic diagram of PLD system.

3.2. X-ray diffraction techniques

The texture analyses of CeO_2 and NiO films were carried out by X-ray diffraction techniques (XRD). The method employed was the constant diffraction vector method in

ωχφ geometry, which is schematically illustrated in **Fig. 3.2**. In this geometry, the X-ray source and the detector are fixed, and the crystallites of a sample are brought successively into the direction of the diffraction vector. XRD θ-2θ scan carried out on a Philips PW1010 were used to investigate the c-axis preference and phase analysis of CeO_2 and NiO films.

ω-scans, with the sample rotated around the CD axis at a small angle around a (hkl) direction, were used to investigate the alignment of the (hkl) orientation, expecially the c-axis (001) orientation. ω-scans were carried out using an MAC–Science X-ray system with 3 independent axes.

φ-scans, with the sample rotated about the sample normal, which may have a angle χ with the plane OST, were used to investigate the in-plane texture, especially the a-b plane texture. φ-scans were carried out using a Philips PW 1729 generator and a PW 1078 texture goniometer.

A pole figures were collected using the same that for φ-scan, and represent a series of φ-scans in which the angle χ is varied from 0 to 75°. Pole figures were used to analyze complicated textures, for example, the rolling texture of Ni tape. For cubic texture, the pole figure can give the out of plane and in-plane texture.

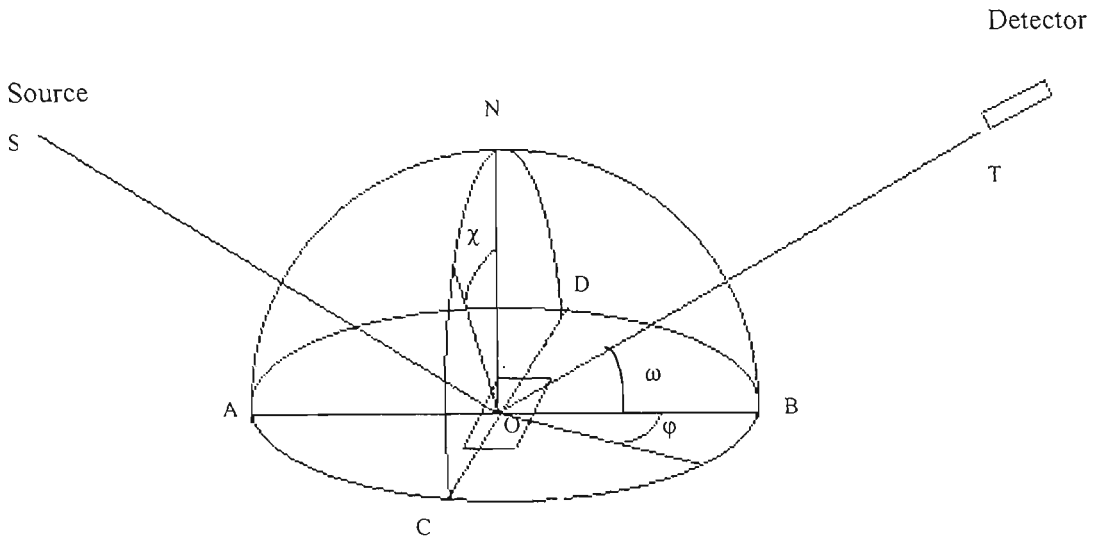

Figure 3.2. X-ray diffraction with ωχφ geometry.

3.3. Scanning electron microscopy (SEM)

Scanning electron microscopy (SEM) was used to investigate the surface morphology , microstructure, defects, and cracks in CeO_2 and NiO thin films. This technique was also used to observe the shape and size of crystalline grains, grain boundaries, and the interface between the thin films and substrates.

The instruments used in the electron microscopy work were a Jeol JXA-80 and a Leica Stereoscan 440, equipped with Electron Dispersive Spectroscopy (EDS) attachments. The microscopy was performed using secondary electron (SE) and back-scattered electron (BSE) imaging. Because the CeO_2 and NiO films are insulators, a very thin gold film was deposited on the surface of samples by DC sputtering in pure Ar. EDS was used to analyse the element composition of the detected spots.

3.4. Atomic force microscopy (AFM)

Atomic force microscopy (AFM) is the main scanning probe microscope technique used for studying the surface properties of materials from the atomic to the micron level [5,6,7]. The force most commonly associated with atomic force microscopy is an interatomic force called the van der Waals force. The dependence of the van der Waals force upon the distance between the tip and the sample is shown in **Fig. 3.3**. The AFM technique has three modes, eg. contact mode, non-contact mode and intermittent contact mode, according to the use of different force regimes.

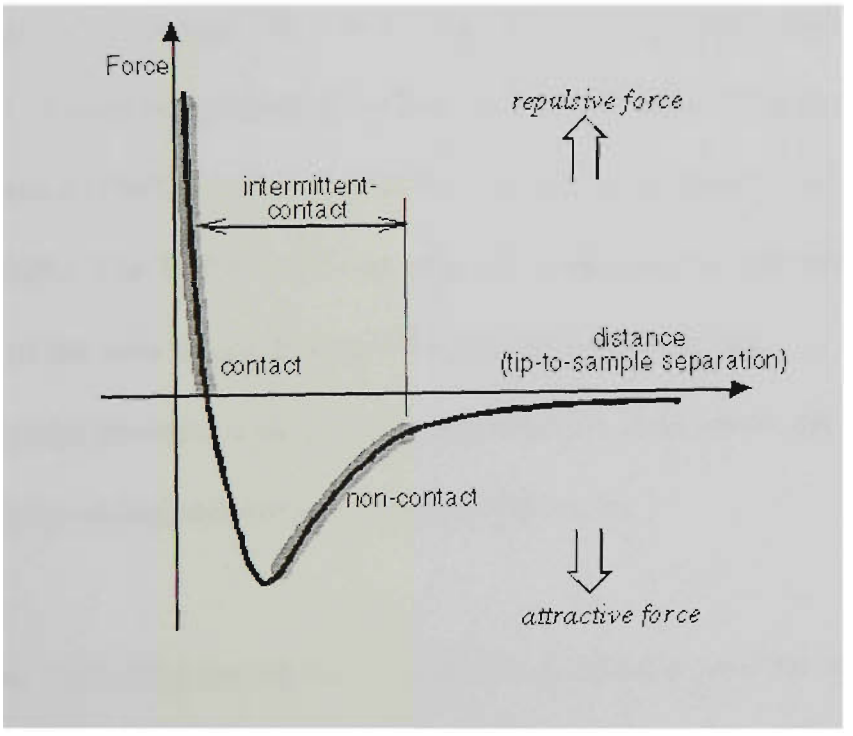

Figure 3.3. Interatomic force vs. distance curve.

An atomic force microscope (AFM) probes the surface of a sample with a sharp tip, about two microns long and often less than 100Å in diameter. The tip is located at the free end of a cantilever that is 100μm to 400μm long. Forces between the tip and the sample surface cause the cantilever to bend, or deflect. A detector measures the cantilever deflection as the tip is scanned over the samples, or the sample is scanned under the tip. The measured cantilever deflections allow a computer to generate a map of surface topography. AFM can be used to study insulators and semiconductors as well as electrical conductors.

Digital Extended Multimode AFM in contact mode was used to measure the surface morphology of CeO_2 and NiO films. **Fig. 3.5** is a schematic diagram of the AFM equipment. A laser beam bounces off the back of the cantilever onto a position-sensitive photo detector (PSPD). As the cantilever bends, the position of the laser beam on the detector shifts. The PSPD itself can measure displacements of light as small as 10Å. The ratio of the path length between the cantilever and the detector to the length of the cantilever itself produces a mechanical amplification. As a result, the system can detect sub-angstrom vertical movements of the cantilever tip.

The probes (including the tip and cantilever) commonly used for AFM measurements are cantilevers with integrated tips of Si_3N_4 or silicon. Si_3N_4 probes can be used for large flat surfaces as well as for atomic-scale imaging. In our experiments, triangular gold-plated Si_3N_4 tips, with lever lengths of 100nm and 200nm were used .

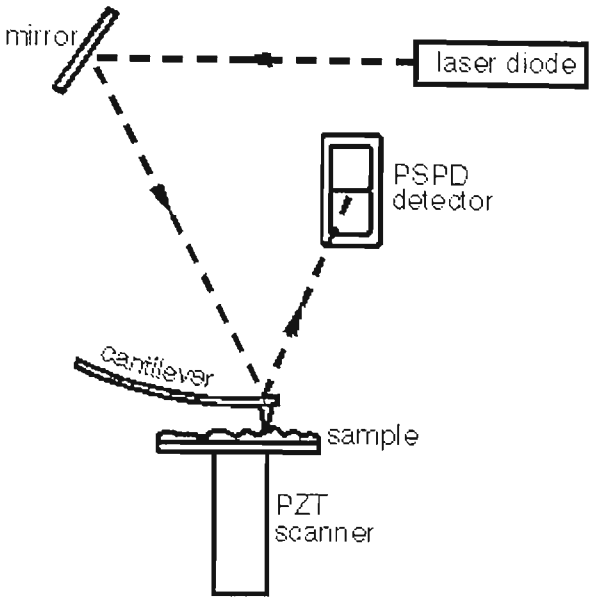

Figure 3.5. Schematic illustration of AFM system.

Chapter 3 references

1. C. L. Chan and J. Mazumder, J. Appl. Phys. 62 (1987) 4579.

2. G. K. Hubler, MRS Bulletin Feb. (1992) 26.

3. T. Venkatesan, X. D. Wu, R. Muenchausen , and A. Pique, MRS Bulletin Feb. (1992) 54.

4. J. Cheung and J. Horwitz, MRS Bulletin Feb. (1992) 30.

5. G.Binning, C. F. Quate and C. Gerber, Phys. Rev. Lett. 56 (1986) 9306.

6. J. L. Hutter and J. Bechhoefer, J. Appl. Phys., 73 (1993) 4123.

7. C.Bai, J. Li, Z.Lin, J. Tang and C. Wang, Surface and Interface Analysis 28 (1999) 44.

Chapter 4. Study of epitaxial CeO_2 films deposited by PLD on single crystal YSZ substrates

4. 1. Introduction

Develos et al [1-7] have done a series of studies of CeO_2 films deposited on single crystal Al_2O_3 substrates. The details of their research have been given in Chapter 2, and the main results are presented here again. They studied the surface morphology and orientation of CeO_2 films grown by pulsed laser deposition on R-plane $(1\bar{1}02)$ Al_2O_3 substrates, and a critical value of the film thickness was found beyond which the surface roughness increases abruptly. Two regimes of growth were found within the investigated range of deposition rates: in the high deposition rate-regime (within 2-4 nm/min), the critical thickness is approximately to 90 nm; but in the low deposition rate-regime (less than 1 nm/min), the critical thickness is shifted to approximately 40 nm. As observed through atomic force microscopy (AFM), the surface morphology was composed of longitudinal islands forming a maze-like pattern in the high deposition rate-regime, whereas the characteristic morphology was composed of rounded grains in the low deposition rate-regime. A significant reduction in the density of large islands and characteristically smoother films were achieved by using a low deposition rate. The effects of the pre-deposition annealing conditions of the Al_2O_3 were evaluated. The annealing of Al_2O_3 substrates improves the smoothness of the surface, and performing this in high vacuum leads to better crystallinity and orientation of deposited CeO_2 films compared to those annealed in oxygen .

Wang et al [8] deposited CeO_2 films by using metal-organic chemical vapour deposition (MOCVD) on YSZ substrates, and the surface morphology was analysed using AFM.

From AFM analysis of CeO_2 films, it was found that the surface consists of a granular morphology. Upon increasing the deposition temperature, the grain diameter remains approximately the same but the root-mean-square (Rms) roughness decreases.

In this chapter, the study of CeO_2 films focused on the four aspects: deposition conditions; orientation and crystallization (including out-of-plane orientation, in-plane orientation, and crystallization); surface morphology (including surface topography, outgrowth on surfaces, and roughness); and growth modes. All these four aspects are correlated with each other. **Fig. 4.1** illustrates the relationships between them. Deposition conditions are the basic factor that determines the other three, and the orientation and crystallization is most important and should be the first to be considered and achieved for CeO_2 film as buffer layers. Considerable work on CeO_2 film as buffer layers has been reported concerning the relationship between deposition conditions and orientations [9,10]. The morphology is another important property of CeO_2 films, as it influences the roughness and the surface resistance of YBCO films grown on top of them. Some work has been published on the growth mode of CeO_2 film, but no clear picture and theory of the growth of CeO_2 thin films have emerged. This chapter makes a contribution in the relationship of the above-mentioned aspects of CeO_2 films. The reason why YSZ substrate was chosen as a substrate material is that the relationship between the deposition temperature and the epitaxial quality of CeO_2 film can be studied due to a relatively wider epitaxial temperature range.

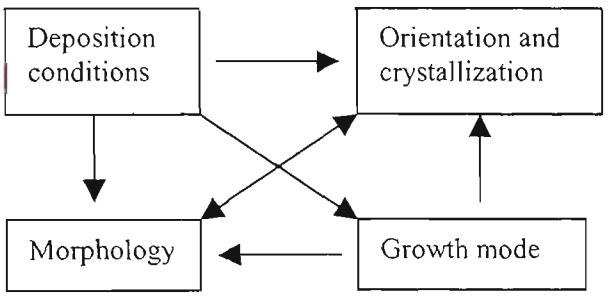

Figure 4.1. The relationship between the deposition conditions, orientation, morphology, and growth modes. Single arrows show a determining relationship, and a double-head arrow shows the correlation.

Typically, CeO_2 films used as a buffer layer on single crystal substrates such as Al_2O_3, YSZ or Si are deposited using an O_2 atmosphere [9-13]. However, for YBCO coated conductors, the commercially attractive rolling assistant biaxially textured substrate deposition technique (RABiTS) uses a CeO_2 buffer layer deposited on a cubic textured Nickel in an Ar + 4-10% H_2 atmosphere[14-18]. To the best of our knowledge, deposition in an Ar + H_2 atmosphere has not been thoroughly investigated. The role of H_2 was thought to be just that of a reducing gas suppressing the formation of NiO [14].

There are no references in the literature regarding the influence of H_2 on the morphology and orientation of CeO_2 film. This chapter also gives some research on the effects of H_2 on CeO_2 films.

4.2. Experiments

The CeO_2 target was prepared from CeO_2 (99.99%) powder which was pressed into a disk, and sintered in air at 1600°C for 6h. An XRD θ-2θ scan (Fig. 4. 2) shows that the target has pure CeO_2 cubic phase. CeO_2 films were deposited on single crystal (001) YSZ substrates by PLD, using an excimer laser system (Compex 301, 248nm from Lambda Physik). The particulars of the deposition system were: fixed laser beam at an angle of 45° to the normal of target; substrate parallel with target and on the axis of target; target-substrate distance 40~70mm; target rotation 10rpm; background pressure $1x10^{-6}$ Torr. The deposition conditions were: laser repetition rate 1~10Hz; pulsed laser duration 25ns; and energy density on the target 1.8~3.0 Jcm^{-2} (400~650mJ/pulse). The deposition pressures used were 200 mTorr of high purity O_2 (99.999%) and 100mTorr Ar + 10% H_2 forming gas. The uniform depositing area is at the plume center and about 10×12 mm^2. The 5×5, 5×10 and 10×10mm^2 YSZ substrates were mounted at this area of the sample heater using silver paste.

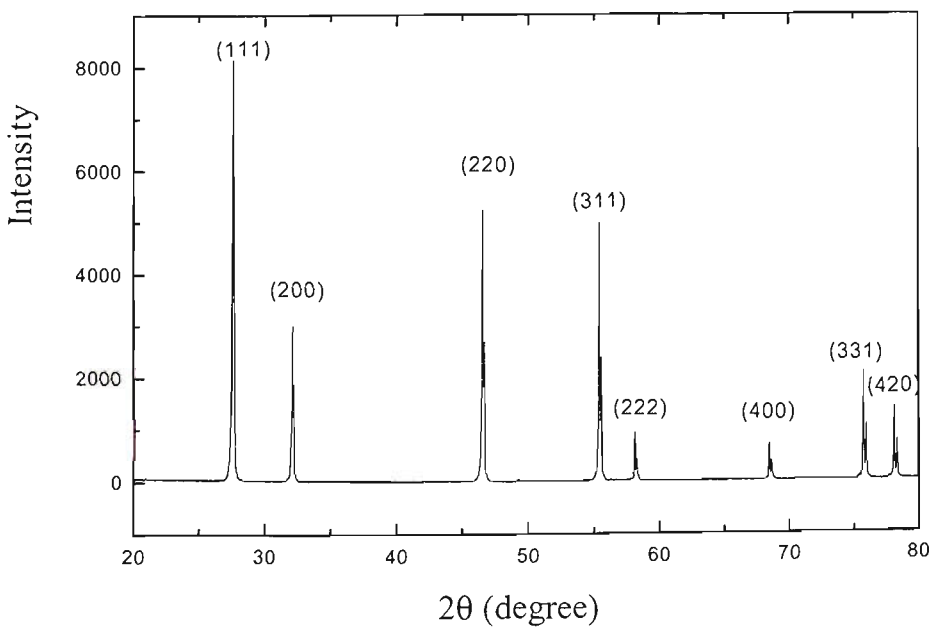

Figure 4.2. XRD θ-2θ scan of the CeO_2 target, which shows the pure cubic CeO_2 phase.

The thickness of the sample was measured using a profilometer. Sample preparation for measuring thickness was as follows. First, YBCO film was deposited on YSZ and patterned and etched in H_3PO_4, leaving alternate bands of YBCO and bare substrate. CeO_2 was deposited on top of this. The sample was then etched again in H_3PO_4, leaving this time alternate bands of CeO_2 and bare substrate. We varied the film thickness from ~3nm to ~1.3μm by adjusting the number of laser pulses. **Table 4.1** gives the parameters of the PLD deposition.

For all samples, after the deposition was completed, the heater was switched off, and the deposition pressure maintained until the temperature of the chamber was below 400°C. CeO_2 has a fluorite structure with a lattice constant of 5.41Å; YSZ has a cubic structure with a lattice constant of. 5.16Å. The lattice mismatch between (100) CeO_2 and (100) YSZ is about 5%. The orientation of the CeO_2 films was characterised by XRD θ-2θ scans and ω-scans. The surface morphology was examined by AFM technique (Digital Extended Multimode AFM) in contact mode, using triangular gold-plated SiN tips, with lever lengths of 100nm and 200nm. The scanner was a K scanner.

Measurements of surface roughness and the size of outgrowths were carried out with AFM, using the height scan mode. Since different values of roughness can be obtained from different scan areas, the root mean square roughness (Rms) value was always calculated for the same scan area. The three dimensional AFM images in this thesis were obtained using the height scan mode, and the two dimensional images of the morphology were obtained with the deflection scan mode and friction scan mode.

Table 4.1. Deposition parameters of the CeO_2 films

Growth parameters	Values
pulsed Laser duration	25ns
Laser energy	400 ~ 650mJ/pulse
Laser fluency	1.8 ~ 3.0Jcm^{-2}
Laser repetition rate	1 ~ 10Hz
Oxygen pressure	200mTorr
Ar + 10% H_2 pressure	100mTorr
Target-substrate distance	40 ~70mm
Substrate temperature	300 ~ 820°C
Target rotation	10rpm
Film thickness	3nm ~ 1.3μm

A. Characterization of YSZ substrates

The YSZ substrates used in this report were investigated before any deposition or other treatments. Commercial single crystal (100) YSZ substrates (ZrO_2 with 8~10 mol % Y_2O_3) have the (100) orientation within +/- 0.5 degree.The full width at the half maximum (FWHM) of the ω-scan was 0.15°, which means that the YSZ surface has a good c-axis orientation. The Rms values of YSZ for the 100×100mm^2, 40×40mm^2, and 5×5mm^2 substrates are 14.45, 7.97, and 1.87nm respectively. **Fig.4.3** shows an AFM image of YSZ, showing linear scratches due to polishing. The maximum depth of the scratches is about 7nm, and the average depth is 3nm.

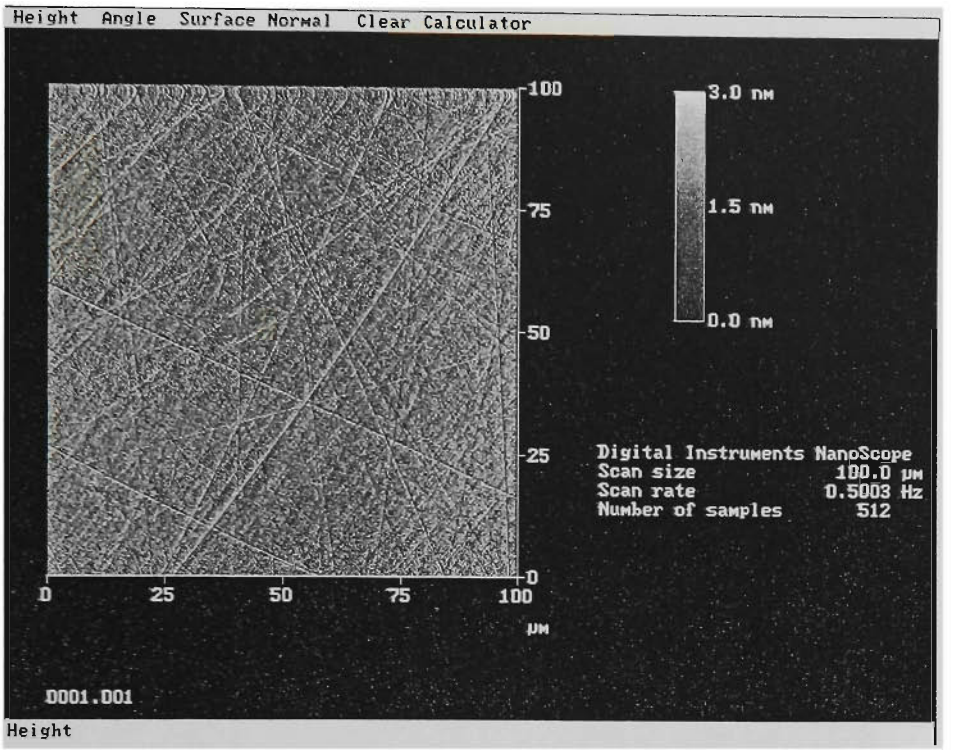

Figure 4.3. AFM image of an YSZ substrate.

B. Definition of the elements of the surface morphology of CeO_2 films.

The definitions associated with the morphology of CeO_2 films are given at this point. The surface morphology of CeO_2 films is consists of the following elements: a background morphology of grains (including the shape of grains) which is the morphology of the area between any outgrowths; outgrowths or islands (including singular outgrowth and linear outgrowth); linear grooves; and droplets caused by the laser ablation. In some cases when the density of outgrowths is high, it is difficult to distinguish the outgrowths from the background morphology. The size of droplets is about 5.5~1.0µm diameter, much larger than any kind of outgrowths. Droplets are not the subject of research in this report because they are not an intrinsic problem of thin film growth. **Fig. 4.4** gives a typical AFM image of a CeO_2 film that includes every element of the surface morphology except droplets.

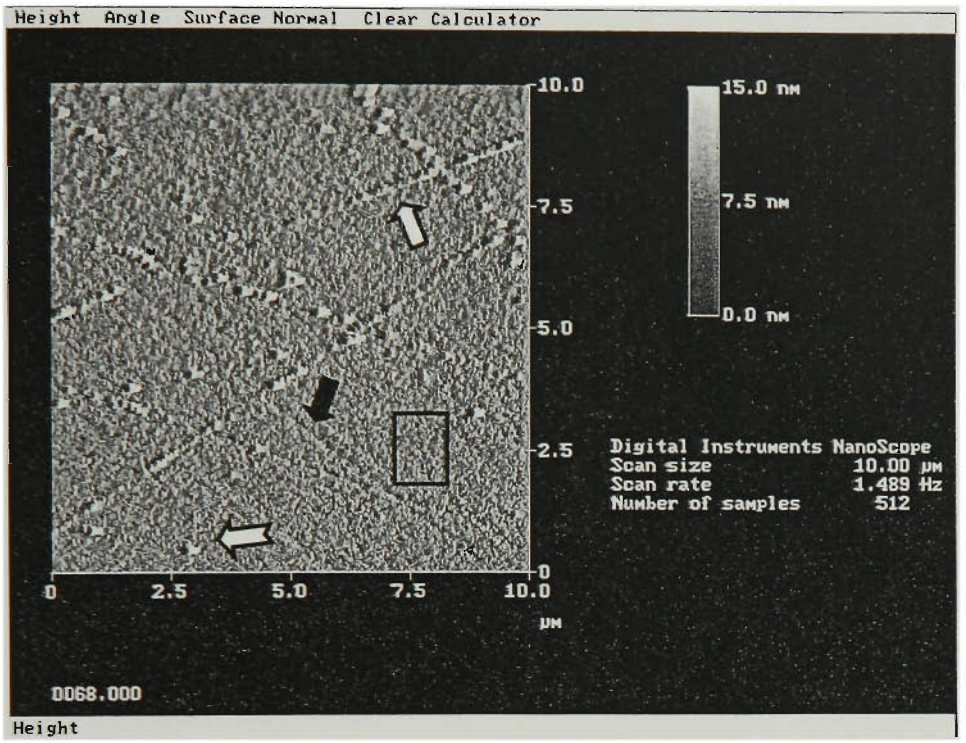

Figure 4.4. Typical AFM image of a CeO_2 film including the elements of the surface morphology.

4. 3. Relationship between deposition condition, orientation, surface morphology and growth mode of CeO_2 films

4.3.1. Epitaxial growth of CeO_2 films using different atmospheres

The results for an O_2 atmosphere are consistent with previous data reported in the literature. We were able to obtain pure c-axis oriented CeO_2 films with substrate temperatures in the range of 775 - 805°C . **Fig.4.5** shows an XRD θ-2θ scan of a CeO_2 film deposited in O_2 at 790°C.

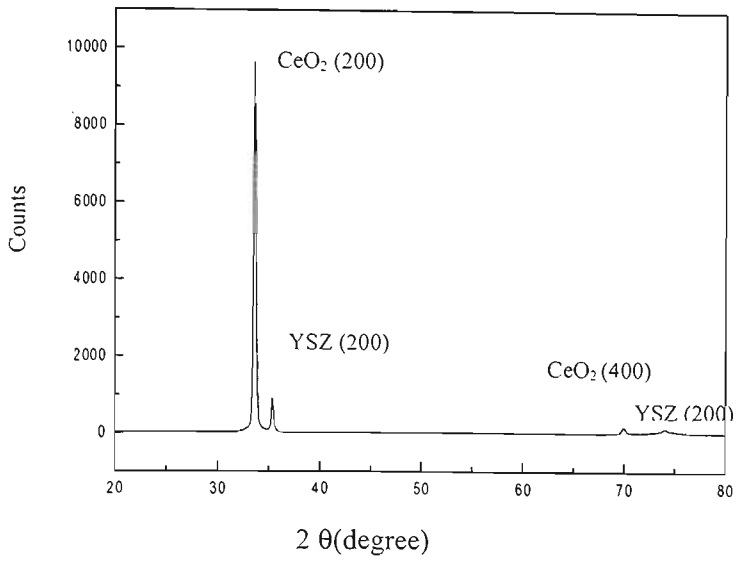

Figure 4.5. XRD θ-2θ scan for a CeO_2 film deposited in O_2 at 790°C.

For the films grown in an Ar + 10%H_2 atmosphere, pure c-axis oriented CeO_2 films were obtained over a much wider substrate temperature range of 350 - 775°C, as shown in **Fig. 4.6**. We also have investigated the orientation of CeO_2 films deposited using pure Ar, and found that the deposition temperature range for pure c-axis orientation is larger than for O_2 but less than for Ar + 10% H_2. Both the absence of O_2 and the presence of H_2 are responsible for the existence of this broad temperature range for the production of c-axis oriented films in an Ar + 10% H_2 atmosphere, compared to an O_2 atmosphere.

Investigation by XRD ω-scan shows that the c-axis orientation of the pure c-axis CeO_2 films deposited using O_2 is better than for those where Ar + 10% H_2 was used. The FWHM of the ω-scan of the (200) peak is less than 0.3° using O_2 (see **Fig.4.17**), but it is about 0.5 ~1.2° using Ar + 10% H_2. **Fig. 4.7** shows the XRD ω-scan of a CeO_2 film

deposited at 550°C using Ar + 10% H_2. The FWHM value is 0.57° **Fig.4.8** gives the ratio of diffraction intensities of the (200) and (400) peaks. From this figure, it can be seen that the ratio of I (200)/I(400) for the CeO_2 film deposited using O_2 is much larger than for using Ar+10% H_2. This feature is certainly related to the orientation of the films, but has not been given a satisfactory explanation so far.

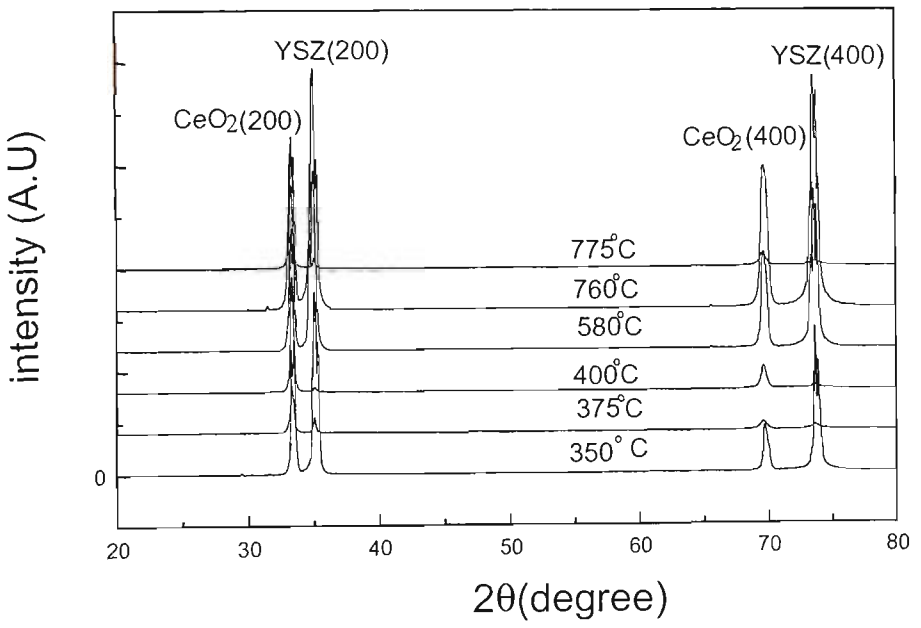

Figure 4.6. XRD θ-2θ scans of the CeO_2 films deposited in 100 mTorr of Ar+10%H_2 at different substrate temperatures on YSZ <100> substrates.

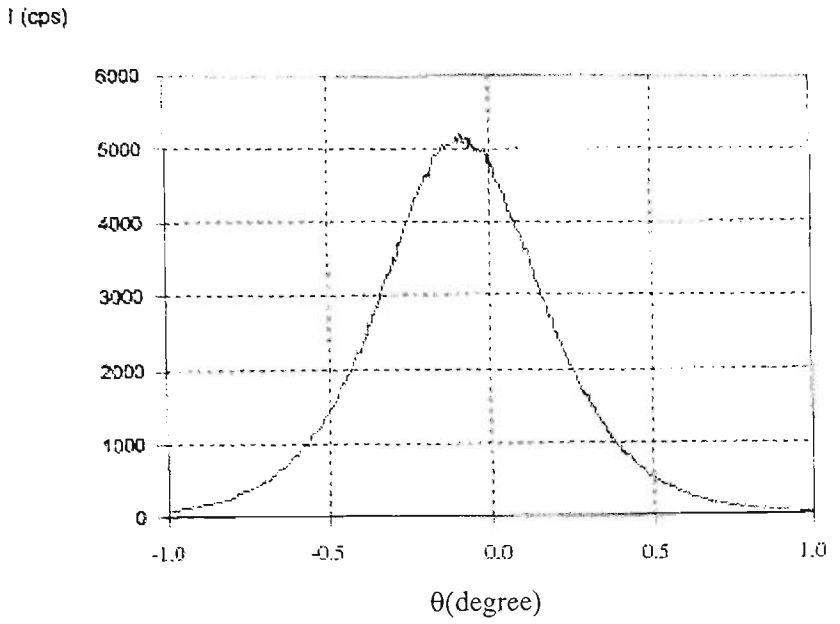

Figure 4.7. ω-scan of the (200) peak of a CeO_2 film deposited at 550°C using Ar + 10% H_2.

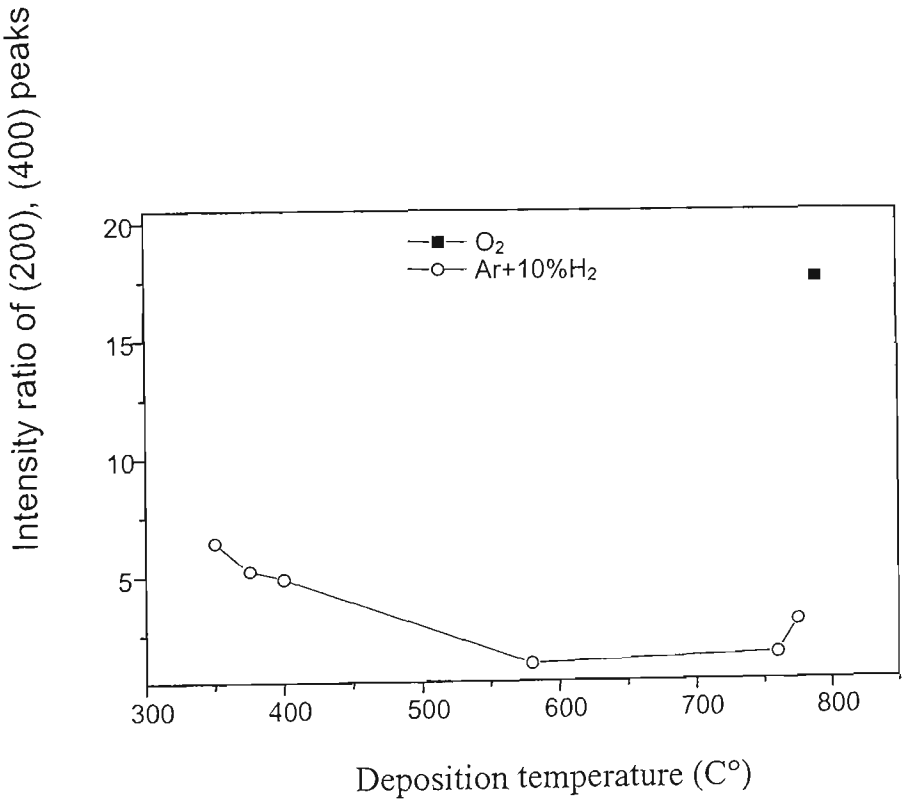

Figure 4.8. The variation of the intensity ratio I(200)/I(400) with temperature in X-ray θ-2θ scans using Ar+10%H_2 and O_2 atmospheres.

4. 3. 2. Surface roughness of CeO_2 films deposited using O_2 and Ar + 10% H_2

A. Surface roughness of CeO_2 films deposited using an O_2 atmosphere

Samples of different thickness in the range of 3nm – 1,300nm were produced and investigated. In order to allow for a direct comparison of the surface morphology, $10x10\mu m^2$ area free of particles caused by laser ablation was chosen on each sample. The root meant square (Rms) roughness was determined for each sample.

We first studied the relationship between the epitaxial temperature and the surface roughness of the CeO_2 films. This work is important for studying the epitaxial growth process in a CeO_2 film, but it can not be done by Develos et al on an Al_2O_3 substrate because a narrow range temperature is critical to the growth of a pure c-axis orientation CeO_2 film. Increasing or decreasing the temperature from the optimum value results to the growth of other orientations [10, 11]. **Fig.4.9** is a plot of the relationship between the temperature and the surface roughness. Although the CeO_2 films with a pure c-axis orientation were obtained over a temperature range of 775 - 805°C, the film deposited at 790°C has the smallest roughness. The following research thus focused on the films deposited at 790°C.

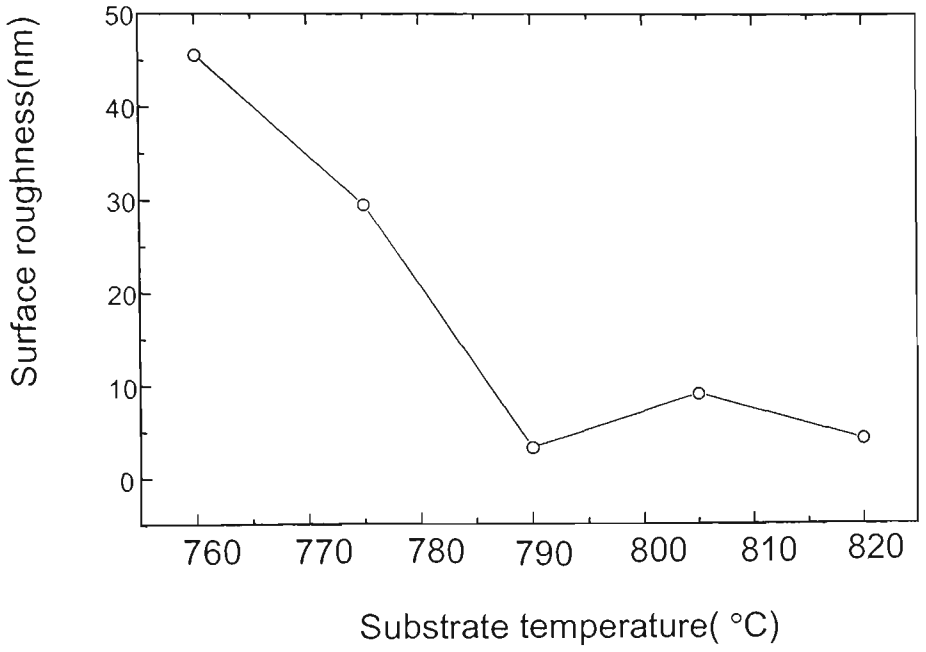

Figure 4.9. Plot of the relationship between substrate temperature and surface roughness for the CeO_2 films of 100nm thickness.

The relationship between thickness and surface roughness is shown in **Fig. 4.10.** There is a critical thickness (200nm) for CeO_2 films, with the surface roughness increasing rapidly above it. This result is consistent with what is seen for CeO_2 on Al_2O_3 films, but in that case the critical thickness is just 90nm. Compared to CeO_2 films on Al_2O_3 substrates [9, 10, 12], the critical thicknesses of CeO_2 films on YSZ is much larger than on Al_2O_3 . The reason for the differences in the critical thickness may be found in the fact that YSZ has a cubic system, whilst Al_2O_3 has a rhombohedral (Hex) system. Although the lattice mismatch between CeO_2 and YSZ (about 5%) is approximately same as that between CeO_2 and the Al_2O_3 R-plane, the angle between the a and b axes of the Al_2O_3 R-plane is not exactly 90°, and this has an influence on the level of dislocations induced in the film. So it can be deduced that not only the lattice mismatch but also the angle between the axes of substrate appears to be important parameters for

epitaxial growth of thin films. Although the critical thicknesses of the CeO_2 films on YSZ and Al_2O_3 substrates are different, the existence of a critical thickness is an intrinsic property of CeO_2 films, which is independent of the nature of the substrate.

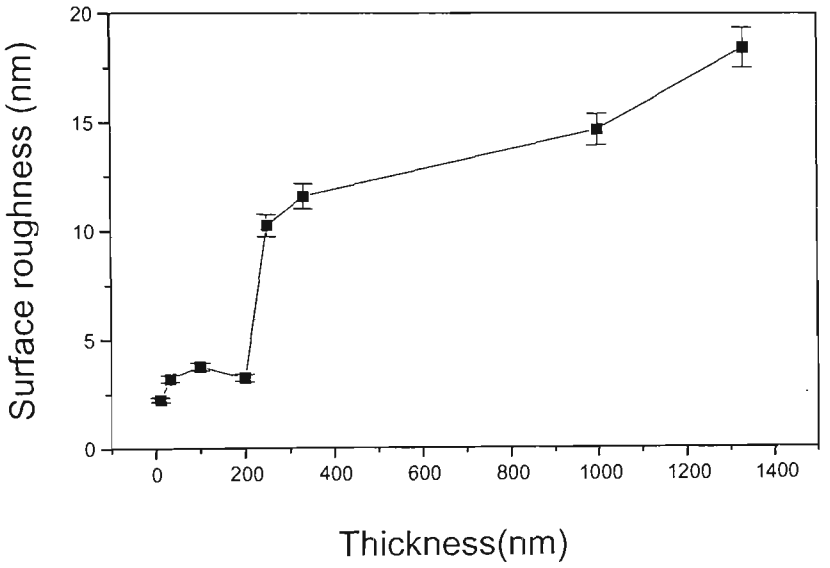

Figure 4.10. Dependence of the roughness of CeO_2 films on thickness for deposition in an O_2 atmosphere at 790°C.

One of the reasons for the roughness of the CeO_2 films becoming worse with increasing thickness is because the outgrowths become larger with increasing thickness. **Fig. 4.11, 4.12,** and **4.13** show the AFM images of CeO_2 films deposited under the same conditions with thicknesses of 100nm, 300nm, and 900nm. It is seen that some small outgrowths are on the surface of the CeO_2 film of 100nm thickness, and the average size of outgrowths on the 300nm film is approximately ϕ260nm×20nm height. **Fig. 4.13** shows similar features but on the 900nm thick film, and the outgrowths now have an average size of approximately 2.5μm×1μm×43nm. From these AFM examinations, it is clear that the average size of outgrowths increases and the density of outgrowth

decreases with increasing thickness. Because the outgrowths are the major contribution to the roughness, this result is consistent with the roughness - thickness relationship shown in **Fig. 4.10**. This property is related to the growth modes of CeO_2 films. The thickness of a CeO_2 film rapidly increases through the critical thickness while the growth mode of the CeO_2 film changes from layer-by-layer growth to island growth. The growth modes of CeO_2 films will be discussed below.

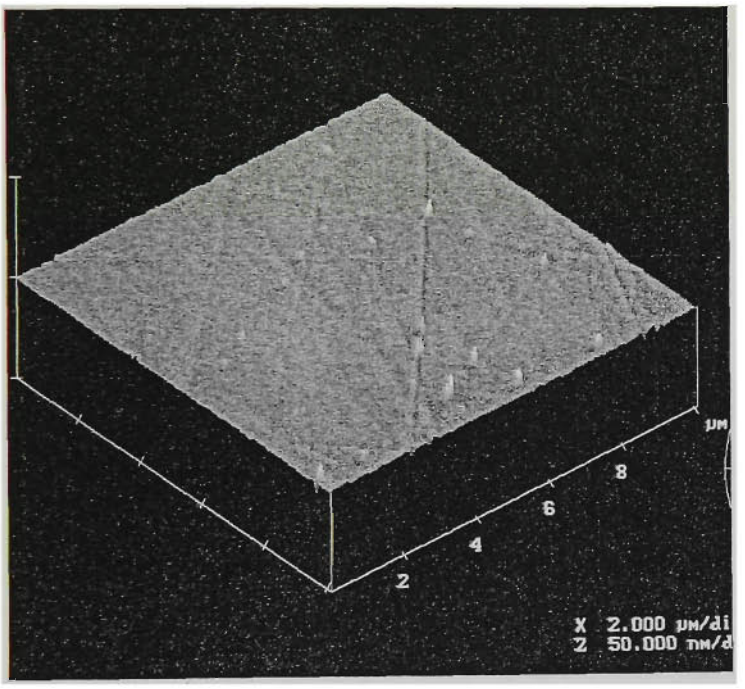

Figure 4.11. AFM surface morphology of a 100nm thick CeO_2 film deposited in 200 mTorr O_2 at 790°C.

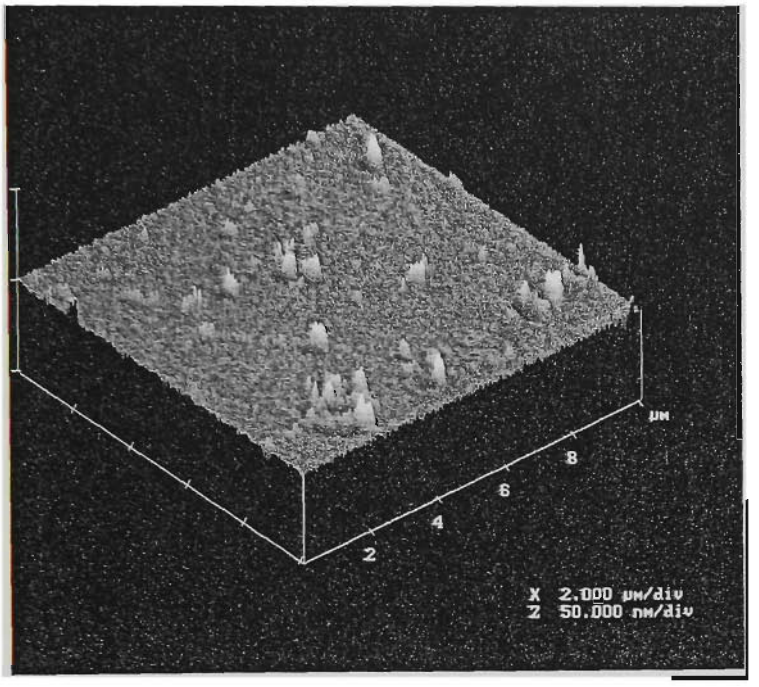

Figure 4.12. AFM surface morphology of a 300nm thick CeO_2 film deposited in 200 mTorr O_2 at 790°C.

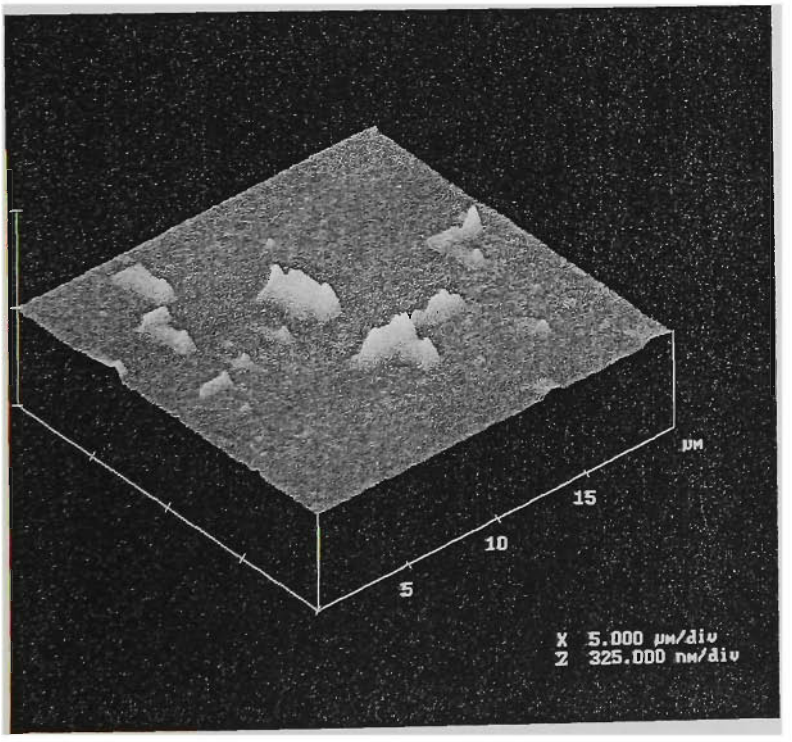

Figure 4.13. AFM surface morphology of a 900nm thick CeO_2 film deposited in 200 mTorr O_2 at 790°C.

Fig. 4.14 shows the relationship between the roughness and laser repetition rates. CeO_2 films of 200nm thickness were deposited at 790°C using a repetition rate of 1, 3, or 5 Hz. The roughness increased with increasing laser repetition rates. This can be explained by the fact that film growth needs time for the mobilization and organization of particles. A low frequency rate of pulsed laser can give the materials time to mobile to a defect free location where the surface energy is smallest and the surface is smooth.

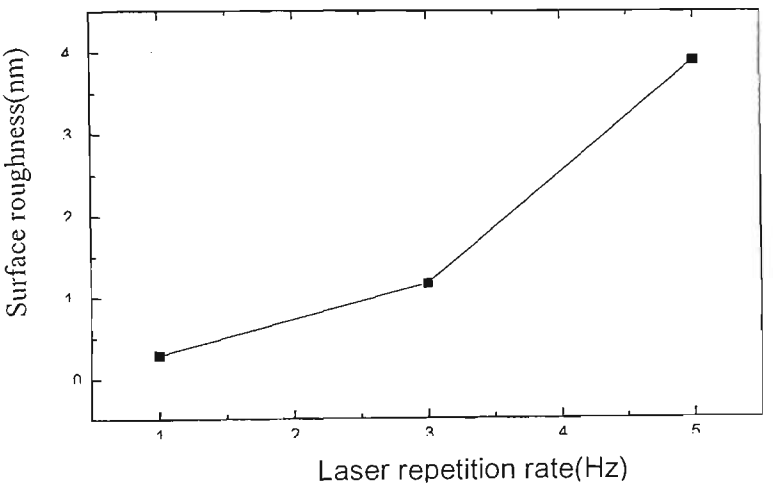

Figure 4.14. The relationship between roughness and laser repetition rate. Film thickness ~200nm, substrate temperature 790°C.

B. Surface morphologies of CeO_2 films deposited using an Ar + 10% H_2 atmosphere

Fig. 4.15 and **Fig. 4.16** are AFM images of CeO_2 films with a 300nm thickness deposited at substrate temperatures of 400°C and 760°C respectively, in 100 mTorr Ar + 10% H_2, with the other deposition conditions unchanged. These surface morphologies

are distinctly different from those films deposited using O_2. For CeO_2 films deposited using O_2, there are many large outgrowths formed as compared to the films deposited under an Ar + 10%H_2 atmosphere. Consequently, the roughness of the former films is larger than the roughness of the latter in which the surface is very smooth (Rms roughness about 2nm) and has very few outgrowths.

The AFM images presented in **Figs.4.11 - 4.13** suggest a strong correlation between the incidence of outgrowth formation and the presence of O_2. We speculate that the surface of the film has a larger mobility in an O_2 atmosphere than for Ar + 10% H_2. Although the large mobility produces large outgrowths, it makes the surface energy smaller and the c-axis orientation better. A smaller mobility means that the atoms of CeO_2 have insufficient time to make a perfect alignment during the deposition process. This is the reason why the c-axis orientation of CeO_2 deposited under Ar + 10% H_2 is worse than that deposited under O_2.

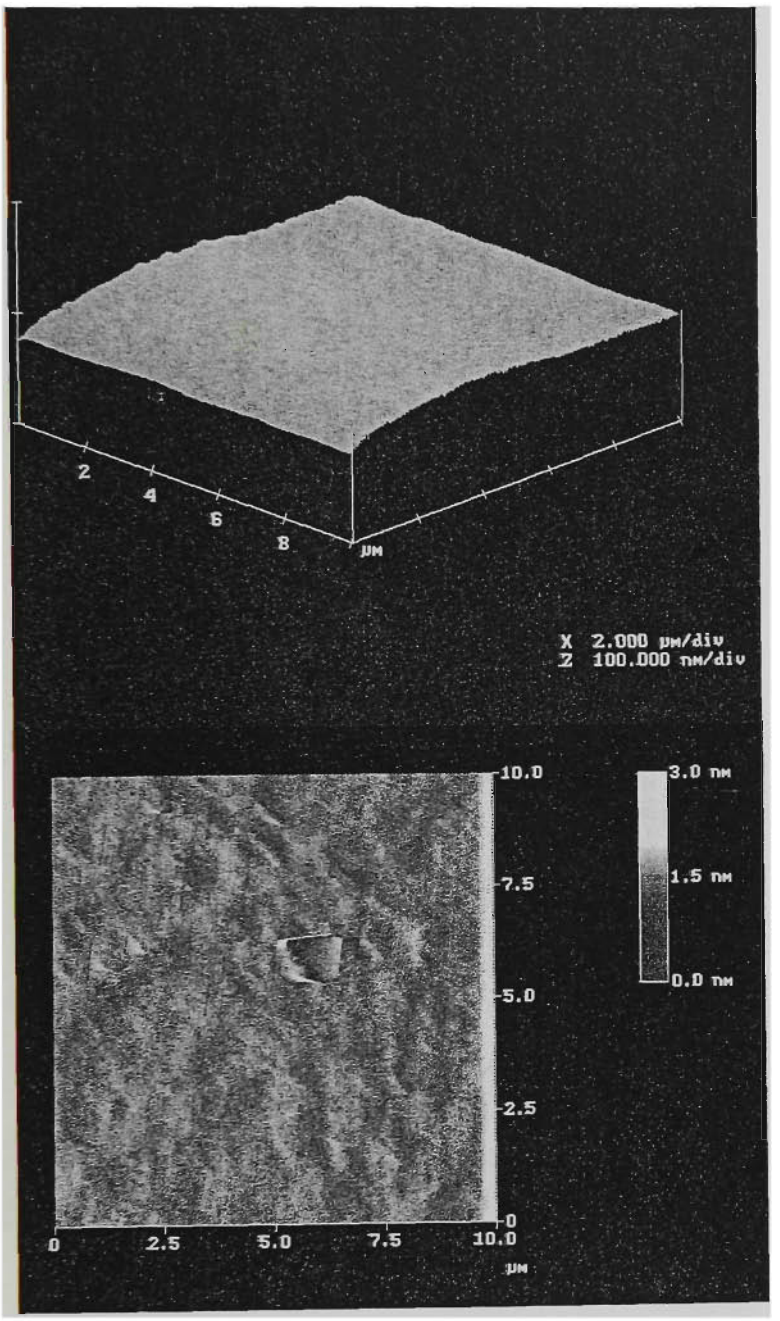

Figure 4.15. AFM 3D and 2D images of the surface morphology of a 300nm thick CeO_2 film deposited at 400°C in Ar+10%H_2.

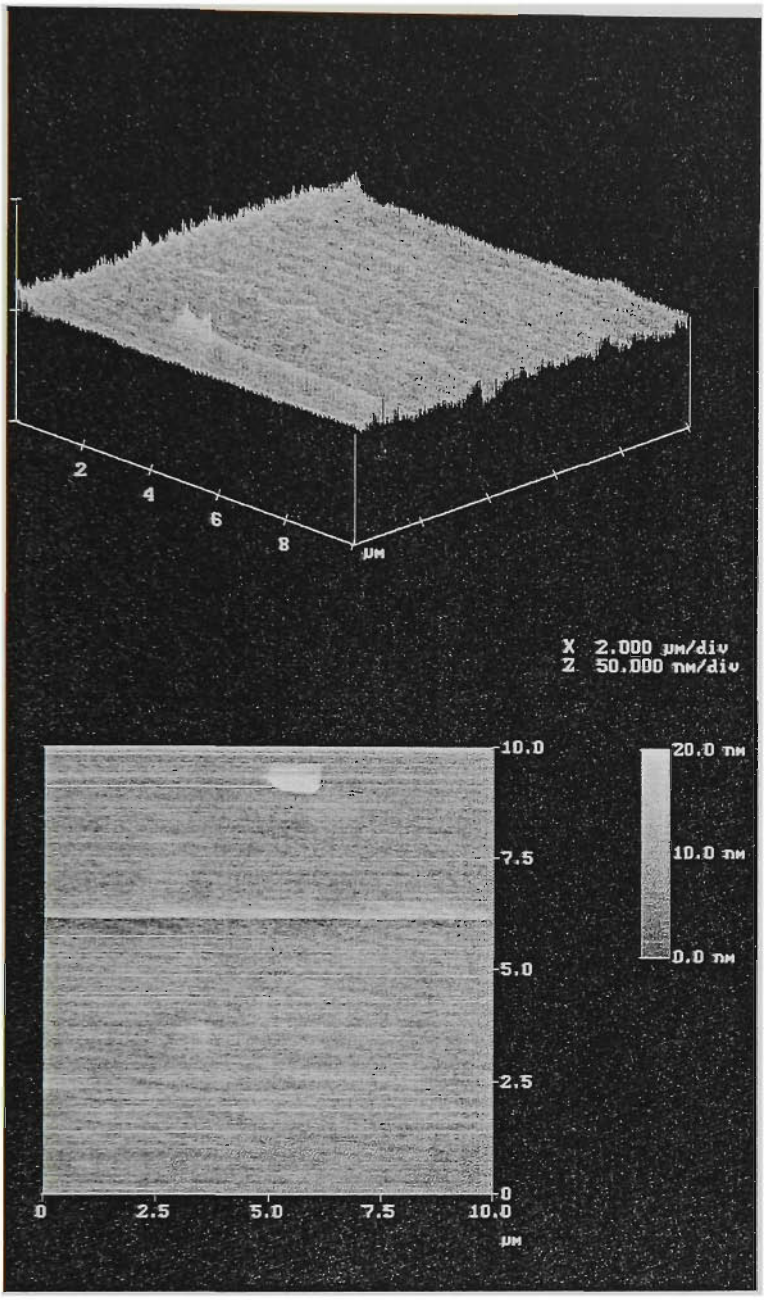

Figure 4.16. AFM 3D and 2D images of the surface morphology of a 300nm thick CeO_2 film deposited at 760°C in Ar+10%H_2.

4. 3. 3. Relationship between grain shape and orientation

The deposition temperature is the most crucial condition for epitaxial growth, apart from the lattice mismatch between the film and the substrate. Pure c-axis CeO_2 films

can be epitaxially grown on singer crystal (001)YSZ substrates over a temperature range of 775 - 805°C, which makes it possible to study the effects of deposition temperature on epitaxial growth of CeO_2 films in detail. The samples studied in this work were deposited under similar conditions except for the temperature.

Three CeO_2 films were produced at different temperatures, all having the same thickness of approximately 100nm: sample A at 775°C; sample B at 790°C; and sample C at 805°C. Sample D was deposited under the same conditions as sample B, except that the thickness was 900nm instead of 100nm.

Pure c-axis oriented CeO_2 films were obtained for all four samples. The dependence of the FWHM value of the XRD ω-scan on the deposition temperature shows a minimum of 0.16° for sample B around 790°C (shown in **Fig. 4.17 (a)**). This value of FWHM of the CeO_2 film is comparable to the corresponding value of the YSZ substrate, of 0.15°. From this result it is inferred that the highest degree of c-axis orientation of CeO_2 film can be obtained at a deposition temperature of 790°C.

The departure from an ideal c-axis orientation is larger for samples A and C, as compared to sample B. This departure was assessed using the FWHM for the (200) reflection obtained in the ω-scan, and the values of FWHMs of samples A and C are 0.19° and 0.18° respectively (shown in **Fig. 4.17(b)** and **Fig. 4.17(c)**)

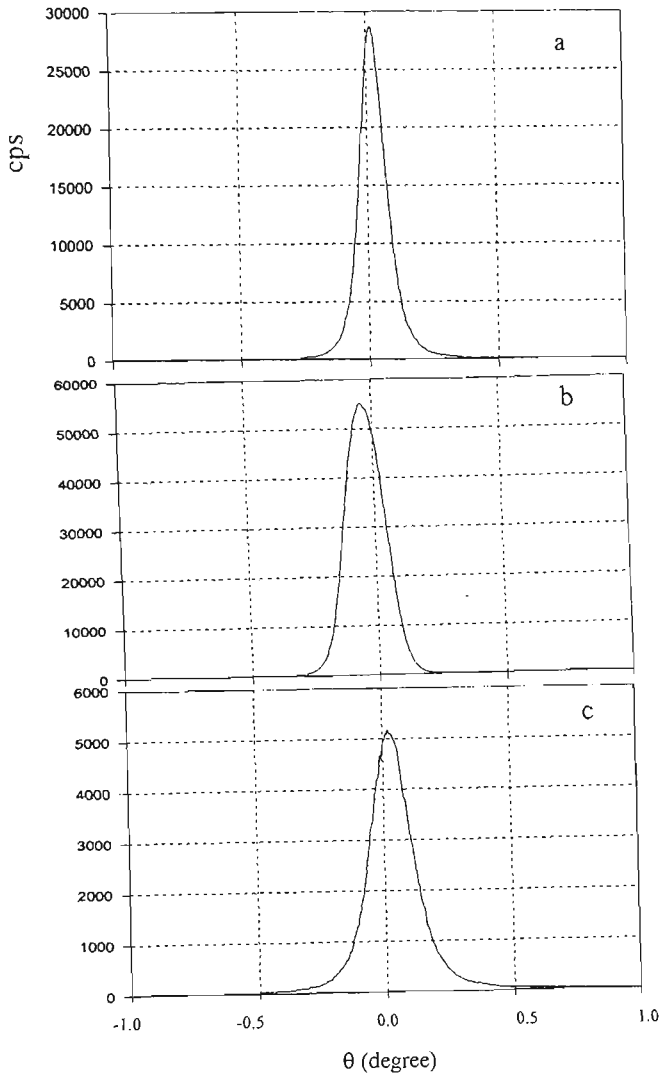

Figure 4.17. ω-scans of (002) diffraction peaks of 100nm samples: (a): sample B; (b): sample A; (c): sample C.

Background morphology was investigated by AFM for all four samples. The result for sample B, which has the highest degree of c-axis orientation, is presented in **Fig. 4.18**. For this deposition temperature, the shape of the CeO_2 grains is approximately round, with an average size of approximately 100nm. The average Rms roughness of this film determined on a scan area of (5×5) μm^2 was 3.62nm. From the cross section profile analysis, shown in **Fig. 4.18(c),** it appears that the top grains are located in the same

layer. The shape of the grains gradually changes from round to square, then to rectangular and mutually perpendicular with increasing the thickness of CeO_2 films deposited at 790°C. The background morphology was completely changed to rectangular at 900nm thickness (shown in **Fig. 4.19**) with a FWHM value of 0.32°.

Identical AFM measurements were performed on samples A and C, and the AFM surface images are presented in **Fig. 4.20** and **Fig. 4.21** respectively. For sample A, which was deposited at the lower end of the epitaxial temperature range, the shape of the grains is approximately square, and the average grain size is approximately 600nm. The average Rms roughness of this sample is 26.42nm, and the cross section profile analysis shown in **Fig. 4.20 (c)** suggests that the top grains are located in different layers.

In the case of sample C deposited at the higher end of the epitaxial temperature range, the shape of the grains appears to be also square-like, but the average grain size is approximately 150nm. The average Rms roughness of this sample is 16.27nm, and the cross section profile analysis shown in **Fig. 4.21 (c)** suggests again that the top grains are located in different layers.

A summary of the data obtained for samples A, B , C, and D is presented in **Table 4.2**.

Table 4.2: Summary of the data obtained for samples A, B , C, and D

Sample	Deposition Temperature [°C]	Thickness (nm)	ω-FWHM [deg]	Rms (nm)	Average Grain Size [nm]	Grain Shape
A	775	100	0.19	26.42	600	Square-like
B	790	100	0.16	3.62	100	Rounded
C	805	100	0.18	16.27	150	Square-like
D	790	900	0.32	18.64	250	Rectangular and mutually respendicular

Develos et al [1,2,3] studied the surface morphology of CeO_2 films deposited by PLD on single crystal Al_2O_3 substrates. In this reference, the film deposited under optimum conditions also has rounded grains, and as the quality of the c-axis orientation deteriorates, the shape of the grains which form the background morphology changes as well.

Wang et al [8] studied the surface morphology of CeO_2 films deposited by metal-organic chemical vapour deposition (MOCVD) on single crystal YSZ substrates. The result of this investigation shows again a correlation between the optimum c-axis orientation of CeO_2 film and the round shape of the grains, as well as a small value of surface roughness.

The results of our investigation, together with the results cited above, suggest that the c-axis orientation of CeO_2 film is related to the morphology of the grains and independent

of the substrate or deposition method; the more rounded the shape of the grains is, the better the c-axis orientation and the smoothness of the CeO_2 film surface are. It appears that this is an intrinsic feature of CeO_2 films, and is related to their growth modes which will be discussed below.

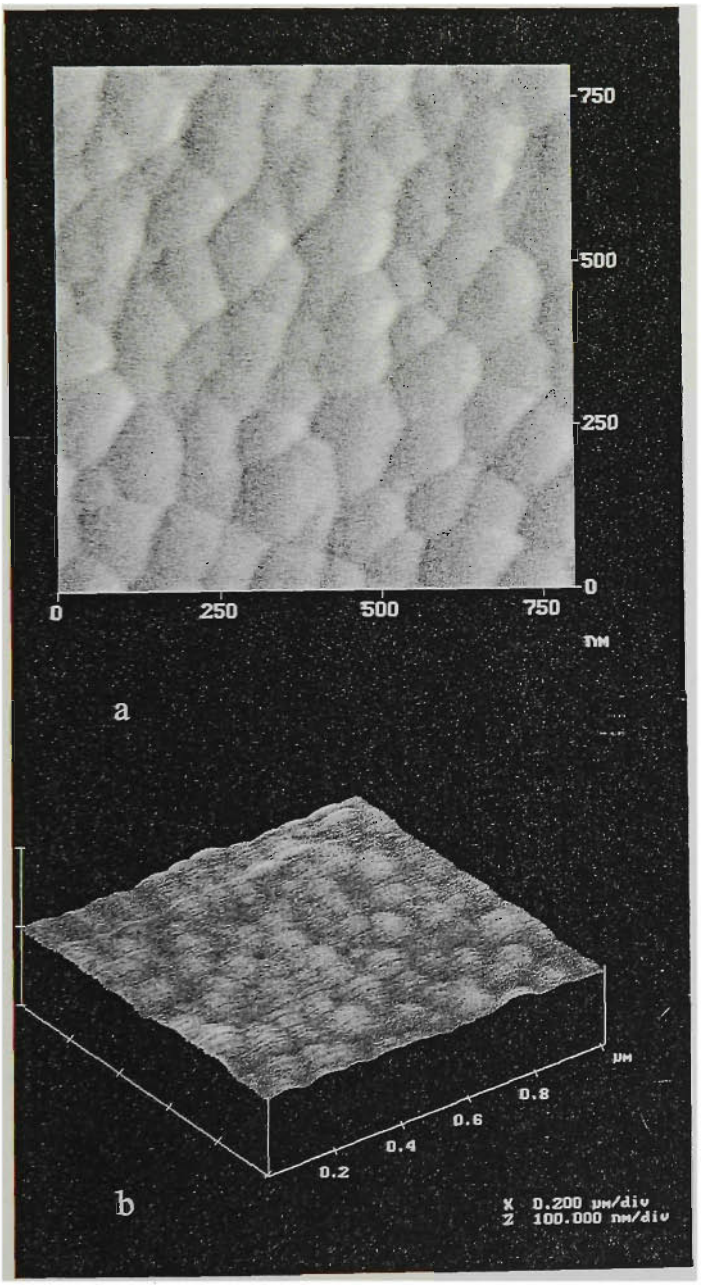

Figure 4.18. AFM images of the CeO_2 film of the sample B. (a): 2D image; (b): 3D image.

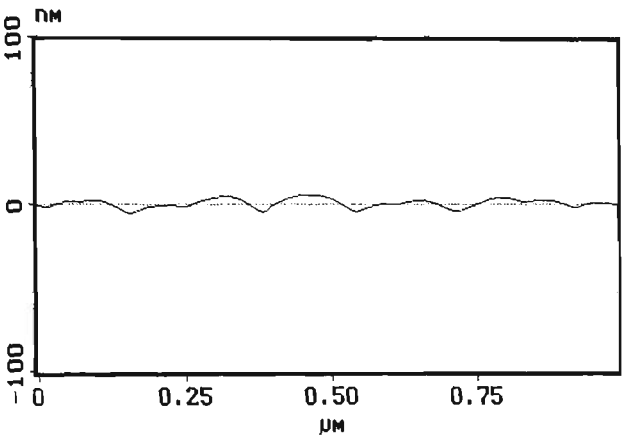

Figure 4.18c. Section profile of the AFM image in Fig. 4.18 (b).

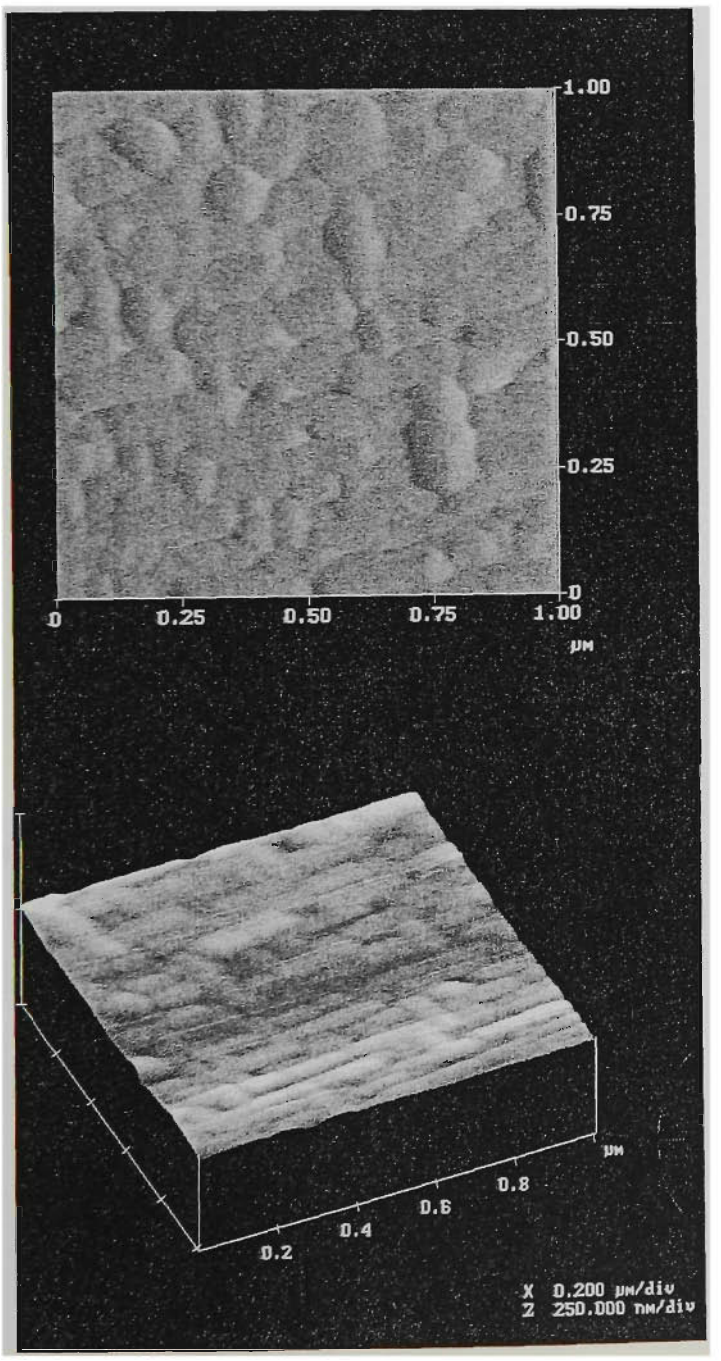

Figure 4.19. AFM images of the CeO_2 film of the sample D. (a): 2D image; (b): 3D image.

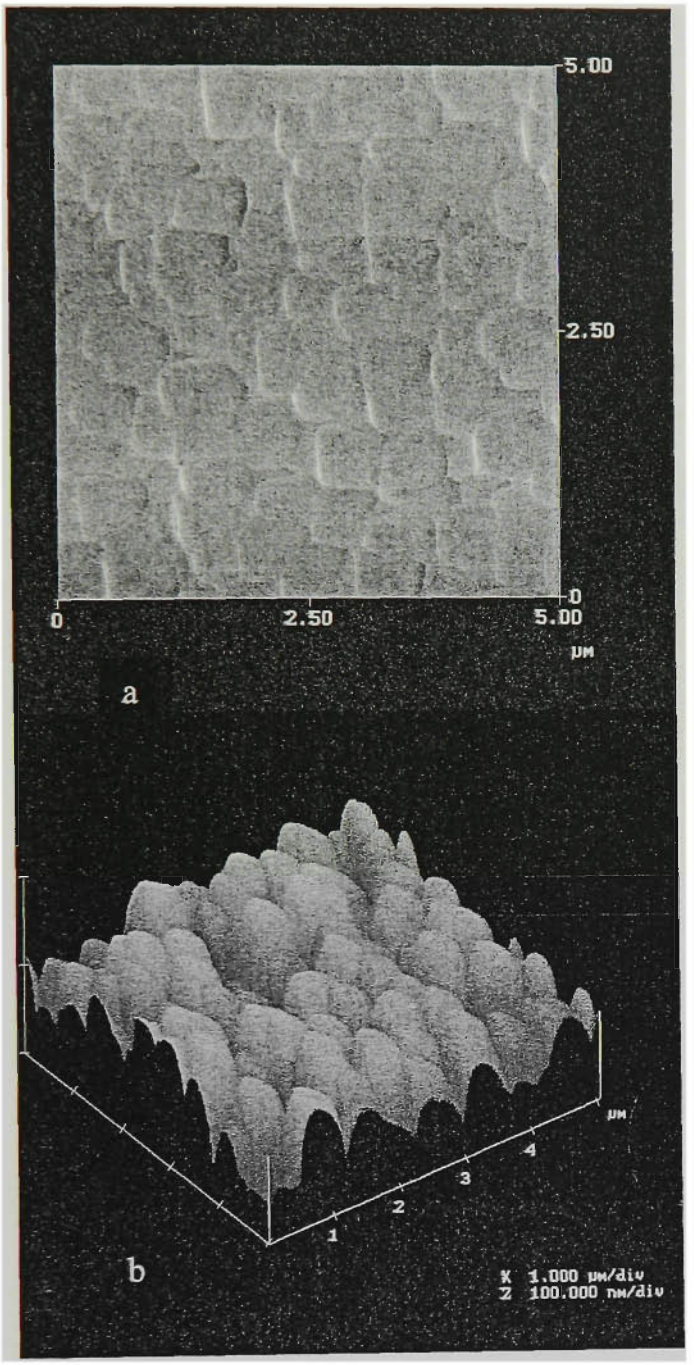

Figure 4.20. AFM images of the CeO_2 film of the sample A. (a): 2D image; (b): 3D image.

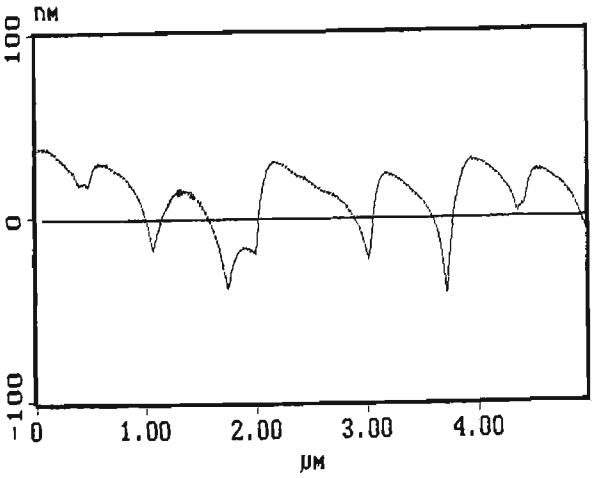

Figure 4.20c. Section profile of the AFM image in Fig. 4.20 (b).

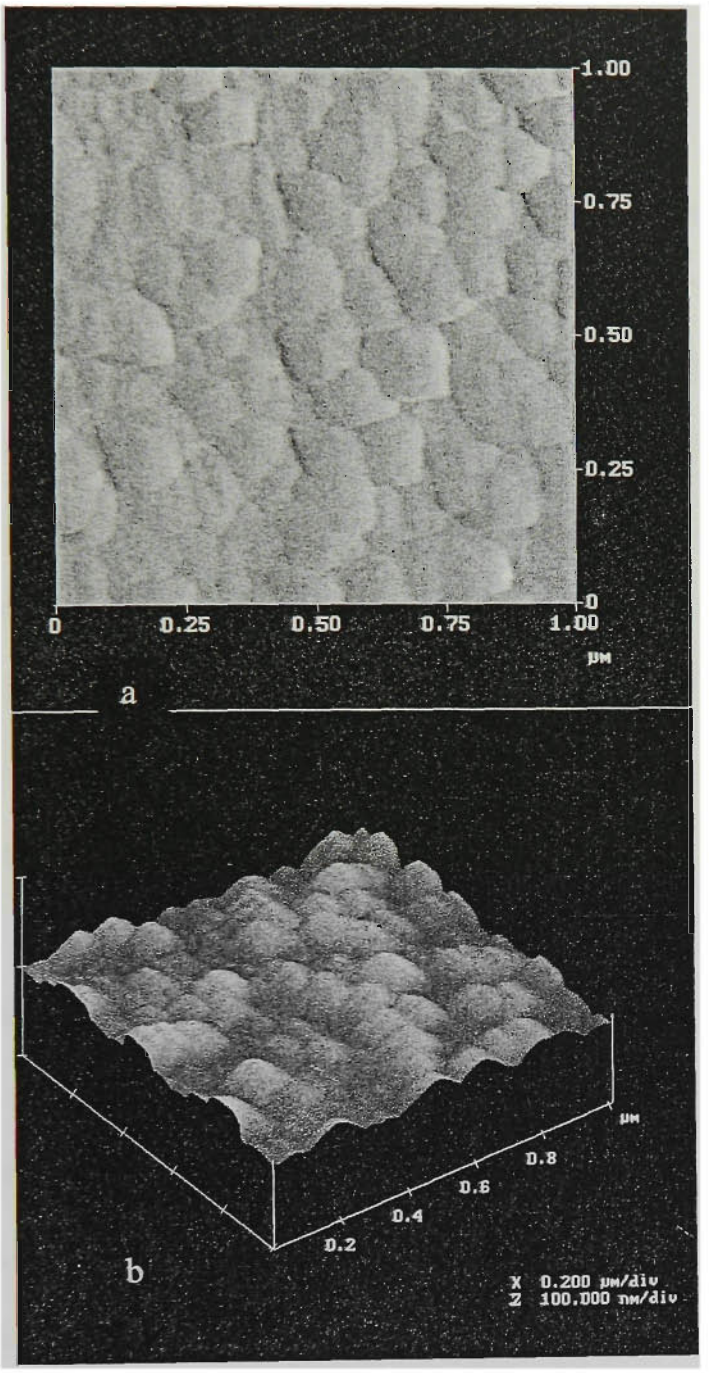

Figure 4.21. AFM images of the CeO_2 film of the sample C. (a): 2D image; (b): 3D

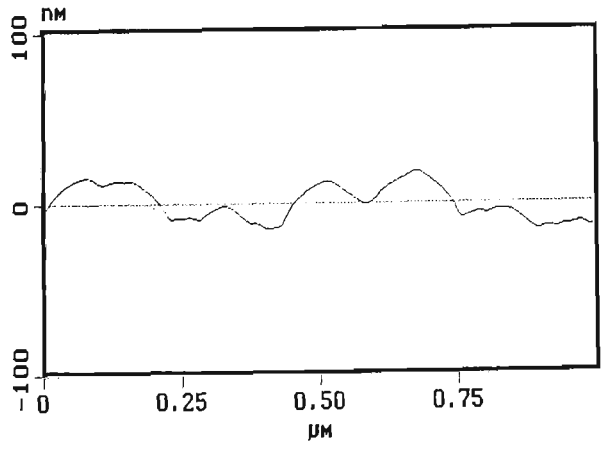

Figure 4.21c. Section profile of the AFM image in Fig. 4.21 (b).

4. 3. 4. Growth modes of CeO_2 thin films

As discussed above, the shape of the CeO_2 grains and the quality of the epitaxy are decided by the deposition conditions. In other words, they are decided by the growth modes which are in turn dependent on the deposition conditions. Generally, a film growth starts from nucleation of deposition species. The nucleation process depends on the interfacial energies between the three phases present: the substrate, the condensing material and the vapour. The minimum-energy shape of a nucleus is like a round cap. The critical size of the nucleus depends on the driving force, i.e. the deposition rate and the substrate temperature. Large nuclei create isolated patches (islands) of film on the substrate, and these subsequently grow and coalesce together.

Besides the temperature and the lattice match, which are the primary influences on the growth mode, other factors such as substrate type, substrate temperature, reactive gas pressure, and flux of the deposition species can also influence the growth. Pulsed laser deposition has some advantages for use in studying growth modes. The non-steady state of pulsed ablation makes it possible to independently control the flux supply for supersaturation and nucleation and the subsequent adsorption migration and growth process.

Generally, there are four growth modes for thin films: layer-by-layer growth (Frank-van der Merwe mode); layer-by-layer, then island or layer-plus-island growth (Stranski-Krastanov growth); island or Volem-Weber growth; and spiral (zero-D) growth [19]. The epitaxial growth of complex oxide thin films, such as HTS and oxide

ferroelectric and magnetoresistive materials, is very complicated, and not yet fully understood. Compared to those complex oxide materials, CeO_2 thin film is simple, and the growth modes of CeO_2 thin films can be studied comprehensively.

During growth of lattice-matched films, a layer-by-layer growth mechanism is usually observed. Besides the group of samples (A, B, C) with the thickness of 100nm, another group of samples (E, F, G) with a thickness of 10nm was analysed. Corresponding to the 100nm samples A, B, C, sample E was deposited at 775°C, sample F at 790°C, and sample G at 805°C. The X-ray diffraction θ-2θ scans for all these samples have only (002) and (004) peaks, showing that the samples have a pure c-axis orientation. The differences between these epitaxial films can be measured by XRD ω-scans of the (002) peaks. The full width at half maximum (FWHM) is similar for all 10nm samples, and smaller than that of the corresponding samples with 100nm thickness (see **Table 2**), which means the epitaxial quality of the CeO_2 films becomes worse as the thickness of the film increases from 10nm to 100nm.

The surface morphologies of the samples were investigated by AFM. The 3D images for samples E, F, and G are presented in **Fig. 4.22**. For these deposition temperatures, the shape of the CeO_2 grains is approximately round, with an average size of approximately 180nm, 200nm, and 170nm, respectively. The Rms roughness of these films for a $5\times5\mu m^2$ scan area was 1.952nm, 1.772nm, and 1.816nm, respectively. It appears that the shape of the grains is rounded, and the top grains are located in the same layer. When a film is grown layer-by-layer, the shape of the grains on the surface

is thus rounded in order to maintain the surface energy smallest. So it can be deduced that films E, F and G are grown by layer-by-layer growth.

For sample B shown in **Fig. 4.18,** a CeO_2 thin film of 100nm thickness deposited under the same conditions as sample F (at 790°C), as analysed above, has approximately round grains on the surface. From the 3D image and the section analysis, shown in **Figs. 4.18 (b)** and **4.18 (c)**, it appears that the top grains are located in the same layer, similar to the 10nm films, indicating the layer-by-layer growth up to the thickness of 100nm in this case.

Samples A and C, as analysed above, were deposited under the same conditions as samples E and G (at 775°C and 805°C) respectively, but grown to a thickness of 100nm. Fig. **4.20** and **Fig. 4.21** of samples A and C show that the shapes of the grains in these films deposited at the lower and higher end of the epitaxial temperature range are approximately square, and the 3D images and section analyses suggest that the top grains are located in different layers. Samples A and C are very different from samples E and G. In these cases, the roughness is much higher, and the shape of the grains has changed from round to almost rectangular. The surfaces of samples A and C consist of grains coming from different layers. So at the deposition temperatures 775°C and 805°C, the CeO_2 films change their growth mode from layer-by-layer growth to island growth, as their thickness increases.

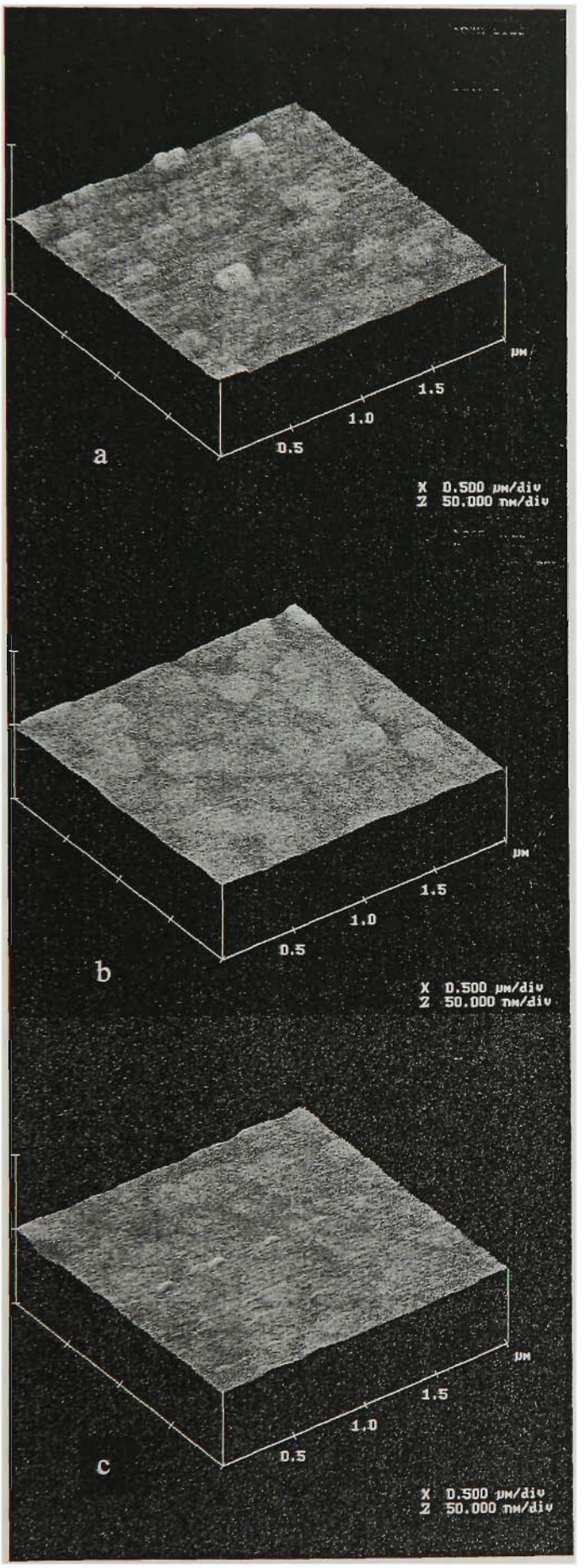

Figure 4.22. AFM 3D images of the CeO_2 films with a thickness of 10nm. (a): sample E; (b): sample F; (c): sample G.

As analysed above, it seems that the layer-by-layer growth can be maintained under a wider deposition temperature range while the films are thin. When the thickness increases, the temperature range for maintaining the layer-by-layer growth becomes narrow. The epitaxial quality becomes lower with worse surface roughness as the growth mode changes from layer-by-layer to island growth, and the shape of grains changes from round to square-like.

Why do the deposition temperature and thickness affect the growth modes? From the point of view of surface mobility, crystalline film growth depends on the surface mobility of the adatoms (vapour atoms). Normally, the adatom will diffuse through several atomic distances before sticking to a stable position within the newly formed film. The surface temperature of the substrate determines the atom's surface diffusion ability. An optimum epitaxial temperature favours defects free crystal growth, whereas at lower and higher temperatures crystal growth may be overwhelmed by energetic particle impingement, resulting in large islands and the growth shifting from layer-by-layer to island growth.

From the point of view of interface energy, the growth mode is decided by the interface energy between the film and substrate from the beginning of deposition [20]. In principle, this energy always increases with an increase in thickness. There is a threshold interface energy at which layer-by-layer growth changes to island growth. When the interface energy increases slowly as the film thickness increases, so that the interface energy stays below the threshold, the film can stay in a layer-by-layer growth

mode all the way, as in the case of sample B. Conversely, once the threshold has been passed, the growth of the film will change to island growth, as in samples A and C.

From the above study, it can be inferred that the interface energy of the best epitaxial film is the smallest. The interface energy is closely dependent on the strain arising from the lattice mismatch between the film and the substrate. In sample B, the optimum epitaxial temperature made the energy of the first layer of the CeO_2 film on YSZ lower than for samples A and C because the better match at the interface reduced the strain in every layer of the CeO_2 film. This made the CeO_2 layers smooth from the first mono-layer, and the interface energy increased so slowly as the film thickness increased that the whole growth process was governed by layer-by-layer growth.

It is a general rule that the growth mode for a CeO_2 film changes from layer-by-layer growth to island growth with increasing thickness, even for an optimum epitaxial growth. **Fig. 4.23** shows the AFM images of a CeO_2 film with the thickness of 1300nm deposited using the same optimum deposition conditions as for samples B and F. From the AFM images, it is clearly seen that large islands had been formed in the top layer of the CeO_2 film, and the growth mode eventually changes to typical island growth.

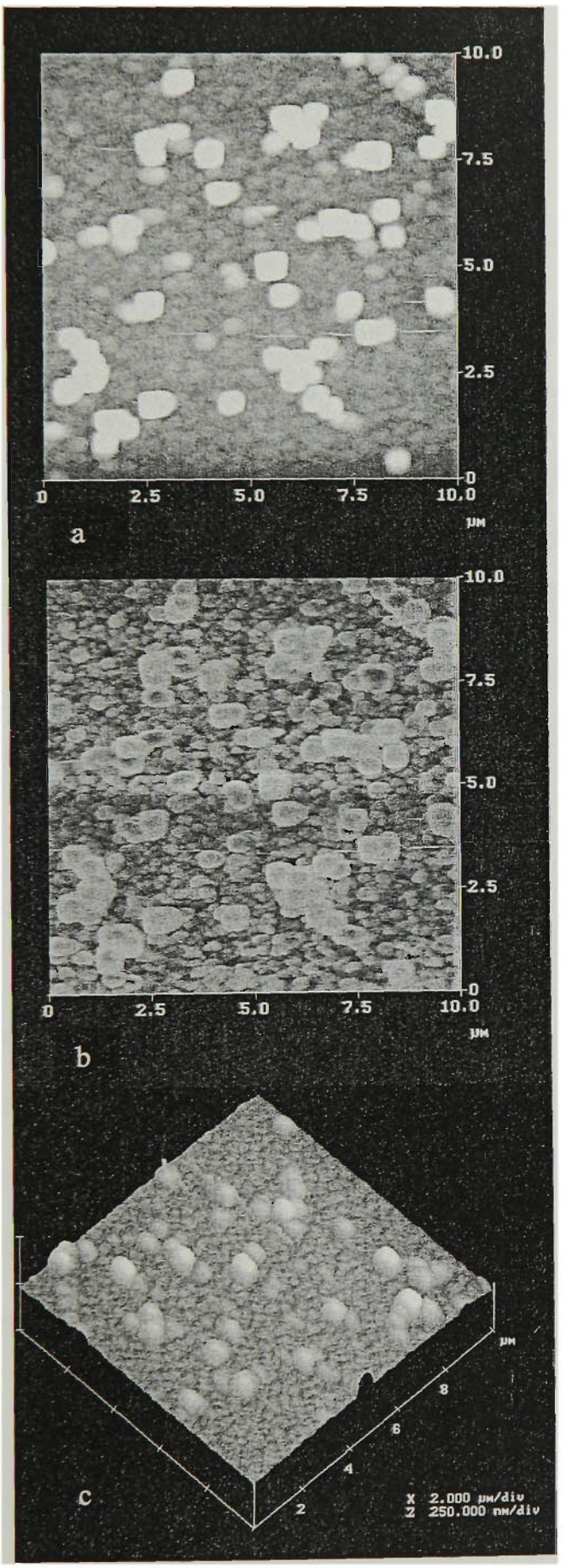

Figure 4.23. AFM images of a CeO_2 film with the thickness of 1300nm deposited under the optimum deposition condition. a: height mode image; b: friction mode image; c: 3D image.

The film deposition was extended from epitaxial growth to imperfect c-axis oriented growth. Sample H is a CeO_2 film of 900nm thickness deposited under the same conditions as the other samples except that the deposition temperature was 750°C. **Fig. 4.24** is an XRD θ-2θ scan of sample H, showing that the CeO_2 film has a small (111) diffraction peak because the temperature is slightly beyond the epitaxial temperature range. The degree of c-axis orientation, as given by Ic = I(200)/(I(111)+I(200)), is 95.4%, and the FWHM of the ω-scan for (200) is 0.37°. **Fig. 4.25** presents 2D and 3D AFM images and a section analysis of sample H, which show that the shape of the grains is completely rectangular. The Rms roughness of this sample is 32.72nm. There are plenty of outgrowths on the surface, with the size about $1.49\times0.46\mu m^2$ base and 72.94nm height. In **Fig. 4.25,** it can be seen the outgrowths prefer to connect to each other to form a network.

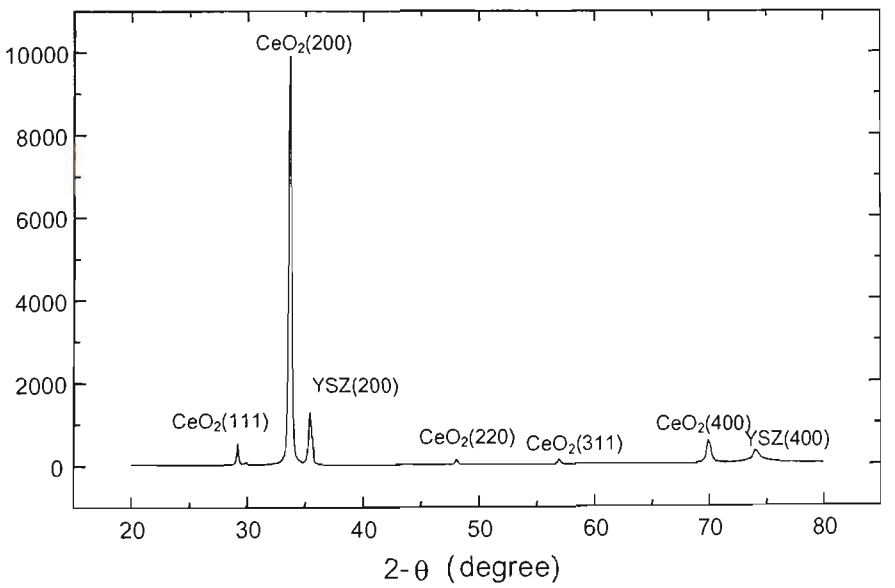

Figure 4.24. XRD θ-2θ scan for the CeO_2 film of the sample H.

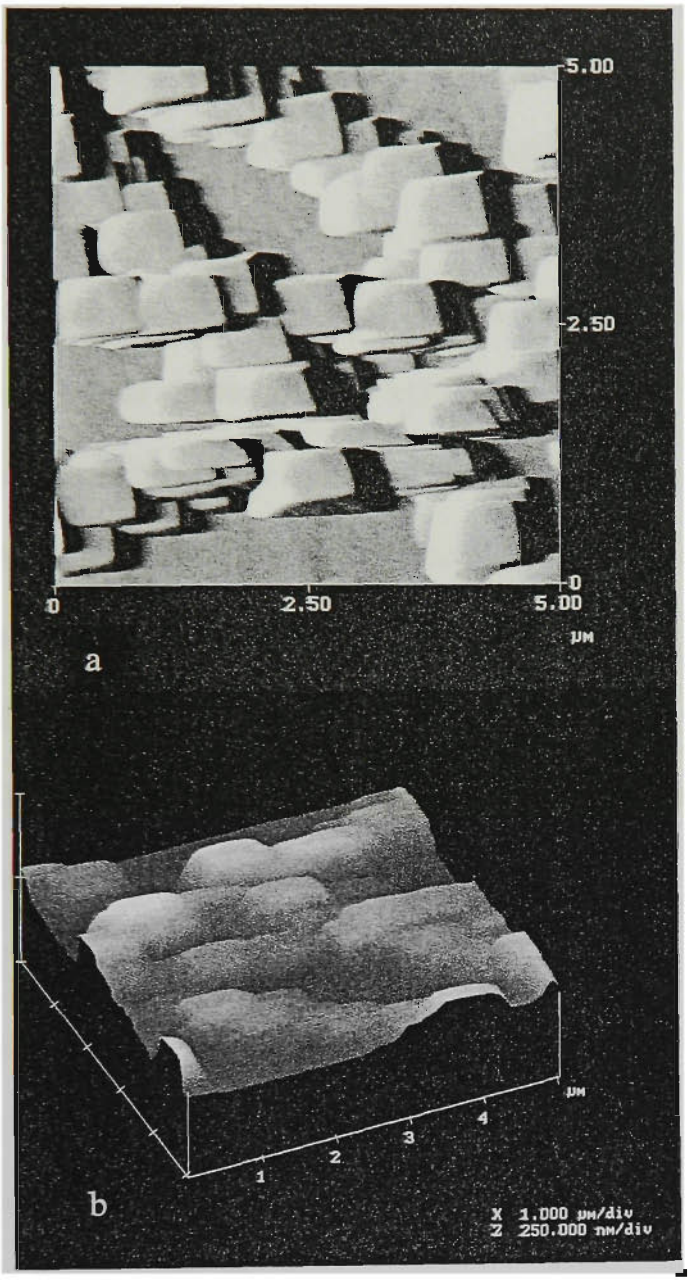

Figure 4.25. AFM images of the CeO_2 film of the sample H. (a): 2D image; (b): 3D image.

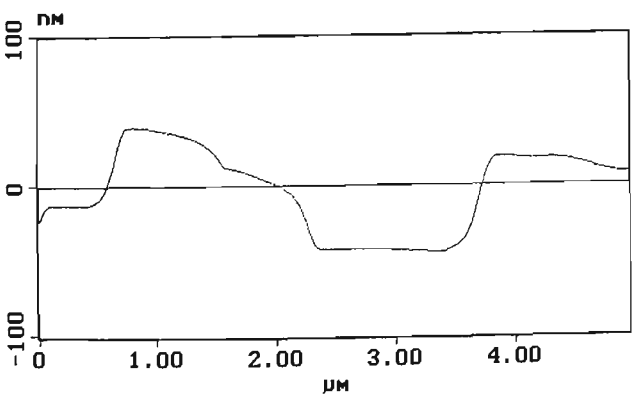

Figure 4.25c. Section profile of the AFM image in Fig. 4.25 (b).

In the case of sample H, the decreased deposition temperature means that there was not enough energy at the surface to rearrange the species as they are deposited. The deposited materials bind together in some nucleation sites from the beginning of deposition, and the size of islands increases quickly with increasing the film thickness. Small islands eventually develop into large outgrowths, which result in a large number of outgrowths on the final surface of the CeO_2 film and a very high surface roughness. The interface energy of this sample increased so rapidly that the growth is typical island growth throughout. **Fig. 4.26** shows a schematic diagram of the island growth of sample H. Film growth starts with nucleation of ablated species on the substrate's surface. Extensive ripening and low surface mobility due to the lower deposition temperature considerably delay the growth and increase in size of the islands. When the surface becomes completely covered by the film, further deposition leads to the formation of the larger islands (outgrowths) through coalescence. In the development of deposition, the outgrowths connect into a network due to lacking surface mobility [21].

Island growth seriously influences the morphology of films, especially because of the existence of the large islands. Connected networks of large outgrowths on the surface are an important factor that makes the surface roughness of sample H worse.

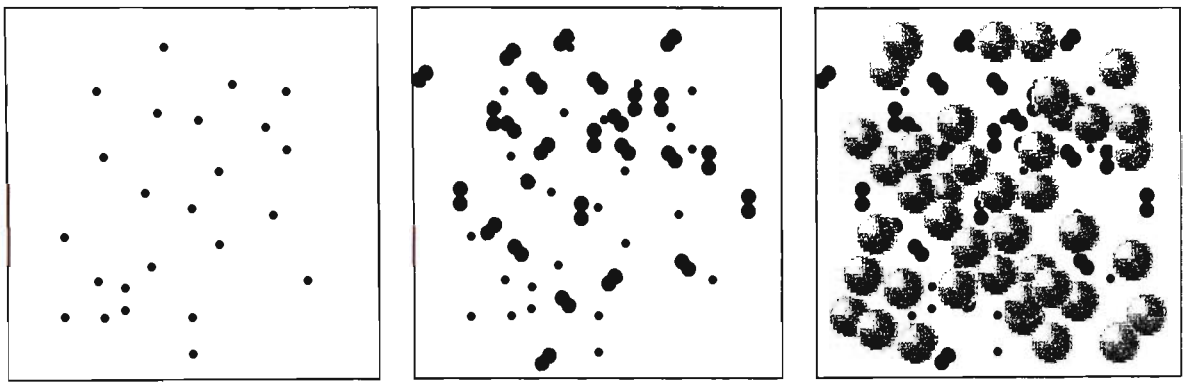

(a) Nucleation

(b) Dissociation and formation of islands

(C) Island growth

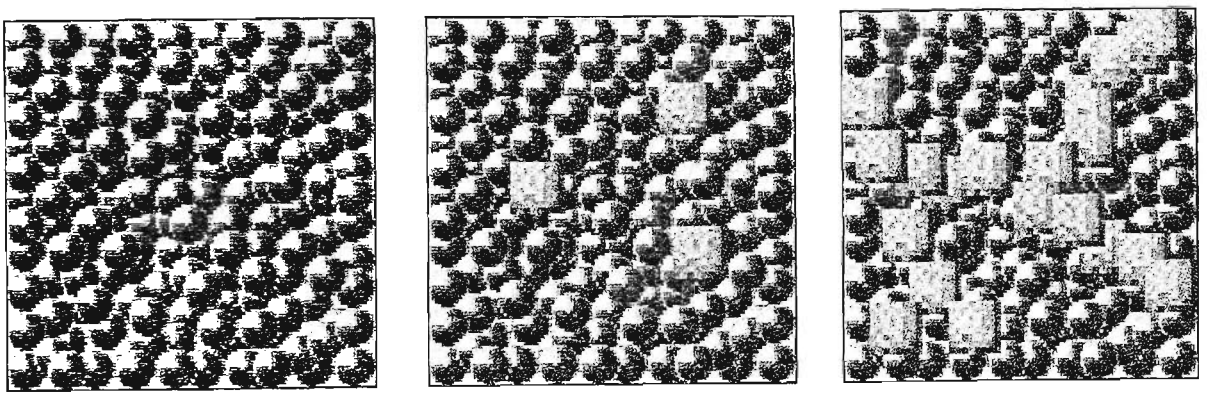

(d) Complete coverage of surface

(e) Formation of large islands (outgrowths)

(f) Outgrowths connect into networks

Figure 4.26. Schematic illustration for the island growth of the CeO_2 film of the sample H deposited at low temperature.

Sample I is a CeO_2 film of 900nm thickness deposited under the same conditions as the other samples except for the deposition temperature, which in this case was 700°C, far away from the epitaxial temperature range. **Fig. 4.27** gives an XRD θ-2θ scan of the sample, showing that the CeO_2 film has a strong (111) diffraction peak. The degree of c-axis orientation was evaluated by I_c=I(200)/(I(111)+I(200)) is 54.1%. The FWHM of

the ω-scan for (200) is 1.46°. **Fig.4.28** presents its AFM images which show that the shape of the grains is completely rectangular. The average Rms roughness of this sample is 94.57nm. There are numerous outgrowths on the surface, and their size is approximately $1.50\times1.10\mu m^2$ base, 180nm height. **Table 4.3** summaries the analysed data on samples E, F, G, H, and I.

Fig. 4.28(b) gives a detailed image of the outgrowths of sample I. The image clearly shows many terraces located around the outgrowths. The terraces associated with the outgrowths are caused by the continuous layer-by-layer growth of the outgrowths. This is because the deposition temperature was so low that the deposited materials did not have enough mobility energy to move away from the outgrowths. In the case of sample I, the film growth has developed into the typical terrace-ledge-kink growth mode for a cubic crystal, and this made the outgrowths grows very large [22].

In YBCO thin film deposition, spiral growth is commonly observed [23]. However, in CeO_2 thin film deposition, spiral growth has never been observed to the best of my knowledge. The other three growth modes have been observed, and they have definite relationship with the epitaxial quality of CeO_2 film.

Table 4.3 A summary of the data obtained for the samples of E, F, G, H, and I

Sample	Deposition Temperature (°C)	Thickness of films (nm)	FWHM of ω-scan (°C)	Rms (nm)	Average Grain size (nm)	Grain shape
E	775	10	0.16	1.95	180	Round
F	790	10	0.15	1.77	200	Round
G	805	10	0.15	1.82	170	Round
H	750	900	0.37	32.72	1000	Square and networks
I	700	900	1.46	94.57	1500	Square and terrace

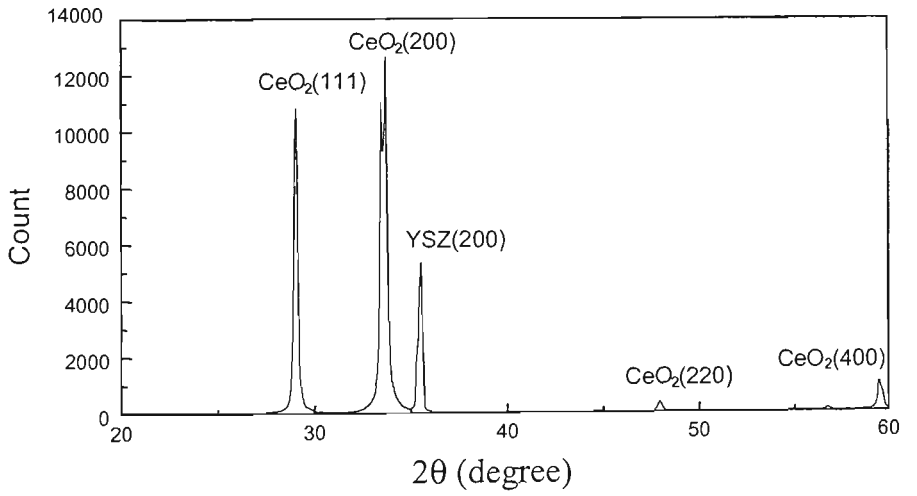

Figure 4.27. X-ray θ-2θ scan for the CeO_2 film of the sample I.

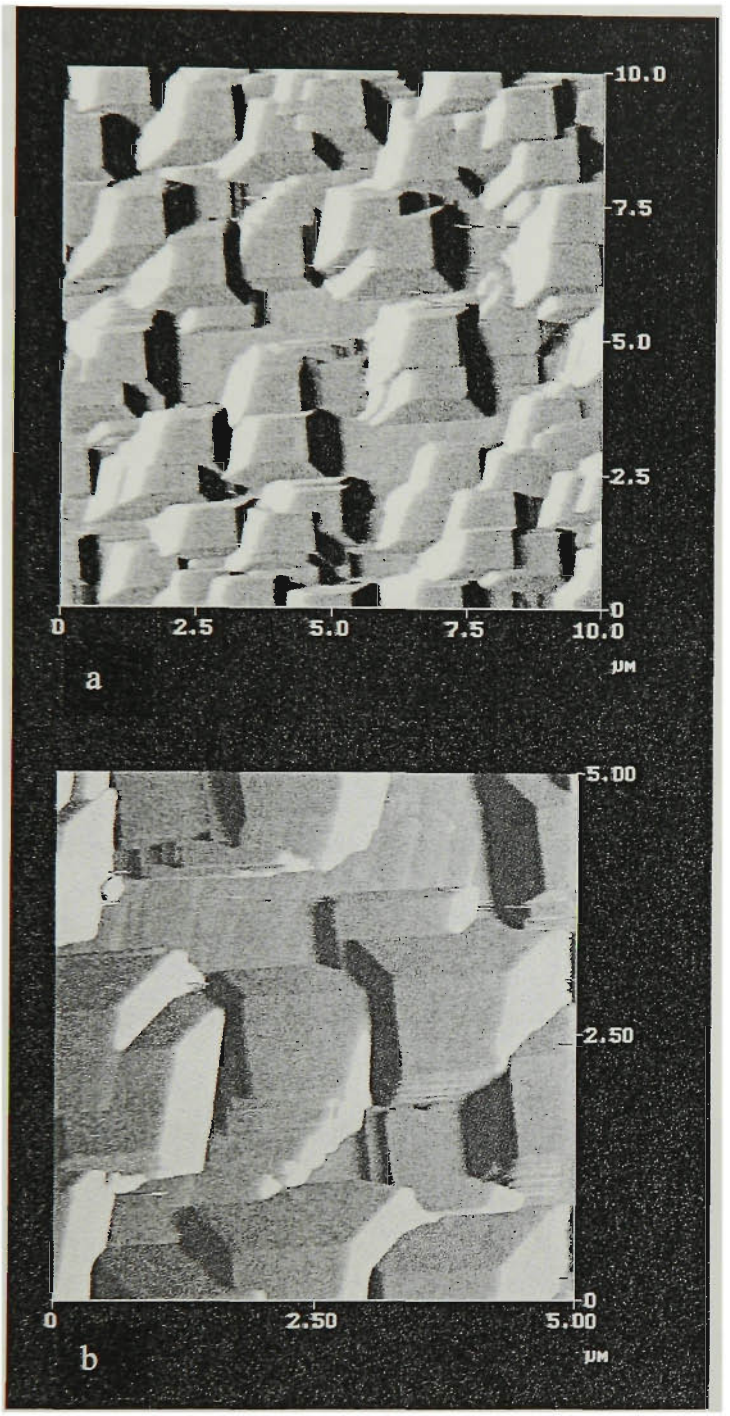

Figure 4.28. AFM images of the CeO_2 film of the sample I. (a): 2D image; (b): The details of outgrowths.

4. 3. 5. Relationship between the surface morphology of CeO_2 films and the condition of YSZ substrates

A. Linear outgrowths and linear grooves on the surface of CeO_2 films with different thicknesses

From the analysis above, it can be seen that there are many outgrowths aligned into lines and linear grooves on the surface of CeO_2 films (**Fig.4.12** and **4.13**). What is the reason for the existence of linear outgrowths and linear grooves? To find a answer we first used AFM to analyse the surface morphology of CeO_2 films with different thicknesses. The thickness range investigated is from about 3nm to 300nm. **Fig. 4.29, 4.30, and 4.31** show AFM images of CeO_2 films with thicknesses of 3.7nm, 33nm, and 300nm, respectively, which were deposited under the optimum epitaxial growth conditions: 200mTorr O_2; 3Hz; 790°C. In **Figs. 4.29(a)** and **4.29(b)**, the morphologies consist of linear grooves and linear outgrowths.

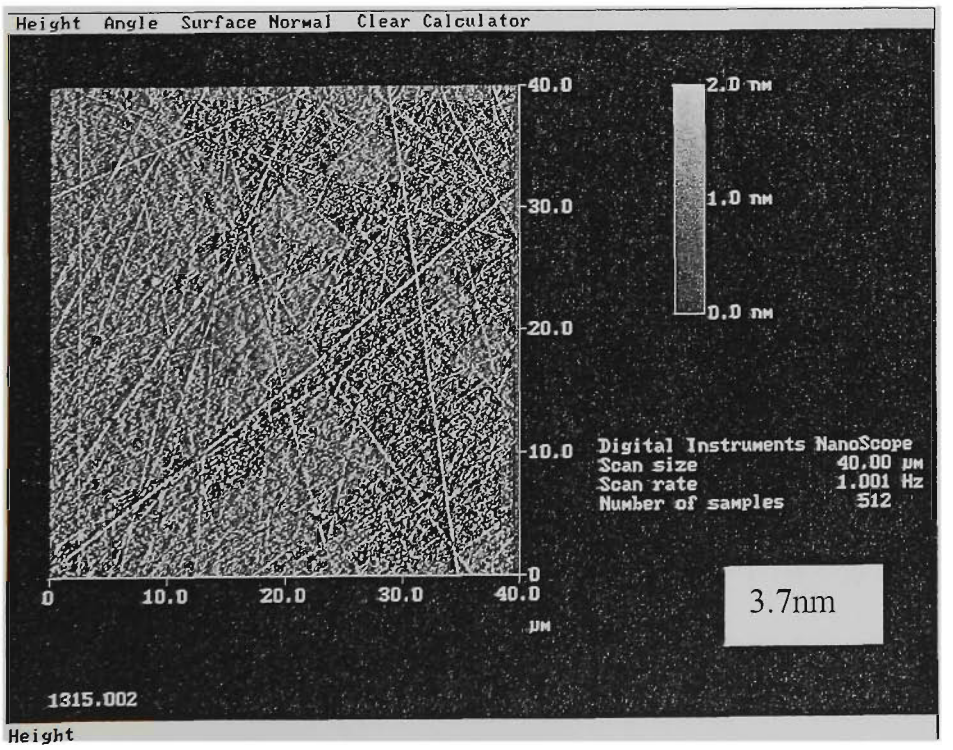

Figure 4.29 (a) AFM image of a CeO_2 films on a YSZ substrate for an area of 40×40μm^2. There are many linear outgrowths.

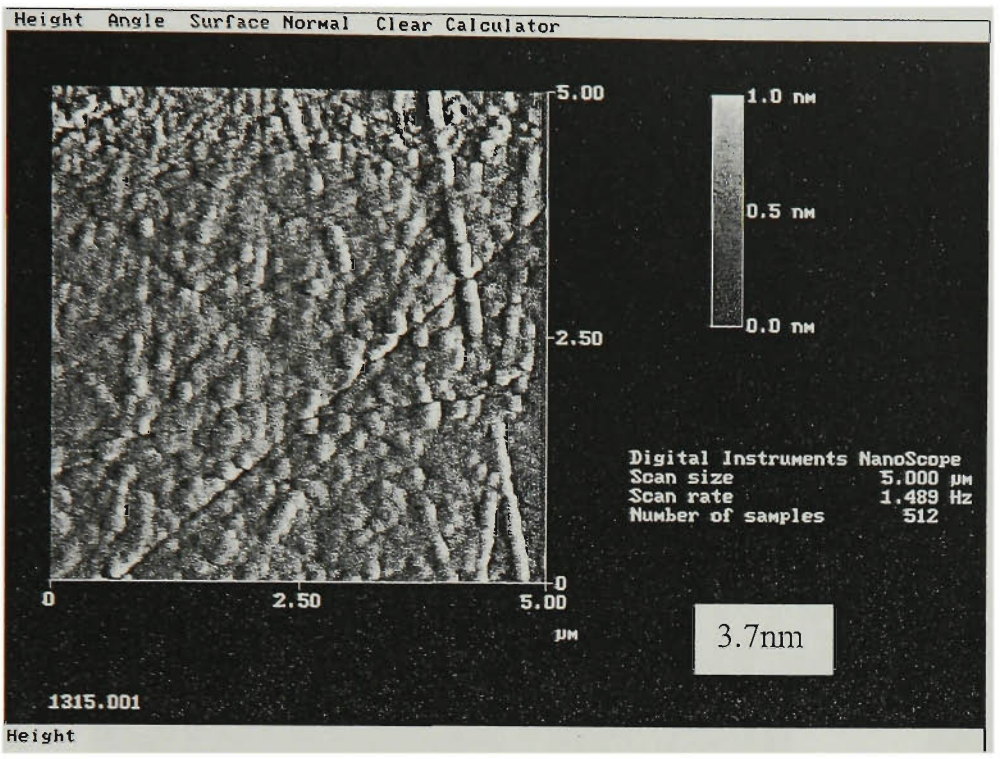

Figure 4.29 (b) AFM image of a CeO_2 film on an YSZ substrate for an area of $5\times5\mu m^2$. Besides numerous linear outgrowths, it can be clearly seen that there are several linear grooves.

Figs. 4.30 (a) and **(b)** show the morphologies of a CeO_2 film with 33nm thickness. From **Fig. 4.29(a)**, it can be seen there are two kinds of outgrowth. One is linear outgrowth, while another is singular outgrowth which is much higher than that of linear outgrowth. Singular outgrowth can easily be seen in the section profiles, whereas the linear grooves and the linear outgrowths can be clearly seen in the images, but the depth of the grooves and the height of outgrowth is very small compared to singular outgrowths and hard to distinguish from the section analysis. For example, in this case, the depth of grooves is 1.25nm, and the height of the liner outgrowths is 3.4nm, but the average height of singular outgrowths is approximately 30nm. From **Fig. 4.30 (b)**, it can be clearly seen that the linear outgrowths also consist of many small individual outgrowths.

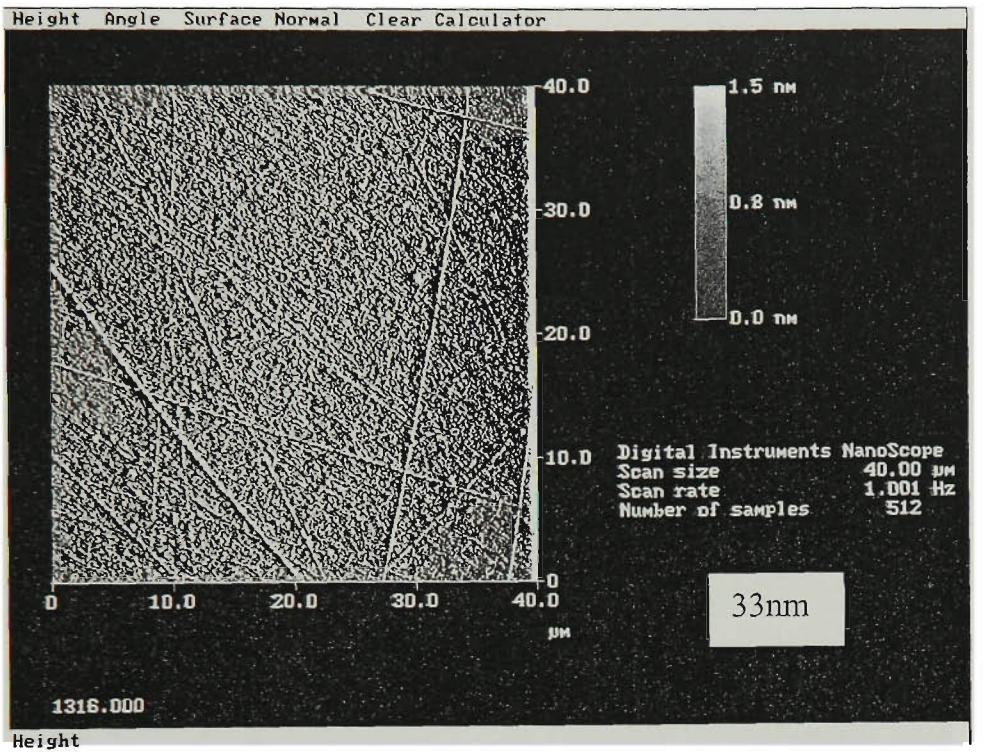

Figure 4.30(a). AFM image of a CeO_2 film on an YSZ substrate for an area of 40×40μm^2. There are many linear outgrowths and singular outgrowths

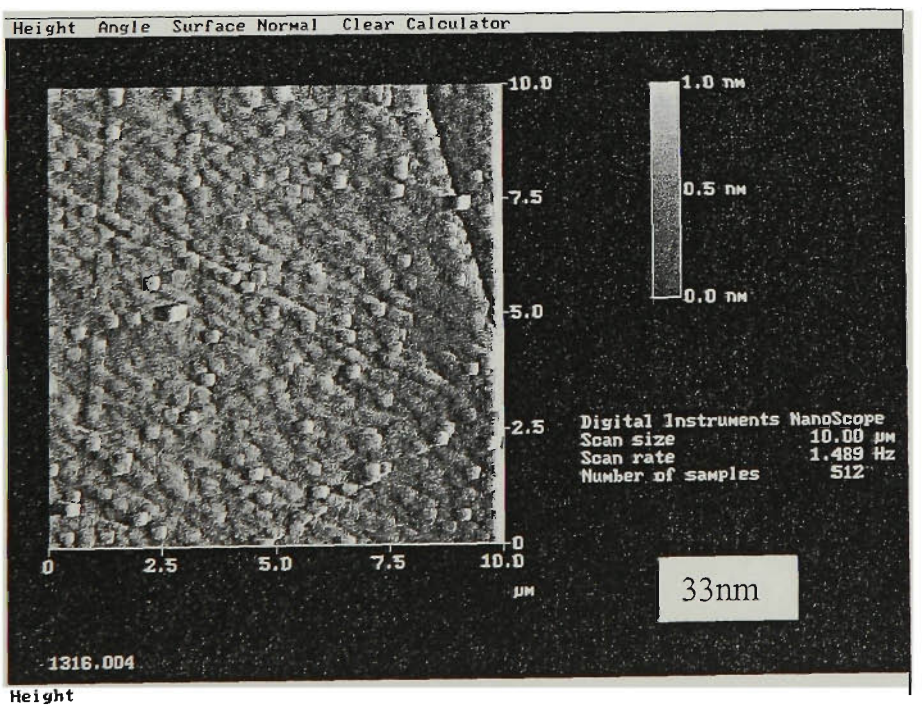

Figure 4.30 (b) AFM image of a CeO_2 film on an YSZ substrate for an area of 10×10μm^2. There are some linear outgrowths, singular outgrowths (white spots) and linear grooves. It can be clearly seen that the linear outgrowths consist of many small round outgrowths.

Fig. 4.31 shows the morphology of a CeO_2 film with 300nm thickness. It can be seen that there are singular outgrowths, linear outgrowths and linear grooves. Many large singular outgrowths occur at the location of the linear grooves.

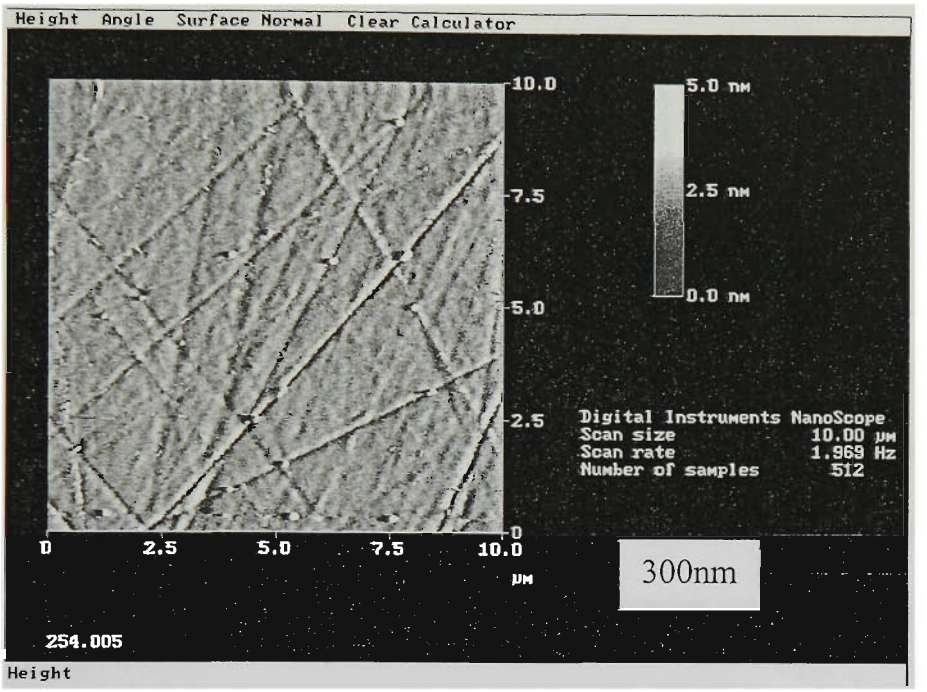

Figure 4.31 AFM image of a 10×10µm² area of a CeO_2 film with 300nm thickness on an YSZ substrate. There are many linear outgrowths, singular outgrowths and linear grooves. It can be clearly seen that many large singular outgrowths are located on the linear grooves.

B. The correlation between the linear outgrowths and the polishing scratches on the surface of YSZ substrates

Because the location of the linear outgrowths and linear grooves is random, the pattern looks very much like the images of polishing scratches on substrates. It is natural to wonder if there is some relationship between polishing scratches and linear outgrowths and linear grooves. In order to confirm it, a CeO_2 sample was made using the procedure

shown in **Fig. 4.32.** First, an YBCO film was deposited on YSZ under the following conditions: 200mTorr O_2; pulsed laser at 3Hz and 500mJ; 5cm distance between target and substrate; deposition temperature 790°C. The YBCO thickness is about 200nm. After the deposition, the YBCO film was annealed at 450°C in ~1 atm O_2 for 30min. The YBCO/YSZ sample was patterned and etched in H_3PO_4, leaving alternate bands of YBCO and bare substrate. A CeO_2 film was deposited on top of this. The sample was then etched again in H_3PO_4, leaving this time alternate bands of CeO_2 and bare substrate. The CeO_2 films crossing the steps were observed using AFM. From **Fig.4.33**, it can be easily seen there are some linear images that continue from the substrate cross the CeO_2 step. These linear images are polishing scratches on the substrate, and represent linear outgrowths on the surface of the CeO_2 film. It is clearly shown that some linear outgrowths are correlated with the polishing scratches on the substrate.

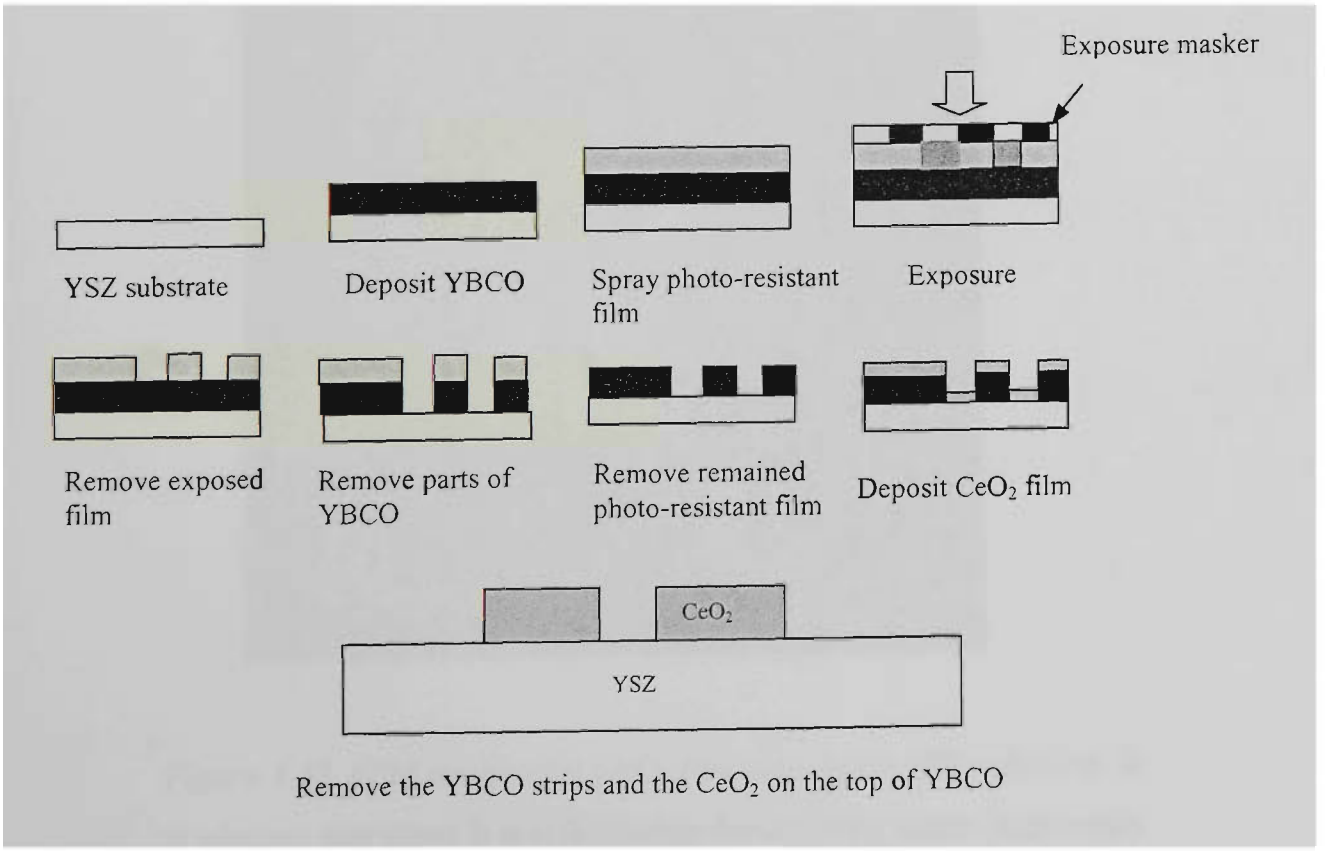

Figure 4.32. Fabricating CeO_2 straps on an YSZ.

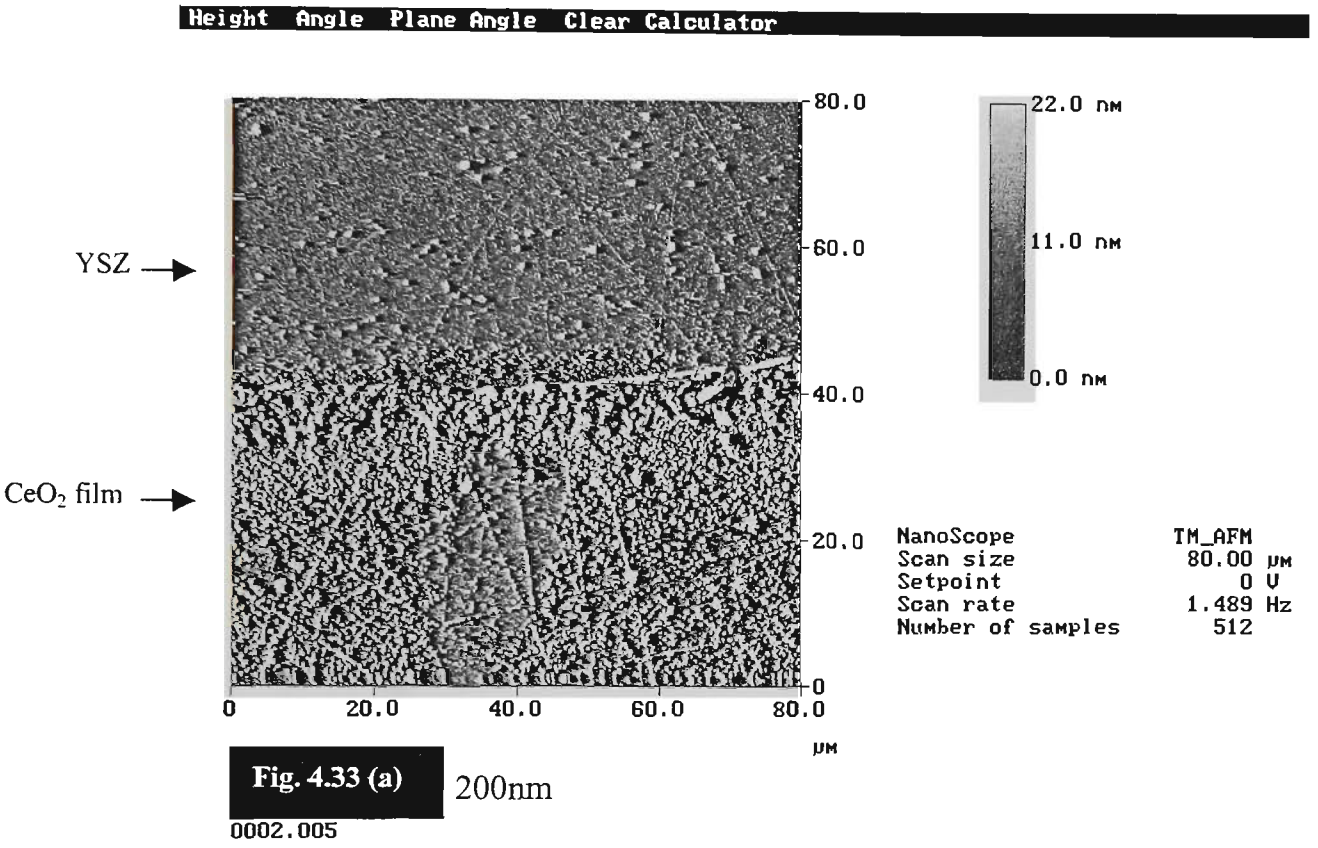

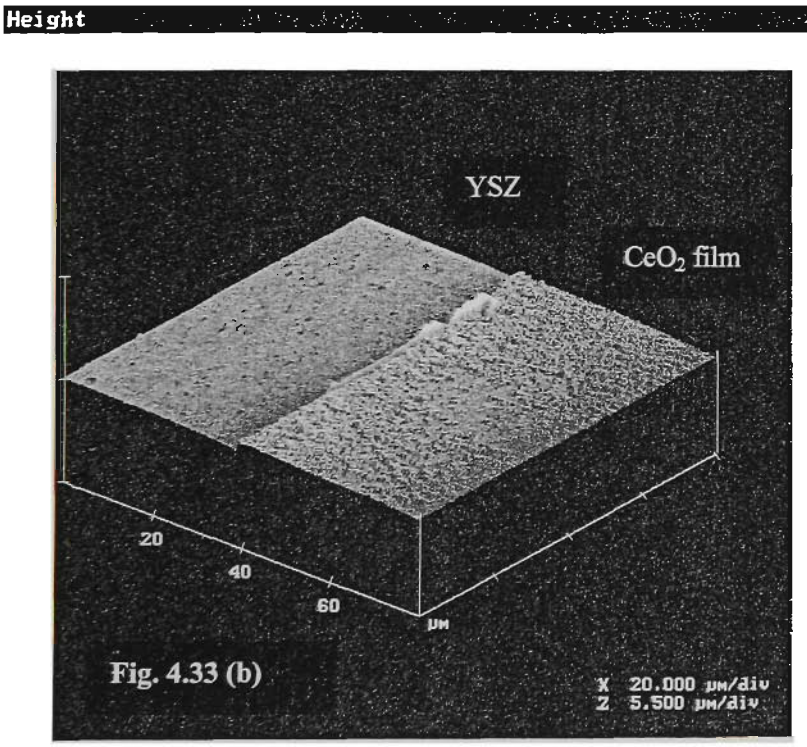

Figure 4.33 AFM image of a CeO_2 film step on an YSZ substrate. It is obvious that there is a relationship between the linear outgrowths and the polishing scratches on the YSZ substrate.

Fig. 4.34 is a schematic diagram that illustrates the correlation between the linear outgrowths and the polishing scratches. The incredible thing is why such shallow polishing scratches (about 2 - 3nm depth) can affect the surface morphology of CeO_2 films with a thickness about 2 orders of magnitude larger than the depth of the scratches. There are two possible reasons for this correlation, one is the geometrical shape of the scratch, another is the stress stored at the scratch due to the mechanical polishing.

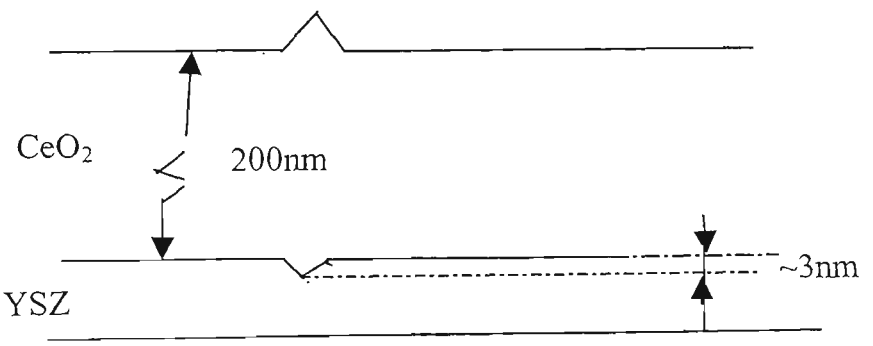

Figure 4.34 Schematic diagram of the correlation between linear outgrowths and polishing scratches

YSZ substrates were annealed at high temperature in air in order to relieve the stress stored at the scratches. The annealing temperatures were selected to be 900, 1100, 1300, and 1500°C. The time at the annealing temperature was 6 h. CeO_2 films were then deposied under the same deposition conditions used previously on non-annealed YSZ. For annealing at 900°C, there is no obvious effect on the surface morphology. For annealing at 1100 and 1300°C, annealing has a significant effect on reducing the linear outgrowths on the surface of CeO_2 films. **Fig. 4.35** shows an AFM image of a 100nm

CeO_2 film on an YSZ substrate annealed at 1100°C. Note that the density of linear outgrowths is very low. Annealing at 1500°C almost eliminates linear outgrowths. It can thus be confirmed that the correlation between linear outgrowths and polishing scratches is due to stress which is caused by mechanical polishing and is stored by the scratch. This fact suggests that it is better to anneal YSZ substrates at high temperature before the film deposition.

So far as linear grooves as concerned, there is still no proof of a correlation with the substrate. They are perhaps due to the growth process of CeO_2 films. The density of linear grooves is much lower than the density of linear outgrowths. Although the linear grooves are very shallow (1~3nm), there is certainly a correlation between linear grooves and singular outgrowths.

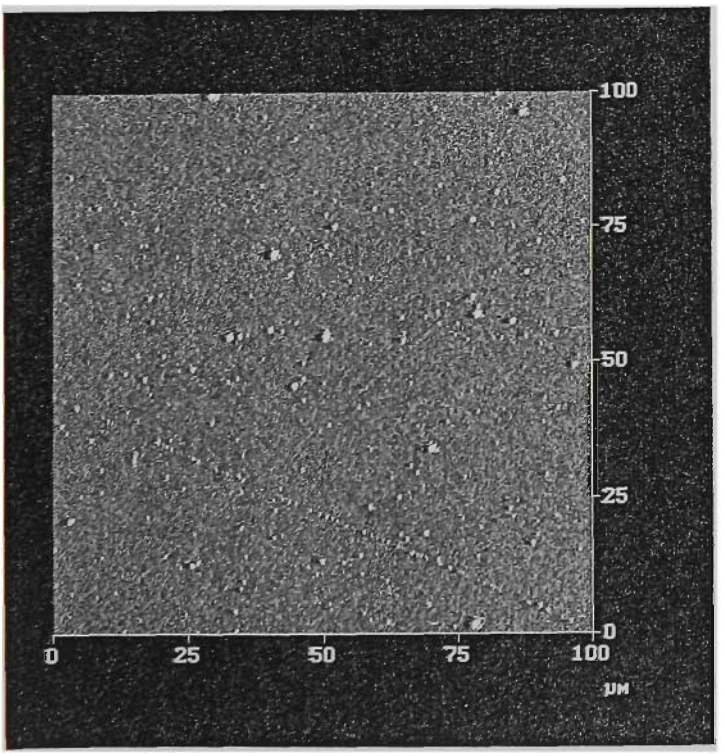

Figure 4.35 AFM image of a CeO_2 film with 100nm thickness on an YSZ substrate annealed at 1100°C for 6hr. The large white particles are droplets due to laser ablation.

C. The correlation between singular outgrowths and the linear grooves on the surface of CeO_2 films

Because singular outgrowths are much higher than linear grooves and linear outgrowths, they give a much greater contribution to the roughness of the surface. In order to get a smooth surface, singular outgrowths should be as few as possible. Singular outgrowths are not randomly distributed on the surface. From **Fig. 4.31**, it can be seen that they are often correlated with linear grooves. **Fig. 4.36** gives a clear AFM image of a CeO_2 film which shows that the large singular outgrowths are located along the grooves, so it can be inferred that the grooves are an important source of outgrowths. One of the explanations about this is that the stress stored at the grooves may play a role in the growth of large outgrowths, by causing the deposition species to coalesce around it. From this point of view, the linear grooves store more stress than the linear outgrowths, which makes the linear grooves more easily become a source of large outgrowths.

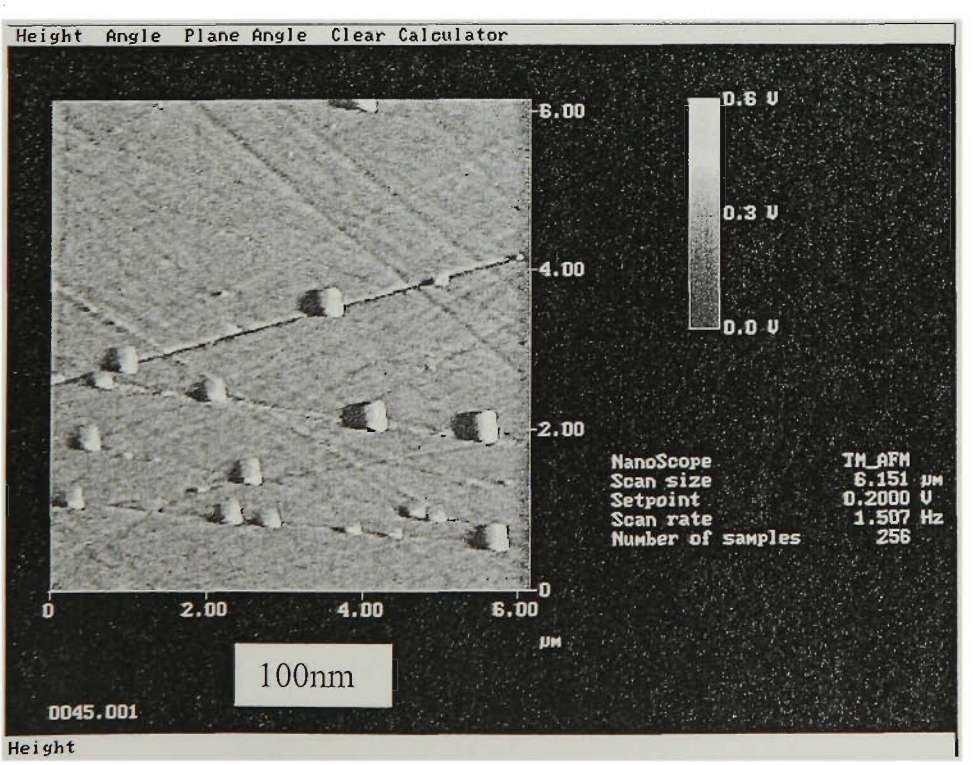

Figure 4.36 A clear AFM image of a CeO_2 film that shows that large singular outgrowths are located along the grooves.

4.4. Summary

There is a significant difference between the epitaxial growth of CeO_2 films by using an O_2 or an Ar+10%H_2 atmosphere on YSZ substrates. Pure c-axis CeO_2 films were grown over a substrate temperature range of 775 - 805°C using an O_2 atmosphere, with the smallest surface roughness occurring at 790°C. A pure c-axis orientation was obtained for substrate temperatures between 350°C and 775°C using an Ar + 10% H_2 atmosphere. The c-axis orientation of CeO_2 films deposited using O_2 is better than that achieved using Ar + 10% H_2, as confirmed by the FWHM of the ω-scan. The morphologies of the CeO_2 films produced in O_2 and Ar + 10% H_2 atmospheres and examined by AFM are remarkably different in terms of outgrowth formation. For the CeO_2 films deposited using O_2, there are many large outgrowths formed as compared to the films deposited under an Ar + 10% H_2 atmosphere. Consequently, the roughness of the former is larger than the roughness of the latter, and it can be deduced that the mobility of the species during deposition of CeO_2 films is smaller using Ar + 10% H_2 than using O_2. The epitaxial growth of a metallic oxide film using an atmosphere including H_2 is quite a new technique, having some advantages for CeO_2 films such as low temperature growth and a smooth surface. It is may be worthwhile to transfer this method to deposit CeO_2 films on other single crystal substrates, such as Si.

The effects of the deposition rate and the film thickness on the surface morphology of CeO_2 films were investigated. For the CeO_2 films deposited in an O_2 atmosphere there is a critical thickness of about 200nm beyond which the surface roughness progressively deteriorates.

The CeO_2 film on YSZ can have a spherical background morphology at 3 Hz, and maintain it until 100nm thickness, but the background morphology will completely change to rectangular by 900nm thickness.

Through studying the change of grain shapes of CeO_2 films with increasing film thickness, it was found that the degree of c-axis orientation is related to the morphology of the CeO_2 grains; the more spherical the shape of the grains is, the better the c-axis orientation and the smoothness of the CeO_2 film surface are. This correlation appears to be an intrinsic feature of CeO_2 films, independent of the type of substrate or the deposition method. For the epitaxial growth of a CeO_2 film, not only the lattice mismatch between the film and substrate, but also the angle between the axes of substrate has an important influence on the film.

By studying the orientation and the surface morphology of CeO_2 films, the relationship between epitaxial quality and growth mode can be analysed. The optimum epitaxial growth of CeO_2 is layer-by-layer growth from the beginning to the end, and the lower quality epitaxial growth is layer-by-layer and then island growth. The growth mode of imperfectly c-axis oriented film is typical island growth. As the islands grow larger and become large outgrowths, the outgrowths prefer to connect to each other to form a network on the surface. For a low quality CeO_2 film which was far from epitaxial, the growth of the film was characterized by the typical terrace-ledge-kink growth mode of cubic crystal.

Some linear outgrowths on the surface of CeO_2 films are correlated with the polishing scratches on the YSZ substrates, although the thickness of the CeO_2 film is much larger than the depth of the scratches. It is believed that the stress stored at the polishing scratch is the reason for this correlation. The annealing of YSZ substrates at high temperature (>1100°C) can significant reduce the density of linear outgrowths. The linear grooves more easily become the source of large outgrowths.

Chapter 4 references

1. K. D. Develos, N. Kusunoki, and S. Ohshima, Japanese Journal of Applied Physics Part 1-Regular Papers Short Notes & Review Papers. 37(1998) 6161
2. K. Develos, H. Yamasaki, Y. Nakagawa, S. Ohshima, and M. Mukaida, Physica C 357 (2001) 1353
3. K. D. Develos, M. Kusunoki, and S. Ohshima, Physica C. 320 (1999) 21.
4. K. D. Develos, N. Kusunoki, and S. Ohshima, Superconductor Science & Technology. 12 (1999) 887.
5. K. D. Develos, H. Yamasaki, A. Sawa, and Y. Nakagawa, Physica C 361 (2001)121
6. S. Ohshima, K. D. Develos, K. Ehata, M. I. Ali, and M. Kusunoki, Physica C 335 (2000) 207
7. K. D. Develos, M. Mukaida, M. Kusunoki, and S. Ohshima, Japanese Journal of Applied Physics Part 1-Regular Papers Short Notes & Review Papers. 39(2000) 1116
8. A. Wang, J. A. Belot, T. J. Marks, P. R. Markworth, R. P. H. Chang, M. P. Chudzik, C. R. Kannewurf, Physica C 320(1999) 154.

9. B. F. Cole, G. C. Liang, N. Newman, K. Char ,and G. Zaharchuk , and J. S. Martens, Appl. Phys. Lett. 61 (1992) 1727.

10. X. D. Wu, R. C. Dye, R. E. Muenchausen, S. R. Foltyn, M. Maley, A. D. Rollett, A. R. Garcia, and N. S. Nogar, Appl. Phys. Lett. 58 (1991) 2165.

11. M. Lorenz, H. Hochmuth, D. Natusch, H. Borner, G. Lippold, K. Kreher, and W. Schmitz, Appl. Phys. Lett. 68 (1996) 3332.

12. D. Q. Shi, B. Yang, X. Wang, Z. Peng, X. Wang, J. Hao, L. Wang, and Y. Wen, Rare Metals 14 (1995) 314

13. D. Q. Shi, B. C. Yang, X. P. Wang, Z. S. Peng, X. H. Wang, J. M. Hao, L. Wang, and Y. L. Wen, Rare Metals,14 (1995) 67.

14. D. P.Norton, A. Goyal, J. D.Budai, D. K.Christen, D.M.Kroeger, E. D. Specht, Q. He, B. Saffian, M. Paranthaman, C. E. Klabunde, D. F. Lee, B. C. Sales, and Fred A. List, Science, Vol. 274(1996) 755-757

15. J. Yang, D. Q. Shi, X. Wang, A. Liu, and G. Yuan , Physica C 337 (2000) 67

16. D. Q. Shi, M. Ionescu, J. McKinnon, and S. X. Dou, Physica C 356 (2001) 304.

17. D. P. Norton, A. Goyal, J. D. Budai, D. K. Christen, D. M. Kroeger, E. D. Specht, Q. He, B. Saffian, M. Paranthaman , C. E. Klabunde , D. F. Lee, B. C. Sales, and F. A. List, Science, 274 (1996) 755.

18. X. Xiong, and D. Winkler, Physica C 336 (2000) 70.

19. C. V. Thompson, J. Floro, Henry J. Smith, J. Appl. Phys. 67 (1990) 4099-4104.

20. J. A. Venables, Introduction to Surface and Thin Film Processes, Cambridge University Press, 2000, p 145.

21. L. Eckertova, Physics of Thin Film, Published by Plenum Press, 1986 p96

22. J. A. Venables, Introduction to Surface and Thin Film Processes, Cambridge University Press, 2000, p5

23. Gerber C, Anselmetti D, Bednorz J G, Mannhart J and Schlom D G, Nature 350(1991) 279.

Chapter 5. Fabrication of epitaxial CeO_2 films on cubic texture nickel substrates

5.1. Introduction

Rolling assisted biaxially textured substrates (RABiTS) method is a main approach to fabricate YBCO coated conductors[1-7]. In order to grow high quality epitaxial superconducting films on the cubic textured Ni substrates by RABiTS method, it is necessary to deposit epitaxial buffer layers on the metal surface to improve the crystallinity of the subsequent YBCO film and to achieve chemical reaction control between the metal substrate and the YBCO film[8-11].

Typically, the most desirable buffer layers for YBCO film growth are oxides. However, Fabricating oxide buffer layers on Ni for epitaxial deposition of YBCO superconducting films is difficult because of the ease of surface oxide formation on Ni under the oxidizing atmospheres required for oxide film growth. Usually the orientation of NiO films is not epitaxial and (111) textured NiO is a preference, which is unsuitable for fabricating high-J_c YBCO films.

One approach has been found by ORNL to solve the problem of unfavorable NiO. An epitaxial CeO_2 buffer layer was directly deposited on the Ni by introducing H_2 gas during the initial film growth. Deposition was performed under a partial pressure of hydrogen such that NiO is unstable while CeO_2 is stable. In the ORNL experiment , Ar + 4% H_2 was used to deposit CeO_2 films [12]. Another effect of using Ar + 4% H_2 is that the epitaxial temperature is about 400°C, much lower than when using oxygen,

which also reduced the oxidation of Ni. CeO_2 films on Ni have cracks because of the thermal expansion mismatch between Ni substrate and CeO_2 film. After the CeO_2 film was deposited, an YSZ layer was deposited on the CeO_2 film by PLD to alleviate cracking of the CeO_2 film [12].

In the RABiTS method, the quality of the texture, surface roughness and integrity of CeO_2 films are crucial factors. In this chapter, some work has been done on fundamental studies of CeO_2 films as buffer layers on cubic Ni. We first studied the quality of the texture, crystallization, and surface roughness of the Ni substrates, then investigated the relationship between the texture of CeO_2 films and the deposition conditions. The optimum deposition conditions have been found through serial experiments. Finally , the cracks in CeO_2 films were investigated, and some efforts have been made to reduce the cracks in CeO_2 films.

5.2. Experiments

Deposition was achieved by the same deposition system used to deposite CeO_2 films on YSZ substrates. A Compex 301 KrF excimer laser was used with a wavelength of 248nm and a 25 nanosecond pulse duration, and the output energy of the laser is between 350mJ and 1000mJ. The pulse, which is rectangular and about 30cm×8cm at the laser window, is focused in one dimension through a cylindrical lens that has a focal length of 80cm. The beam of laser light is passed through the focusing lens and a sapphire window and then into the chamber. This arrangement results in a rectangular spot of approximately 1.0cm × 0.2 cm on the target.

Before the deposition, the chamber was evacuated to about 1×10^{-6} Torr by a turbo molecular pump, and then the sample holder was heater. For studying the optimum deposition conditions, a wide range of deposition pressure was used, Generally, for deposition pressures lower than 50mTorr, the turbo pump was used during the deposition with the pumping speed adjusted by the gate valve. For the deposition pressures higher than 50mTorr, only a mechanical pump was used during the deposition. Ar + 10% H_2 forming gas was used, and the deposition pressure was maintained by adjusting a pin valve.

The Ni substrates were cleaned with detergents and organic solvents using an ultrasonic cleaner. A Ni sample was then attached to the substrate holder with the silver paste. Before the formal deposition, the target was ablated for about two minutes to clean the surface. The particulars of the deposition system were similar to that for CeO_2 films on single crystal YSZ substrates using Ar + 10% H_2 : substrate parallel with target and on the axis of target; target-substrate distance 40~70mm; target rotation 10rpm; background pressure $1x10^{-6}$ Torr. The deposition conditions were: laser repetition rate 1~10Hz; and energy density on the target 1.8~3.0 Jcm^{-2} (400~650mJ/pulse). The deposition pressure was 0.1~ 200mTorr Ar + 10% H_2 forming gas.

Some important aspects of the PLD deposition in our works should be noted:

1. The cleanliness of the sapphire window has an significant influence on the energy of laser impacting on the target. It is necessary to clean the window every few depositions.

2. A 28mm diameter stoichiometric CeO_2 ceramic target was used. **Fig. 5.1** gives an SEM image of the freshly polished CeO_2 target, and it can be seen that the ceramic grains are small (~1-2μm). During deposition, the laser ablation causes some target melting. In the ablation region, the ceramic grains are large (~ 4μm) and non-uniform (shown in **Fig. 5.2**). In order to prevent laser ablation from causing non-stoichiometry of the surface of the CeO_2, the target was polished after every few depositions.

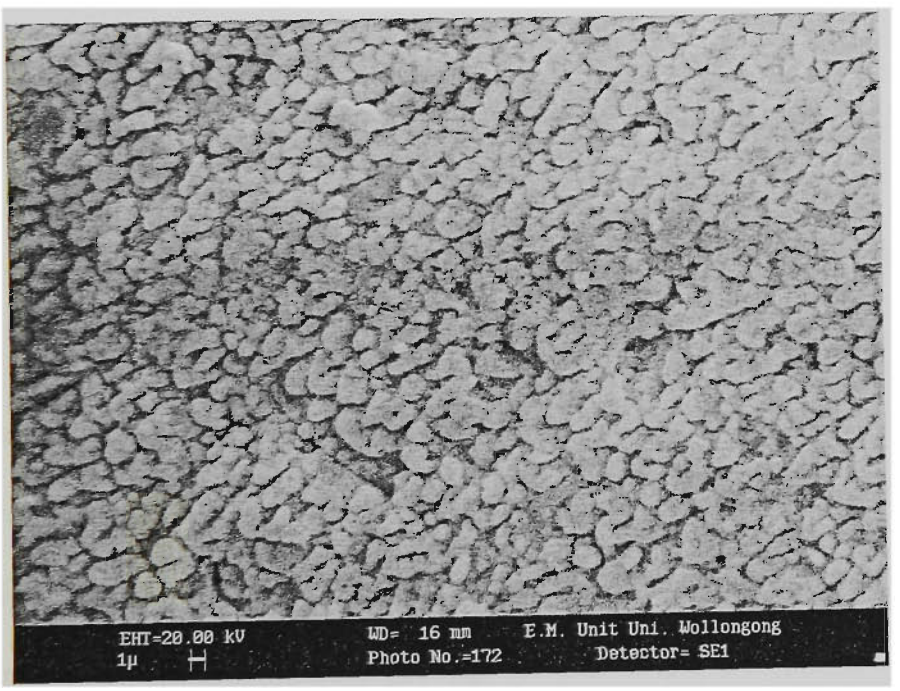

Figure 5.1. SEM image of the surface of the freshly polished CeO_2 target.

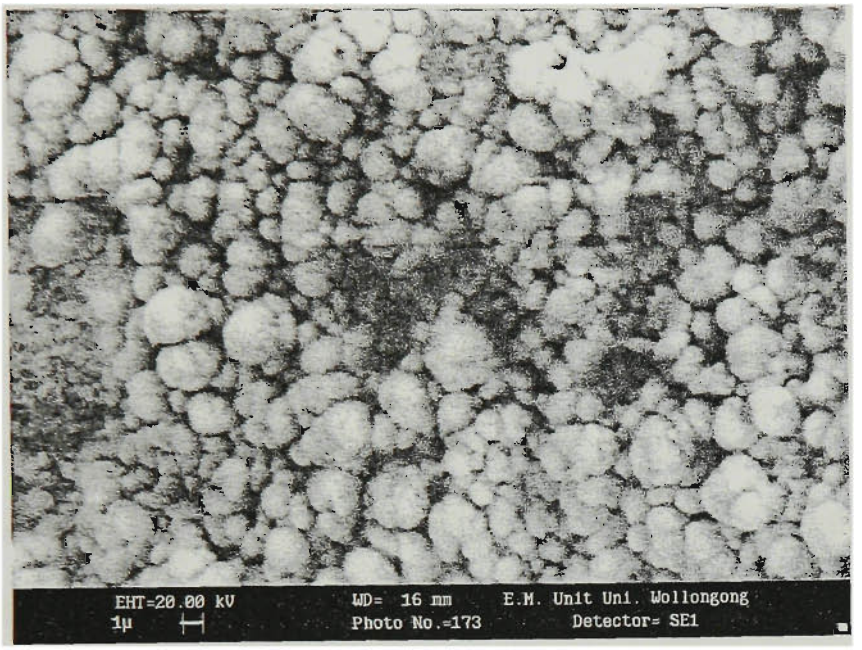

Figure 5.2. SEM image of the surface of the CeO_2 target after laser ablation.

3. The substrate holder is heated by electrical resistance which is made of NiCr alloy and can work at high oxygen pressures. A thermocouple is attached to the inside of the substrate holder. Actually, the thermocouple measures the temperature of the substrate holder, not the temperature of the surface of the substrate which is the critical condition for the deposition. The thicknesses of single crystal YSZ substrate (0.5mm) and cubic Ni substrate (0.15mm) are different, as well as their heat conduction. While the thermocouple indicates the same temperature for YSZ and Ni substrates, the temperatures on the surface of

these substrates is actually different. This fact is very important for the deposition process.

4. The nickel samples of $5\times13mm^2$ were cut by a chisel instead of scissors which can produce a shear texture and damage the cubic texture.

XRD θ-2θ scans, ω-scans, ϕ-scans, and pole figures were used to investigate the texture and orientation of Ni substrates and CeO_2 films. SEM was used to examine the surfaces of Ni substrates and CeO_2 films. Ni substrates serving as SEM samples were etched using the diluted HNO_3. Because CeO_2 film is an insulator, Au thin film was firstly deposited on it by DC. Sputtering for the SEM examination.

5.3. Results and discussion

5.3.1. Examination of Ni substrates

Many face-centered cubic metals, such as copper, aluminum and nickel, can exhibit an almost perfect cubic texture after rolling to a large reduction of thickness and subsequent annealing. The cubic textured Ni tapes were fabricated by our collaborators. High purity Ni tapes with a thickness of about 0.15mm and a width of 13mm were formed by progressive deformation rolling. The total deformation is more than 90%. The rolling texture was investigated by means of XRD pole figures such as those shown in **Fig. 5.3**, which illustrate a typical rolling texture. The $\{123\}\langle \bar{4}, \bar{1},2\rangle$, $\{110\}\langle \bar{1},1,2\rangle$, and $\{112\}\langle \bar{1}, \bar{1},1\rangle$ orientations are very strong. [13]. A systemic

study of rolling texture can be achieved using orientation distribution functions (ODFs) in Euler space [14].

The rolling of the Ni tapes was followed by a recrystallization anneal in a high vacuum with tantalum getter, or in a 1 atm Ar-H_2 atmosphere at 850-900°C for 15-30 minutes. Recrystallization is a process of nucleation and growth. The size and shape of the grains after recrystallization are different from the as- rolled condition. The recrystallization texture was investigated by means of XRD pole figures such as those shown in **Fig. 5.4**. It can be seen the deformation texture was almost entirely changed to the cubic texture. In **Fig. 5.3**, the deformation texture of the Ni is not cubic, so the recrystallization texture is completely different from the deformation texture.

Typical sample has XRD ω-scan and ϕ-scan, shown in **Fig.5.5** and **Fig.5.6,** with a FWHM of 6° and 8° respectively. Having Ni substrates with a sharp and uniform texture is very important to the fabrication of long coated tapes. The textures of many Ni substrates cut to a 1 cm length were examined. About 80% of the samples have good cubic texture (as shown in **Fig. 5.4**). However, about 20% of the samples do not. **Fig. 5.7** shows pole figures of an example of these poor samples. The value of the FWHM of the ϕ-scan is about 10°. The cubic texture of Ni was found to be stable up to the YBCO deposition temperature of 800°.

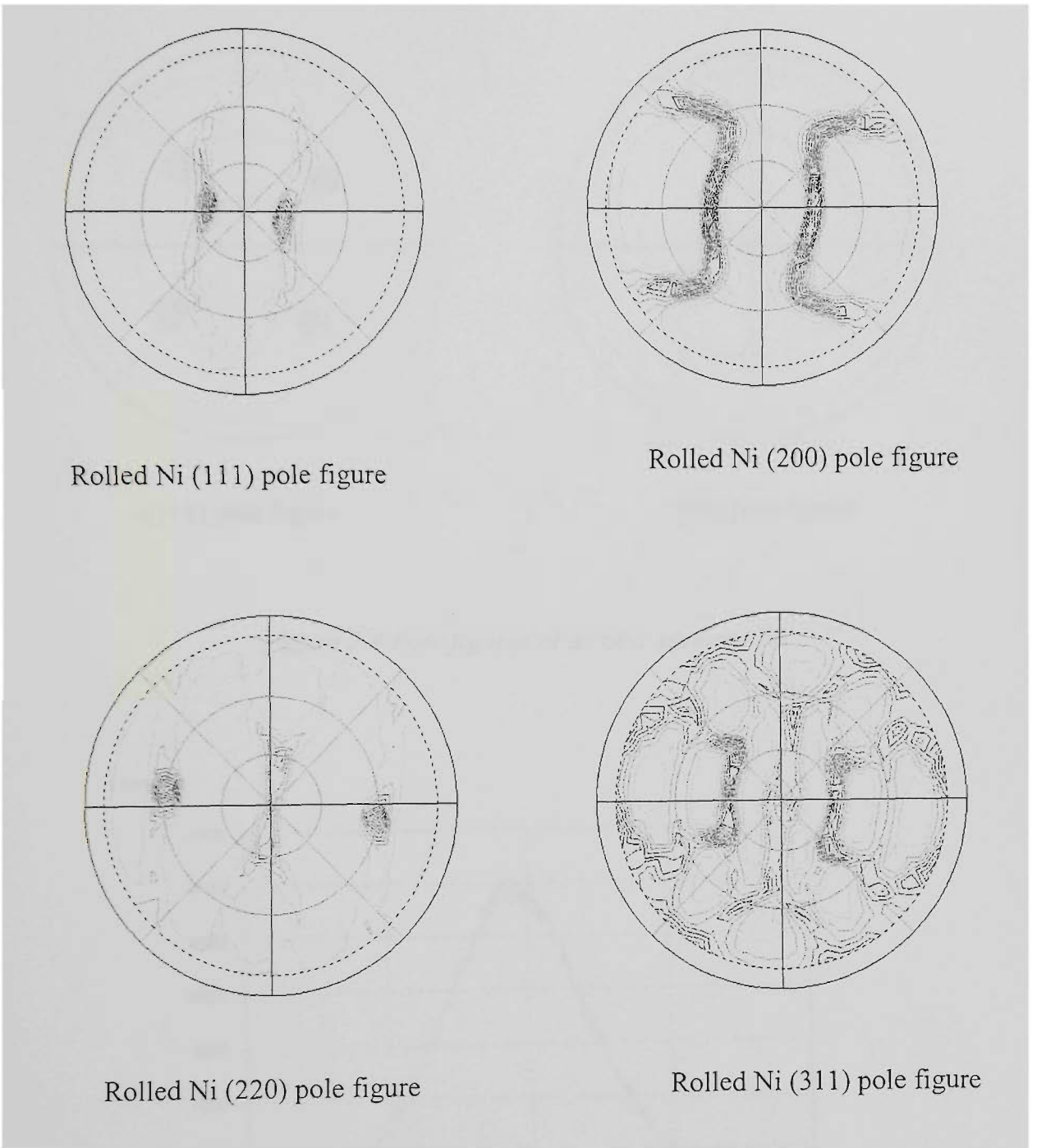

Figure 5.3. XRD pole figures of an as-rolled Ni tapes.

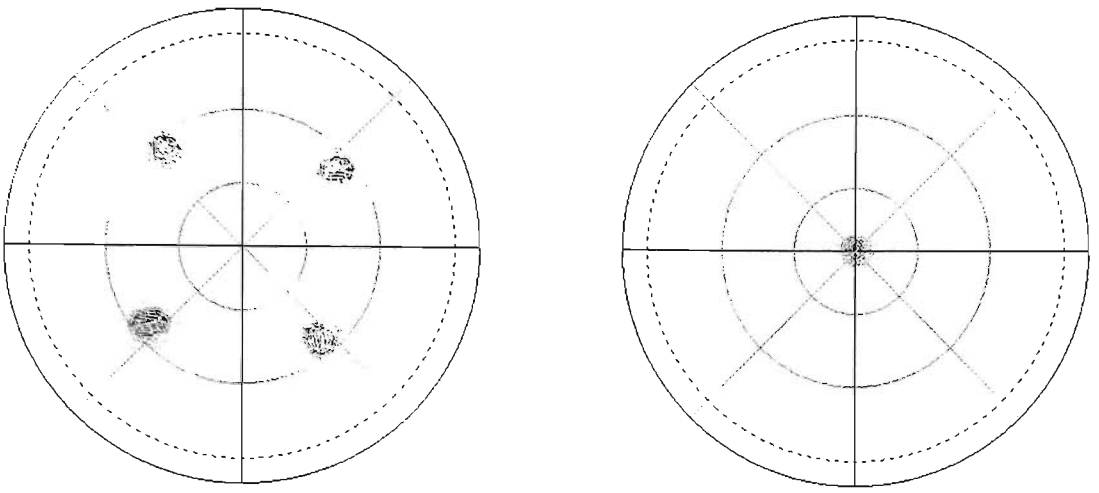

(111) pole figure (200) pole figure

Figure 5.4 Pole figures of a cubic textured Ni.

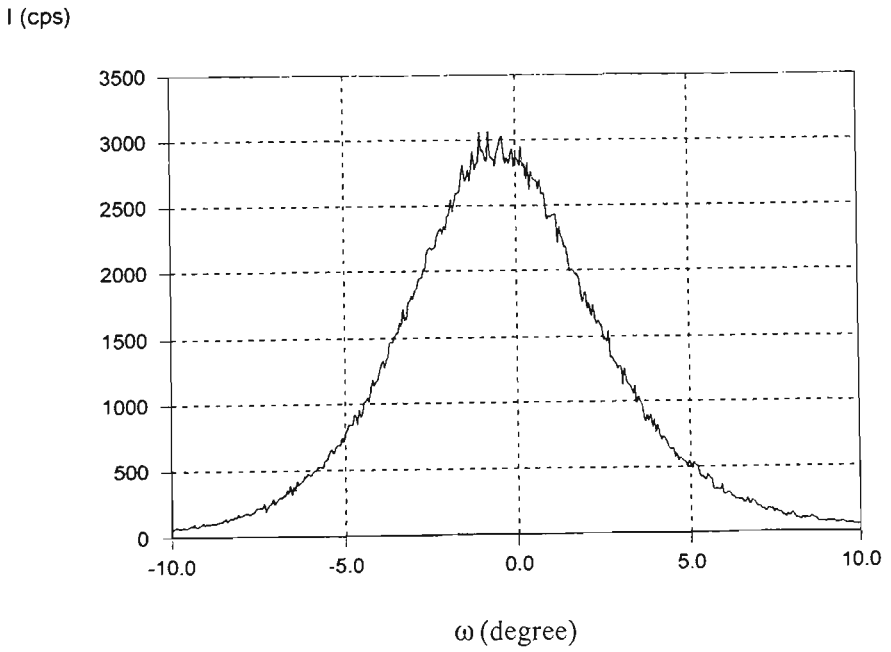

Figure 5.5. ω-scan of a cubic textured Ni substrate, the value of the FWHM is about 6°.

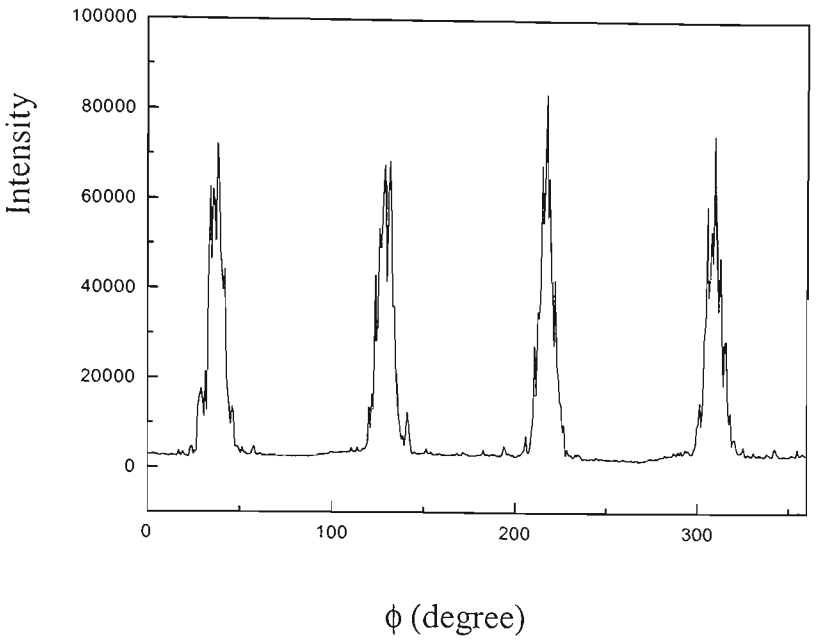

Figure 5.6. ϕ-scan of a cubic textured Ni substrate, the value of FWHM is about 8°.

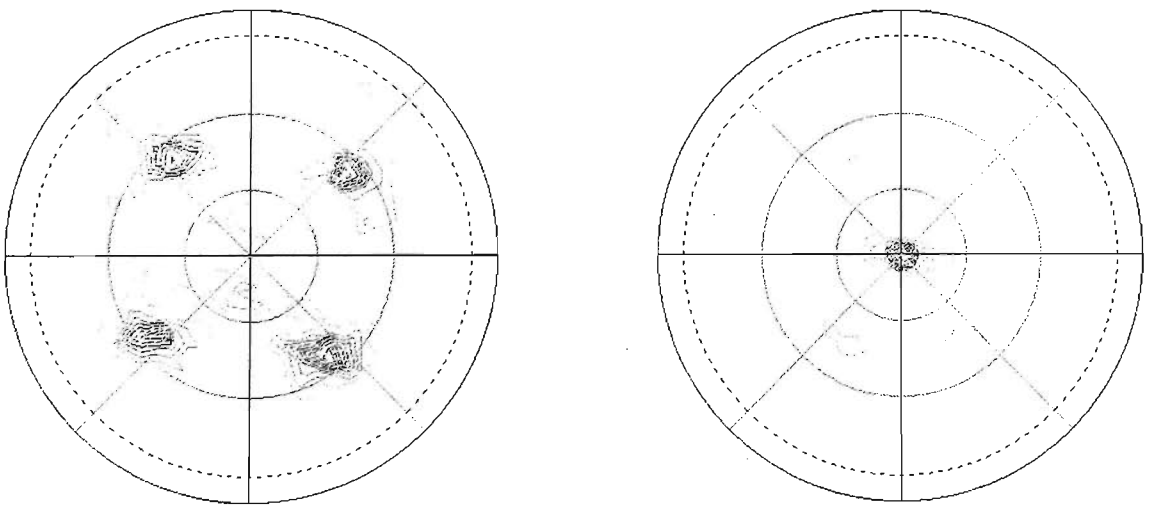

Figure 5.7. Pole figures of a low-quality cubic textured Ni substrate.

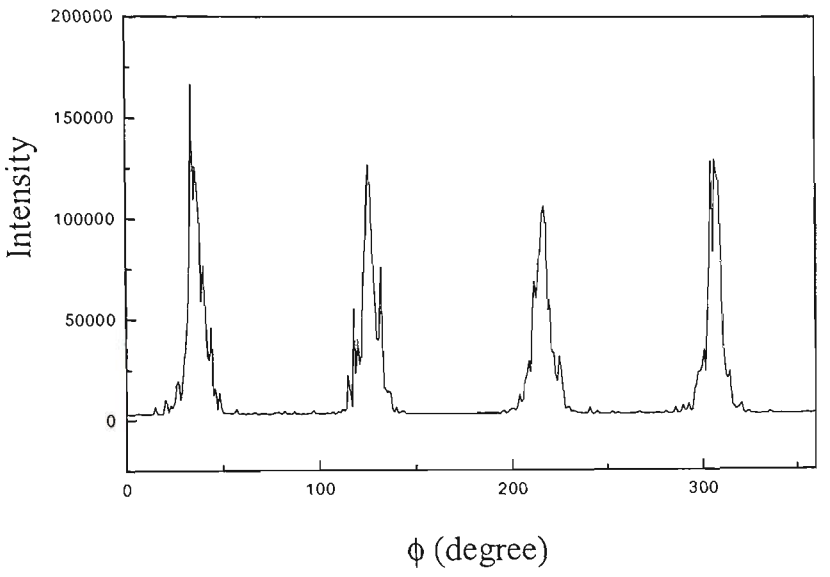

Figure 5.8. ϕ-scan of a low-quality cubic textured Ni substrat; the FWHM is10°.

Fig. 5.9 and **Fig. 5.10** show optical and SEM images of the grains of a cubic textured Ni substrate. It can be estimated that the sizes of the recrystallization grains are about 20~30μm diameter, and there are not very large grains, which means that the recrystallization is mainly the primary recrystallization. The advantage of primary recrystallization is that the surface roughness is not much worsen after the recrystallization. The surface condition of a substrate can greatly affect the epitaxy and integrity of buffer layers and hence the J_c of the superconducting film. Mechanical polishing can seriously damage the cubic texture. Although chemical or electro-polishing do not degrade the cubic texture, they are not suitable for scaled-up long tapes. An AFM scans in a 40×40 μm region indicate an Rms roughness of ~120nm, far from the best roughness reported in the literatures. From **Fig. 5.9**, it can be seen there are many scratches caused by the rolling process.

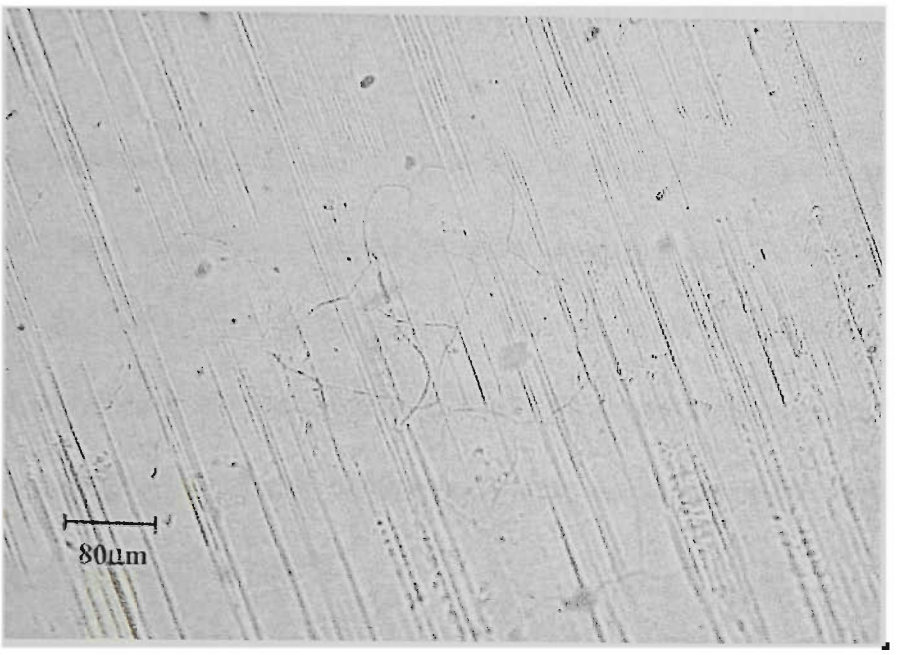

Figure 5.9. Optical microscope image of a cubic textured Ni substrate.

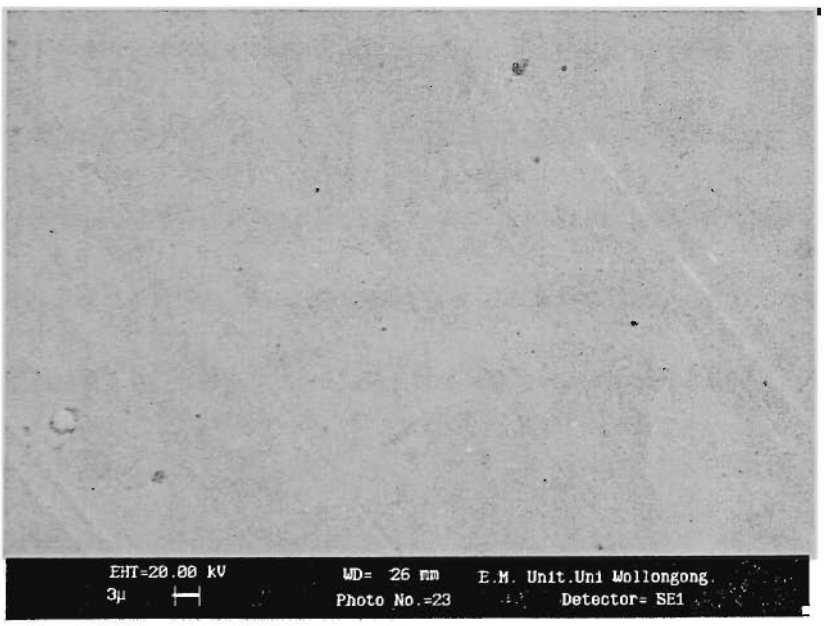

Figure 5.10. SEM image of a cubic textured Ni substrate.

5.3.2. Relationship between the deposition conditions and the texture of CeO_2 films

The deposition temperature, deposition rate adjusted by the pulse laser repetition rate, deposition pressure, and the distance between the target and the substrate are important parameters for CeO_2 film deposition. In order to study the relationship between the deposition conditions and the texture of CeO_2 film, and moreover, to find the optimum deposition conditions, a series experiments were conducted with changing one of the parameters and fixing the others.

The deposition temperature is the most important parameter for epitaxial growth. **Fig. 5.11** shows the XRD patterns of CeO_2 films prepared by PLD at different temperatures and at 3Hz and 530mJ laser energy. The films show that the growth direction changes from CeO_2 (111) to CeO_2 (200) with increasing deposition temperature from 370°C. The ratio of the intensity of the (200) peak and the (111) peak reaches a maximum at a deposition temperature of 395°C, then declines as the temperature continues to increase (shown in **Fig. 5.12**). Compared to the large epitaxial temperature range for CeO_2 film on YSZ using Ar + 10%H_2, the temperature range for CeO_2 film on Ni is almost a point. The lattice constant of Ni is 3.52Å, and the lattice constant of CeO_2 is 5.41Å. The CeO_2 layer has a 45° in-plane rotation with respect to the lattice of Ni, and the lattice mismatch is about 8.8%, larger than the lattice mismatch of 5% between CeO_2 and YSZ. Moreover, the orientation of the Ni is not as perfect as in the single crystal, So the epitaxial temperature range of CeO_2 on Ni is much more narrow than on YSZ. The following experiments were carried out at the optimum deposition temperature of 395°C.

A pulsed laser at 1, 3, or 5 Hz was used for the depositions. The result is that the film under 3Hz deposition has the best c-axis orientation (shown in **Fig. 5.13**), which means that at this deposition rate the deposited species have enough mobility to find a perfect position.

Fig. 5.14 shows the ratio of the XRD θ-2θ scan intensity of the (200) peak and the (111) peak with increasing Ar + 10% H_2 pressure. CeO_2 film deposited at 100mTorr has the best c-axis orientation. A similar analysis was employed with respect to changing laser energy. A laser energy of 500 mJ is the best energy for the epitaxial growth of CeO_2 films (see **Fig. 5.15**)

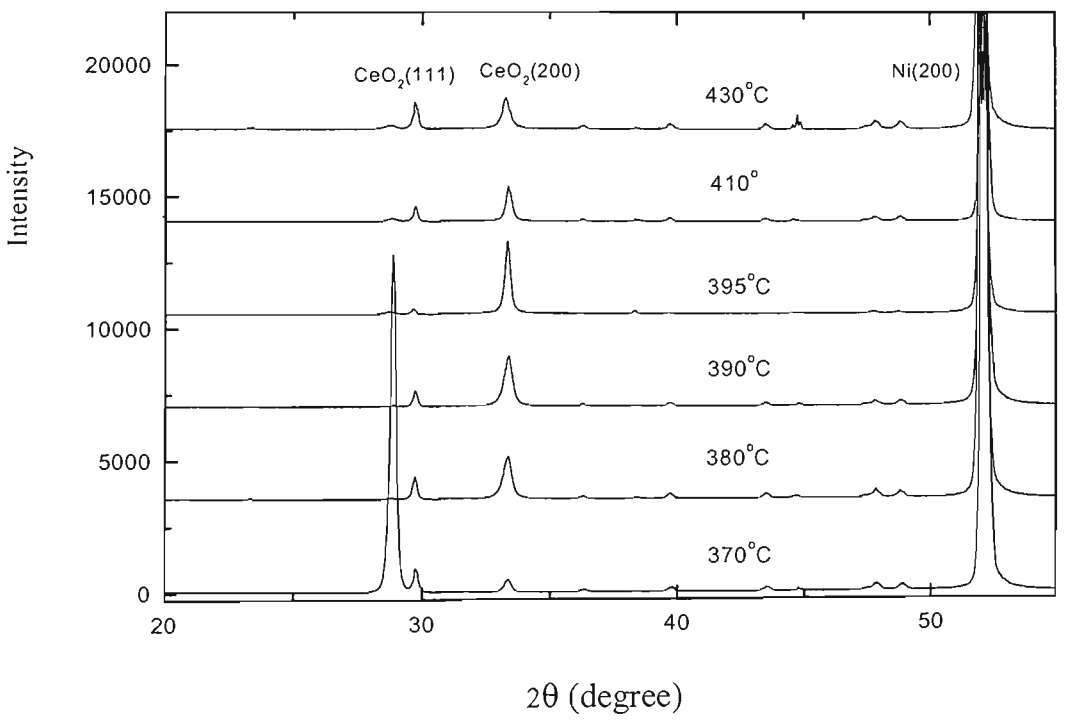

Figure 5. 11. XRD θ-2θ scan patterns of CeO_2 films grown on cubic textured Ni at different temperatures.

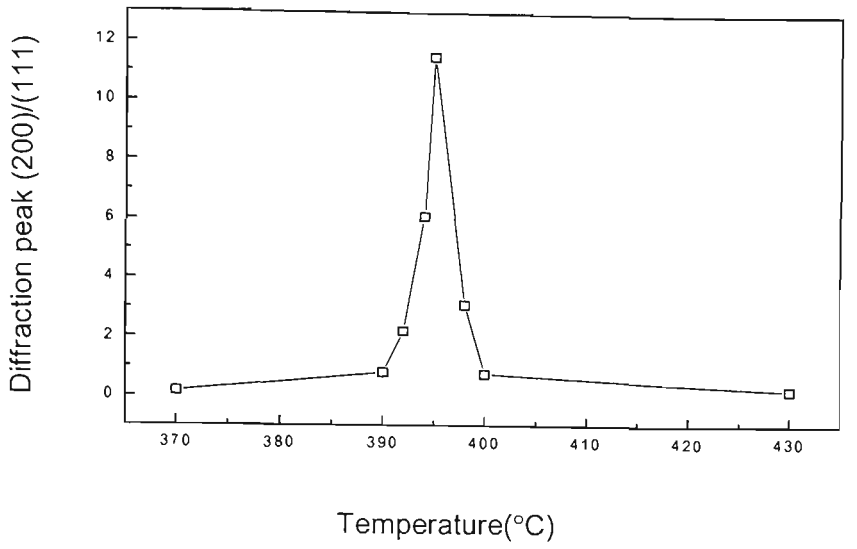

Figure 5.12. Dependence on deposition temperature of the ratio of the intensities of the (200) peak and the (111) peak, for CeO_2 films deposited on Ni substrate.

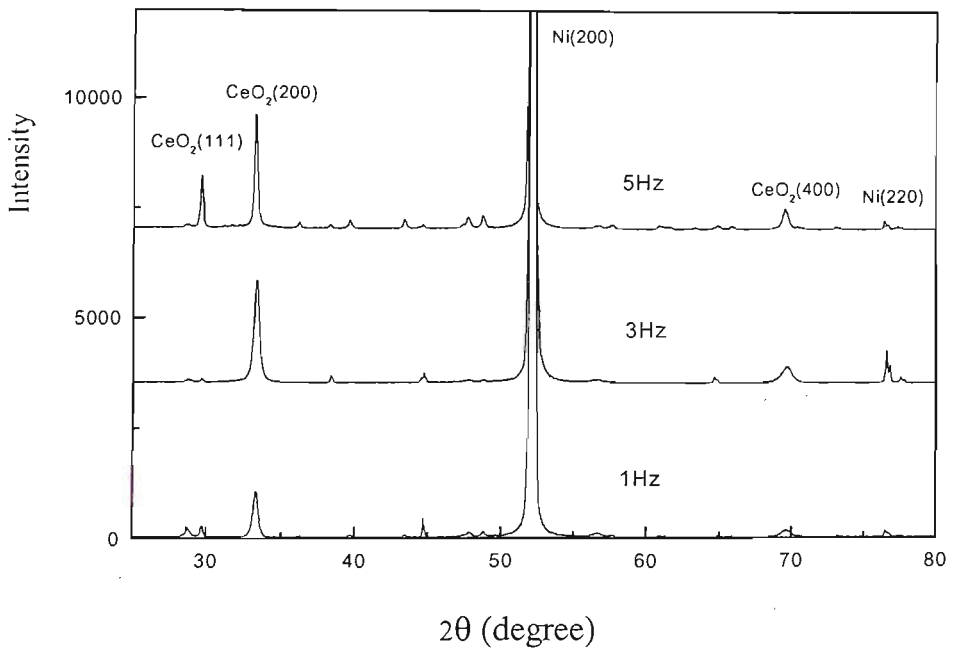

Figure 5. 13. XRD θ-2θ scan patterns of CeO_2 films grown on cubic textured Ni using different laser repetition rates.

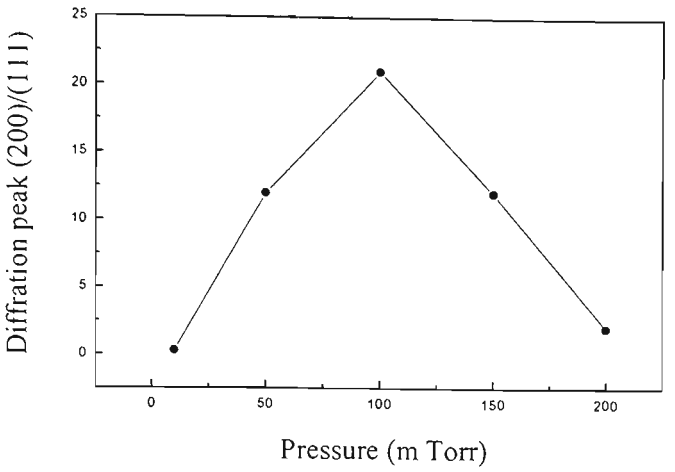

Figure 5.14. Dependence on deposition pressure of the ratio of the intensities of the (200) peak and the (111) peak, for CeO_2 films deposited on Ni substrate.

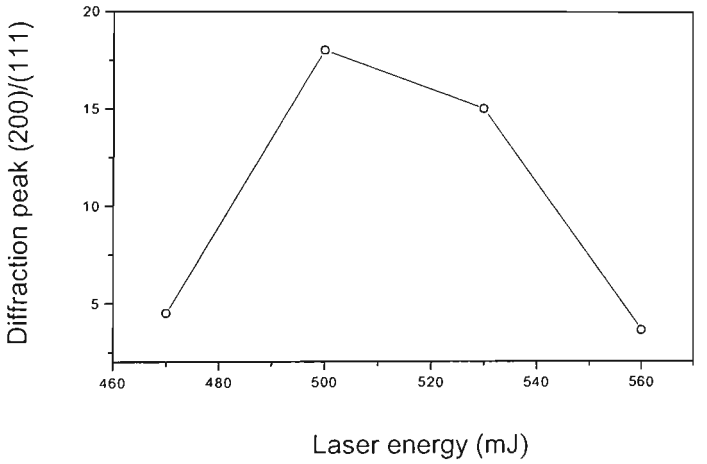

Figure 5.15. Dependence on laser energy of the ratio of the intensities of the (200) peak and the (111) peak, for CeO_2 films deposited on Ni substrate.

The distance between the target and the substrate is another important parameter, and it depends on the length of the plasma plume. However, the size of plasma plume also depends on the pressure of the deposition chamber: the higher the pressure is, the shorter and wider the plume is; and the lower the pressure is, the longer and more narrow the plume is. Fig. **5.16** gives a schematic diagram of the relationship between the plume and the pressure. No matter what the size of the plume is, the optimum distance between the substrate and target is slightly beyond the plume (~5mm). At this distance, the deposited species are stoichiometric, and the energy of the deposited species is suitable for epitaxial growth.

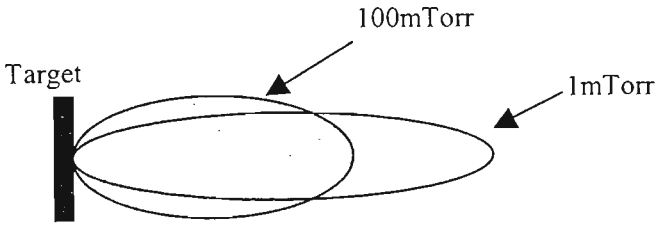

Figure 5.16. Schematic diagram of the relationship between the plume and the deposition pressure.

The optimum deposition is: deposition temperature 395°C; pulsed laser of 3Hz and 500mJ; Ar + 10% H_2 pressure of 100mTorr; and target-substrate distance of 5 cm. **Fig.5.7** shows the XRD θ-2θ scan of the sample. The degree of c-axis orientation, as given by Ic=I(200)/(I(111)+I(200)), is 95.8%. **Fig. 5.18** shows an XRD ω-scan of the (200) peak of optimum CeO_2 film, the value of FWHM is 4.9°. Compared to the FWHM value of Ni (6°), the c-axis orientation of the CeO_2 film is improved.

The ϕ-scan pattern (a) in **Fig. 5.19** shows an XRD ϕ-scan of the CeO_2 (111) peak, and the value of the FWHM is 12°. Comparing the ϕ-scan of the Ni (111) peak for the same CeO_2/Ni sample, shown in ϕ-scan pattern (b), the peaks of the ϕ-scan of the CeO_2 film are shifted to a 45° angle to the ϕ-scan peaks of Ni. This proves that the CeO_2 principal crystallographic axes are rotated 45° relative to the in-plane Ni (100) axes. The epitaxial orientation in this case is <110> CeO_2//<100>Ni. This growth is in agreement with near-coincidence site lattice match modes (see the schematic diagram in **Fig. 5.20**) [15].

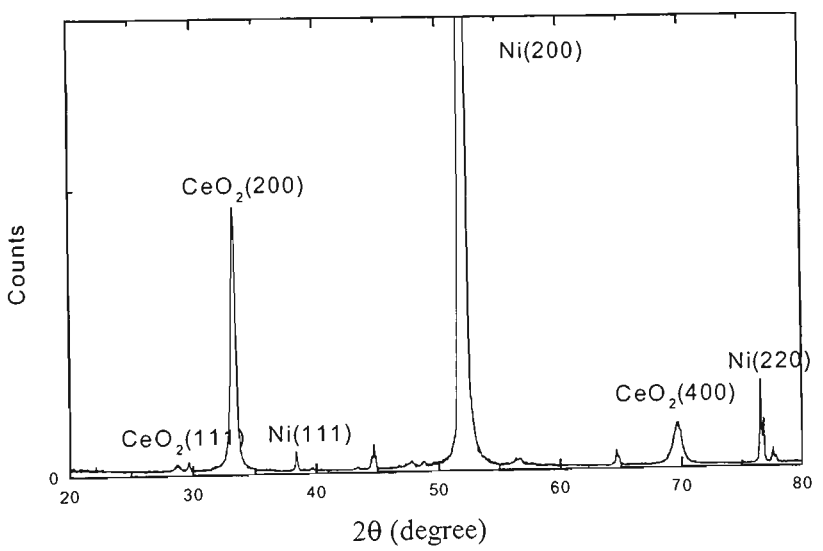

Figure 5.17. XRD θ-2θ scan of a CeO_2/Ni sample. I_C=I(200)/(I(200)+I(111))= 95.8%.

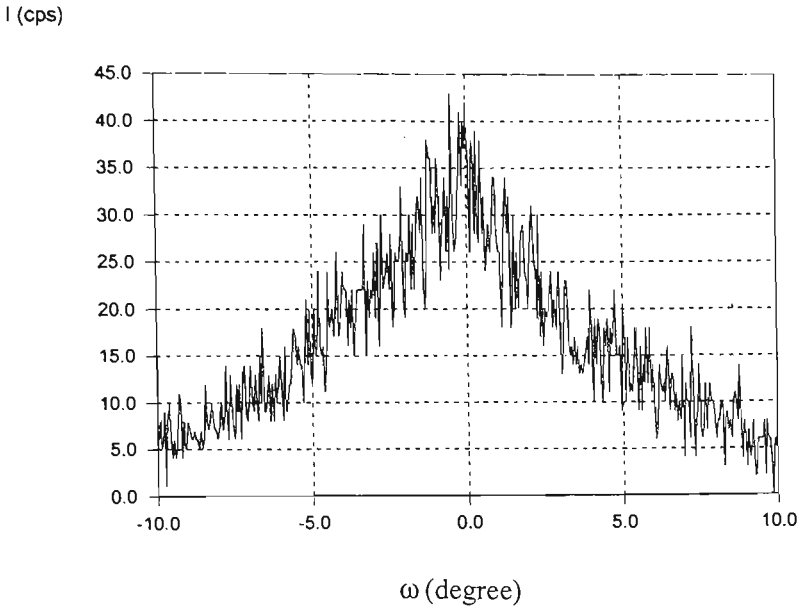

Figure 5.18. ω-scan of the (200) peak of a CeO_2 film on cubic textured Ni substrate. The value of the FWHM is 4.9°.

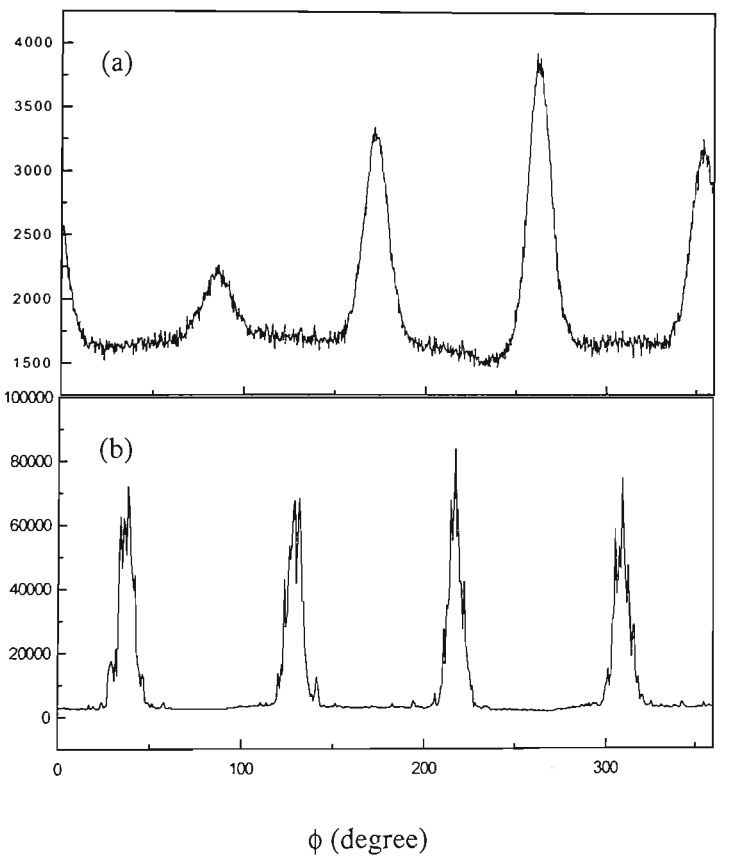

Figure 5.19. XRD ϕ-scans for the (111) peak of a CeO_2/Ni sample. (a): CeO_2 film; (b): Ni substrate. The CeO_2 principal crystallographic axes are rotated 45° relative to the in-plane Ni (100) axes.

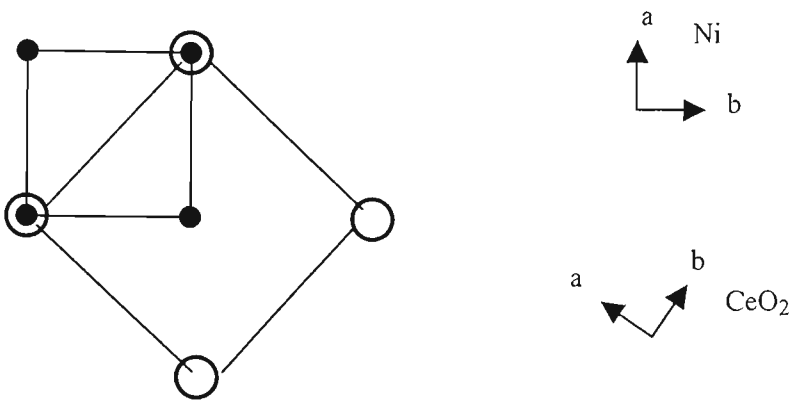

Figure 5.20. Schematic diagram of a 45° in-plane rotation in plane view, where the viewing direction is along the c-axis of the film and substrate. The a- and b- axes for Ni and CeO_2 in the two directions are indicated in the figure.

5.3.3 Microstructure and cracks in CeO_2 films

The CeO_2/Ni samples were analyzed by SEM. **Fig. 5.21** shows an SEM image of the surface of a CeO_2 film. There are uniform columnar grains of a size of about 100nm in diameter. **Fig. 5.22** shows the cracks in the CeO_2 film on the Ni substrate. These cracks are due to the thermal expansion mismatch between the Ni substrate ($\sim 16\times10^{-6}K^{-1}$) and the CeO_2 film ($\sim 12\times10^{-6}K^{-1}$). If an YBCO superconducting film is directly deposited on CeO_2/Ni, the interdiffusion between the YBCO and the Ni through the cracks significantly degrades the superconductivity of the YBCO film.

The following approaches were made to reduce or eliminate the cracks in CeO_2 films.

1. Deposit CeO_2 films with different thicknesses. The density of cracks is low while the thickness of a CeO_2 film is less than 10nm. However, such thin CeO_2 films can't be used as an single buffer layer due to the poor integrity caused by the surface roughness of the Ni substrate. There is no significant effect on the cracks in CeO_2 when the thickness of a CeO_2 film is increased from 10nm to 100nm.

2. First deposit CeO_2 film to 10nm using 100mTorr Ar + 10% H_2 at 395°, then deposit CeO_2 film to 100nm using 100mTorr O_2 at 790°C. This two step deposition method has been used by some groups to fabricate CeO_2 buffer layers on Ni. However in our work, Ni substrate is oxidized through the cracks at the high deposition temperature in O_2. The quality of the CeO_2 film is worse than that only using Ar + 10% H_2.

3. First deposit CeO_2 film to about 10nm using 3Hz, than deposit CeO_2 film to 100nm at 1Hz or 5Hz. For the 5Hz deposition, the cracking is worsen. For the 1 Hz deposition, the density of cracks is low and the cracks are narrow. (shown in **Fig. 5.22**).

A single crack-free CeO_2 buffer layer for YBCO coated conductor on an Ni substrate hasn't been achieved as yet. Further work is needed to continue this efforts in this direction.

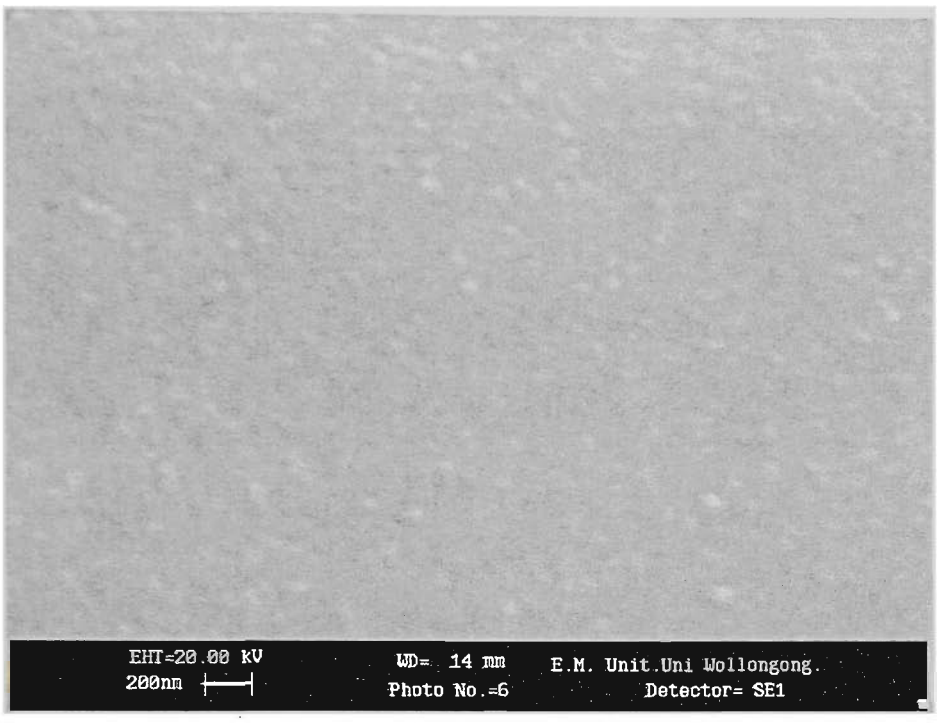

Figure 5.21. SEM image of a CeO_2 film on a cubic textured Ni substrates. There are uniform columnar grains with a diameter of about 100nm.

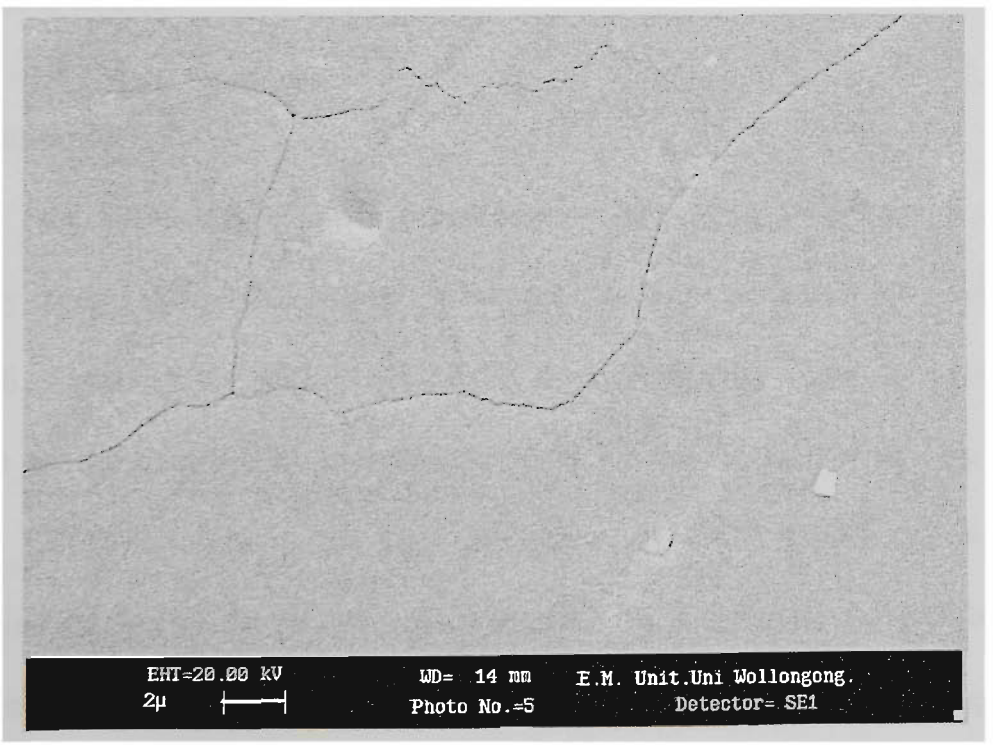

Figure 5.22. SEM image of CeO_2 film on a cubic textured Ni substrate. There is obvious cracking in the CeO_2 film.

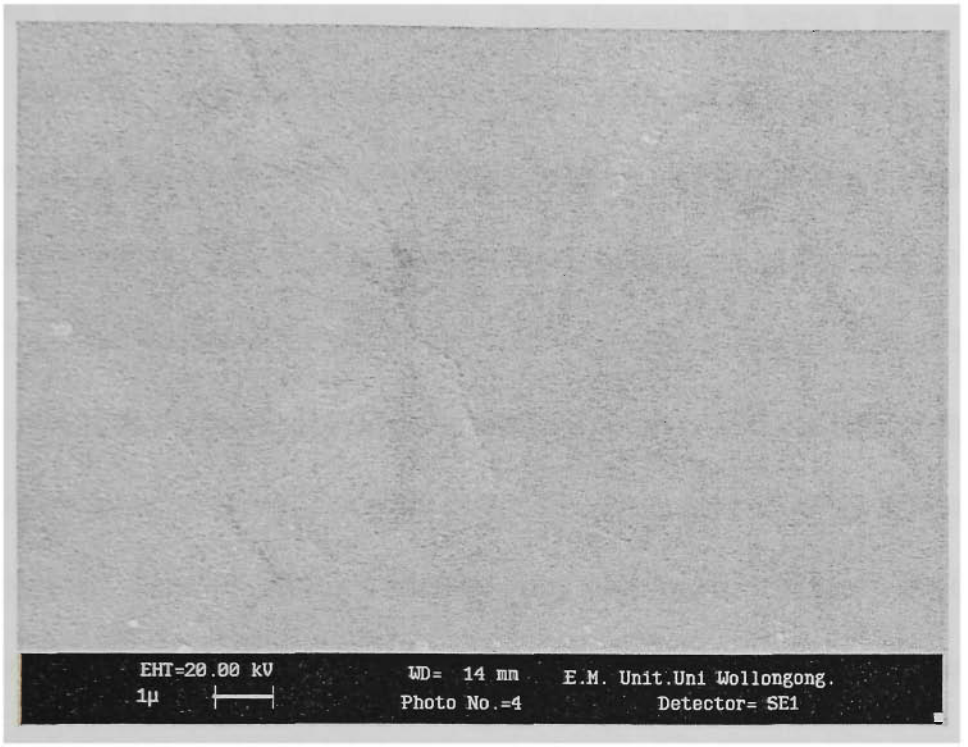

Figure 5.23. SEM image of a CeO_2 film on a cubic textured Ni substrate. The density of cracks in the CeO_2 film was reduced, and the width of the cracks is smaller.

5.4 Summary

One of the practically scalable processes for fabricating long lengths of flexible, biaxially textured, polycrystalline substrates involves a technique referred to as RABiTS. Epitaxial deposition of YBCO superconducting films on cubic textured metallic substrates provides a promising route for the fabrication of long lengths of high-J_c YBCO conductors. A key component of the RABiTS technique is the fabrication of buffer layers on cubic textured Ni substrates. Several buffer layer architectures involve the use of CeO_2 film deposited under a reducing atmosphere as the first layer of a multi-layered buffer, such as YBCO/YSZ/CeO_2/Ni or YBCO/CeO_2/YSZ/CeO_2/Ni .

In our research, we chose the reducing gas Ar + 10% H_2 for depositing CeO_2 films by PLD on cubic textured Ni substrates. The relationship between the texture of CeO_2 films and the deposition conditions was analyzed by adjusting the deposition temperature, deposition rate, deposition pressure, and the distance between the target and the substrate. The optimum deposition conditions are: deposition temperature 395°C; pulsed laser at 3Hz and 500mJ; Ar + 10% H_2 pressure of 100mTorr. Besides a target-substrate distance, the relative distance between the substrate and the plasma plume was found to be an important parameter. No matter what the size of the plume is, the optimum distance between the substrate and target is slightly beyond the plume (~5mm). At this distance, the deposited species are stoichiometric, and the energy of the deposited species is suitable for epitaxial growth. The degree of c-axis orientation, as given by I_c=I(200)/(I(111)+I(200)), is 95.8%. The FWHM of an XRD ω-scan and an optimum ϕ-scan of an optimum CeO_2 film are 4.9° and 12°, respectively. The shift of angles of ϕ-scans between a CeO_2 film and its Ni substrate proves that the CeO_2 principal crystallographic axes are rotated 45° relative to the in-plane Ni (100) axes, e.g. <110> CeO2//<100>Ni, which means that the growth of CeO_2 film on cubic textured Ni (100) substrate is in agreement with near-coincidence site lattice match modes.

Some attempts have been made to reduce the cracks in CeO_2 films. The deposition procedures of first depositing CeO_2 film up to 10nm at 3Hz, then depositing CeO_2 film at 1Hz up to 100nm can significantly reduce the density of cracks and make the cracks narrow.

Chapter 5 references

1. A. Goyal, D. P. Norton, J. D. Budai, M. Paranthaman, E. D. Specht, D. M. Kroeger, D. K. Christen, Q. He, B. Saffian, F. A. List, D. F. Lee, P. M. Martin, C. E. Klabunde, E. Hartfield, and V. K. Sikka, Appl. Phys. Lett. 69 (1996) 1795.
2. D. P. Norton, A. Goyal, J. D. Budai, D. K. Christen, D. M. Kroeger, E. D. Specht, Q. He, B. Saffian, M. Paranthaman, C. E. Klabunde, D. F. Lee, B. C. Sales, and F. A. List, Science, 274 (1996) 755.
3. S. W. Lu, F. A. List, D. F. Lee, X. Cui, M. Paranthaman, B. W. Kang, D. M. Kroeger, A. Goyal, P. M. Martin, and R. E. Ericson, Superconductor Science & Technology, 14 (2001) 218.
4. A. Goyal, R. Feestra, F. A. List, M. Paranthaman, D. F. Lee, D. M. Kroeger, D. B. Beach, J. S. Morrell, T. G. Chirayil, D. T. Verebelyi, X. Cui, E. D. Specht, D. K. Christen, and P. M. Martin, JOM (1999) 19.
5. M. Paranthaman, A. Goyal, F. A. List, E. D. Specht, D. F. Lee, P. M. Martin, Q. He, D. K. Christen, D. P. Norton, J. D. Budai, and D. M. Kroeger, Physica C 275 (1999) 266.
6. A Goyal, D. F. Lee, F. A. List, E. D. Specht, R. Feenstra, M. Paranthaman, X. Cui, S. W. Lu, P. M. Martin, D. M. Kroeger, D. K. Christen, B. W. Kang, D. P. Norton, C. Park, D. T. Verebelyi, J. R. Thompson, R. K. Williams, T. Aytug and C. Cantoni, Physica C 357-360 (2001) 903.
7. M. Yamazaki, T. D. Thanh, H. Kubota, Y. Kudo, H. Yoshino, and H. Nagamura, Advances in Superconductivity Vol11, ed N Koshizuka and Tajima (Tokyo:Spring) (1999) 789.

8. A. Kumart and J. Narayan, Supercond. Sci. Technol. 6 (1993) 662

9. M. Paranthaman, D. F. Lee, A. Goyal, E. D. Specht, P. M. Martin, X. Cui, J. E. Mathis, R. Feenstra, D. K. Christen, and D. M. Kroeger, Supercond. Sci. Technol. 12 (1999) 319

10. E. Y. Sun, A. Goyal, D. P. Norton, C. Park, D. M. Kroeger, M. Paranthaman, and D. K. Christen, Physica C 321 (1999) 29

11. D. K. Finnemore, K. E. Gray, M. P. Maley, D. O. Welch, D. K. Christen, and D. M. Kroeger, Physica C 320 (1999) 1.

12. A. Goyal, D. P. Norton, D. M. Kroeger, D. K. Christen, M. Paranthaman, E. D. Specht, J. D. Budai, Q. He, B. Saffian, F. A. List, D. F. lee, E. Hatfield, P. M. Martin, C. E. Klabunde, J. Mathis, and C. Park, J. Mater. Res., 12 (1997) 2924.

13. H. Makita, S. Hanada, and O. Izumi, Acta. Metal. Vol.36, No. 2 (1988) 403.

14. R. D. Doherty, D. A. Hughes, F. J. Humphreys, J. J. Jonas, D. J. Jensen, M. E. Kassner, W. E. King, T. R. McNelley, H. J. McQueen, and A. D. Rollett, Materials Science and Engineering A238 (1997) 219.

15. J.D.Budai, R. T. Young, B. S. Chao, Appl. Phys. Lett. 62, (1993) 1836.

Chapter 6. Fabrication of epitaxial NiO films on cubic textured nickel substrates by surface-oxidation epitaxy

6. 1. Introduction

Surface oxidation epitaxy (SOE) is a new approach to produce in-plane aligned NiO buffer layers on cubic textured Ni substrates for YBCO coated conductors. The main characteristic of this method is that a cubic-textured NiO layer is made by controlled surface oxidation of a cubic-textured nickel or nickel alloy ribbon, in an electric furnace [1-5]. NiO has an face-centered cubic unit cell with a lattice parameter of 4.17Å similar to the lattice parameter of MgO, which is a well-known substrate for YBCO film growth. Also, a NiO layer provides a suitable barrier for the protection of the YBCO film from adverse chemical interactions with the nickel substrate.

The degree of in-plane texture of NiO films fabricated by SOE method, evaluated by the FWHM of ϕ-scans, is not much lower than those by IBAD or RABiTS methods [6-11]. However, as reported, the critical current density of an YBCO film deposited by the pulsed laser deposition (PLD) on a cubic-textured NiO film, previously fabricated by SOE from cubic-textured Ni, was between 4 x10^4 Acm^{-2} and 6 x10^4 Acm^{-2} (at 77K, and 0T) [12]. This value is approximately two orders of magnitude lower than the critical current density of an YBCO/CeO_2/Ni tape where the CeO_2 buffer layer is produced by PLD using IBAD on randomly-oriented Ni, or by PLD on cubic textured Ni [13,14].

An explanation for this difference in J_c is the low quality of the surface of the NiO films fabticated by SOE. The growth of a NiO film through an oxidation process is difficult to

precisely control compared to PLD or other vapour deposition techniques such as magnetron sputtering, and as a consequence, there are many microcracks in the NiO film, Nickel contamination in YBCO films may occur in the vicinity of the microcracks, since the diffusion of nickel is rapid there. The nickel reduces the T_c of the YBCO films. On the other hand, the surface roughness of NiO films is relatively high. This increased roughness is reflected in the increase of the full width at half maximum (FWHM) of the XRD ω-scans of the NiO films, as compared to CeO_2 films deposited by IBAD and PLD or by PLD on the similar cubic textured Ni substrates[15].

Therefore, although the growth of a NiO buffer layer by SOE is an appealing option, the above-mentioned problems indicate the importance of improving the quality of the NiO buffer layer. The enhancement of the surface quality of the NiO film is necessary for obtaining high J_c.

In this study we investigated the thermal oxidation process in three atmospheres (air, flowing oxygen, and flowing Ar + 8% O_2) in order to achieve a highly biaxially textured NiO film on cubic textured Ni substrates. Fabrication of {100}<001> NiO films was analysed by careful control of oxidation atmosphere, oxidation temperature, and oxidation time as well as the rate of heating and cooling. The surface morphology including the microcracks and surface roughness was analysed by SEM and AFM.

6.2 Experiment

All of the NiO film samples used in this investigation were grown on {100}<001> cubic textured Ni substrate. The Ni substrate was 0.15mm thick, fabricated by a standard procedure, using a large reduction cold rolling and re-crystallization method.The cubic texture of Ni substrates were investigated at Chapter 5 by XRD pole figures (**Fig. 5.4**), ω-scans (**Fig. 5.5**), and ϕ-scans (**Fig. 5.6**).The smallest values of the FWHM of the ω-scans for the (200) and the ϕ-scans for the (111) plane are about 6° and 8° respectably, which means that the Ni substrates have a good c-axis and a-b in-plane textures. The Ni samples were cut to a size of $8\times13mm^2$ for experimental samples.

Fig. 6.1 shows an AFM image of the surface of a typical Ni substrate. Note that there are many grain boundary grooves which were caused by the thermal treatment. The average roughness of the as-recrystallised Ni substrates determined by atomic force microscopy (AFM) on $(40x40)\mu m^2$ scans was about 120nm Rms. This value was reduced by electro- polishing, down to 24nm, which is comparable with the average roughness of a polished ceramic substrate. A similar (111) pole figure and a ϕ-scan were performed on a Ni substrate after electro-polishing, and the results indicated that the cubic texture was not affected by the electro-polishing process.

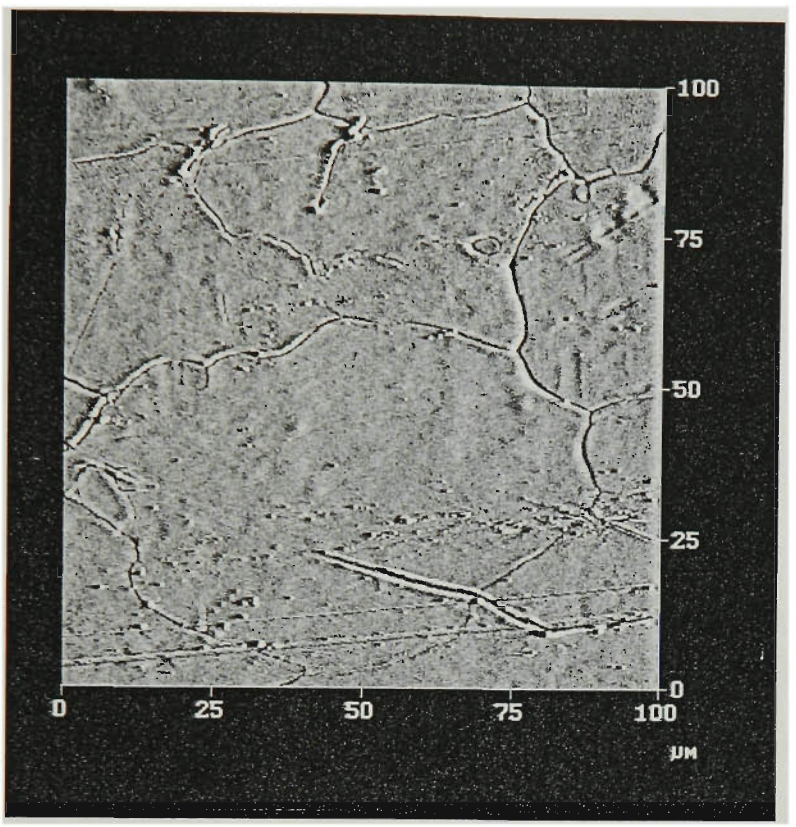

Figure 6.1 AFM image of the surface of a cubic textured Ni substrate. Many grain boundary grooves caused by the thermal treatment present on the surface.

Before the oxidation, the Ni substrates were cleaned with detergents and organic solvents using an ultrasonic cleaner. The oxidation of the Ni substrates was carried out in an electric tube furnace. The surface oxidation was done in air, in flowing oxygen ($P_{O_2} \sim 1$ atm) , or in flowing Ar + 8% O_2 ($P_{Ar+8\%O_2} \sim 1$ atm) at temperatures ranging from 800°C to 1200°C, for between 30 s and 5h. In order to precisely control the oxidation time, Ar was flushed into the furnace after the oxidation reaction finished, and the samples were allowed to cool down to room temperature inside the furnace. The rates of heating and cooling were maintained to ensure similar conditions through the investigation.

Optical microscopy, SEM and AFM were used to investigate the surface morphologies of the Ni substrates and NiO layers. X-ray diffraction (XRD) θ-2θ scans, ω-scans, ϕ-scans and X-ray pole figures were used to measure the texture of the Ni substrates and NiO layers.

6.3. Results and discussion

6.3.1. Fabrication of NiO films using different atmospheres

NiO film is formed on a Ni surface by oxidation. In the initial stage of the oxide formation, an epitaxial relationship can exist between the crystal orientation of the growing NiO and the underlying Ni surface [16]. With increasing thickness of the NiO film, the texture of the NiO changes depending on the oxidation temperature, the oxidation time, and the oxidation atmosphere. X-ray diffraction θ-2θ scan data showed evidence for a c-axis orientation of NiO surface layers. The ratios of (200) NiO to (111) NiO were calculated from XRD peak intensities then compared to determine the best annealing for achieving a c-axis oriented NiO film on an Ni substrate. For the NiO/Ni samples with good c-axis orientation, XRD ω-scans, ϕ-scans and pole figures were used to investigate the cubic texture of the NiO film.

A. Oxidation in air

Ni substrates were oxidized in air at temperatures ranging from 800- 1200°C for a time ranging from 1 min to 1h. The texture of a NiO layer grown on a cubic textured Ni substrate is strongly influenced by the oxidation temperature and the oxidation time.

Fig. 6.2 shows the dependence of the c-axis orientation on the oxidation temperature for a 10 min reaction time, assessed by XRD θ-2θ scans. It is evident that between 1110°C and 1130°C, there is only a small of the NiO (111) reflection. The minimum is located at 1115°C.

Fig. 6.3 shows the relationship between the c-axis orientation and the oxidation time at 1120°C, assessed by XRD θ-2θ scans. This result indicates that between 5 min and 15 min reaction time, there is a maximum in the ratio of the intensities of the (200) to the (111) reflections of the NiO layer which located around a reaction time of 10 min.

The XRD θ-2θ scan for a NiO/Ni sample obtained at 1120°C for a reaction time of 10 min, shown in **Fig. 6.4**, reveals that the NiO layer has a strong c-axis orientation vertical to the broad face of the Ni substrate. A quantitative assessment of the c-axis orientation can be defined by $I(200)/\{I(200)+I(111)\}$, where $I(200)$ and $I(111)$ are the XRD θ-2θ scan intensities for the (200) and (111) peaks. For the sample with θ-2θ scan presented in **Fig. 6.4**, this ratio $I(200)/\{I(200)+I(111)\}$=95.2%, which represents a strong c-axis orientation. **Fig.6.5** shows the XRD pole figures for the (111) and the (200) planes of NiO oxidized at 1120°C for 10 min in air, which means that the NiO film has a partial cubic texture.

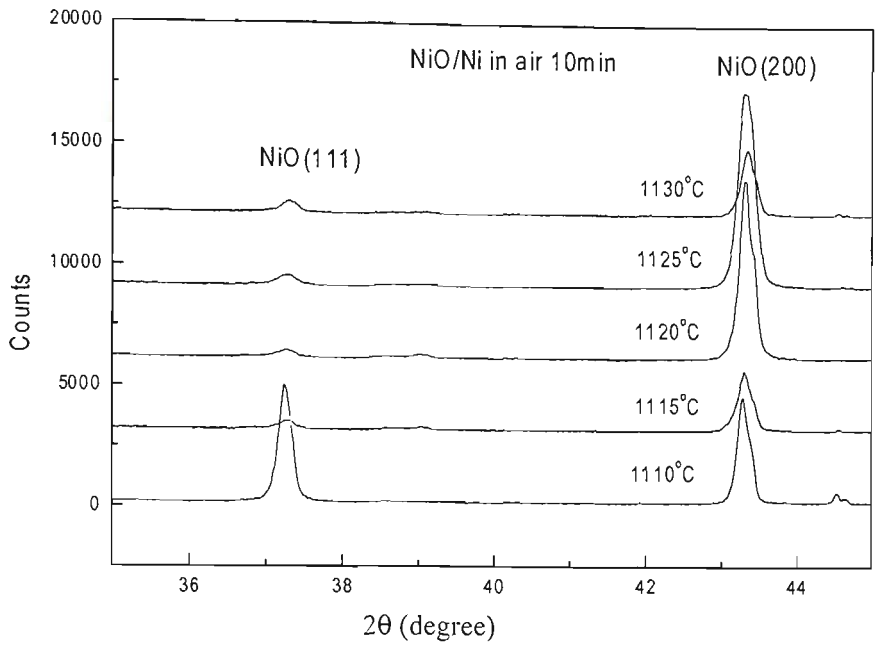

Figure 6.2 XRD θ-2θ scan of a NiO/Ni sample at different oxidation temperatures and for an oxidation time of 10 min.

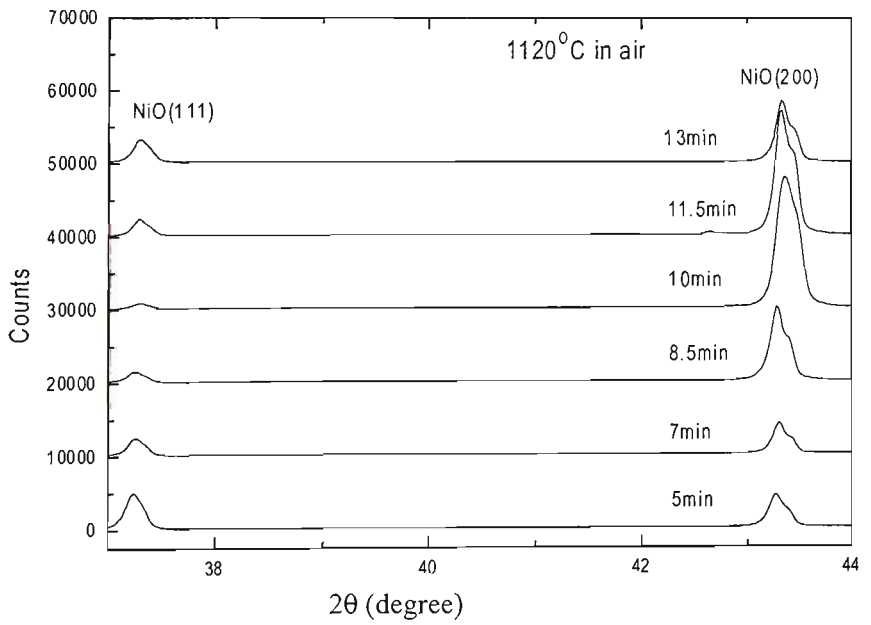

Figure 6.3 XRD θ-2θ scan of a NiO/Ni sample at an oxidation temperature of 1120°C and for different oxidation times.

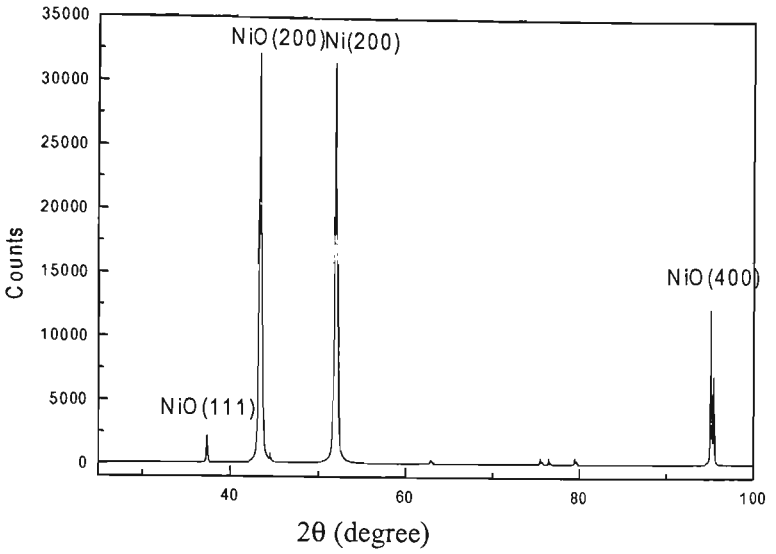

Figure 6.4 XRD θ-2θ scan of a NiO/Ni sample; I_c = I(200)/(I(200) + I(111)) = 95.2 %.

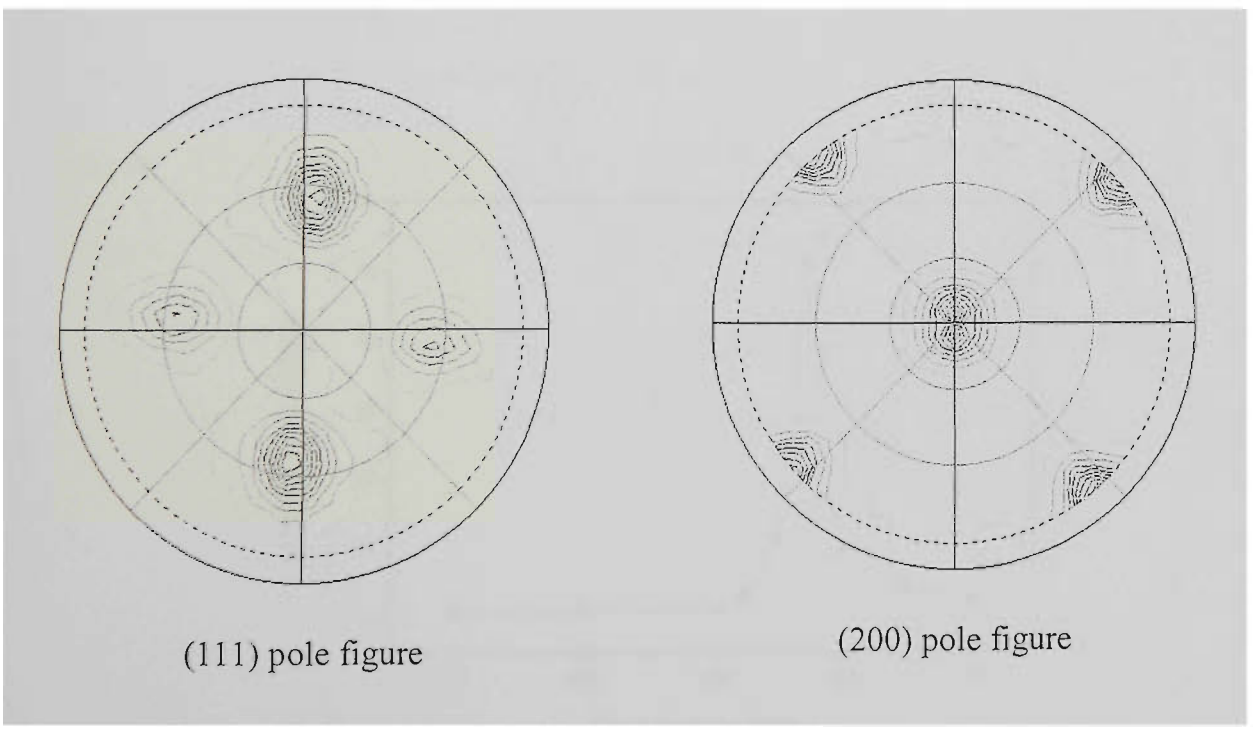

Figure 6.5 Pole figures of a NiO film oxidized in air.

B. Oxidation in flowing oxygen

Similar analyses were carried out for the surface oxidation of Ni to form a cubic textured NiO layer in flowing oxygen (P_{O2} ~ 1 atm) at temperatures ranging from 800°C to 1200°C, for between 1 min and 90 min. A plot of the ratio of *I*(200) to *I*(111) at different temperatures for a constant annealing time of 10min showed a maximum at 1075°C (**Fig. 6.6**). Hence there exists a narrow optimum or critical conditions at which the formation of (200) is favorable. The texture of NiO is decided by the kinetic energy of oxidation. The Ni oxidation starts with the formation of NiO nucleuses and islands. At an oxidation temperature of 1075°C, a c-axis orientation makes the energy of a NiO film the smallest. Oxidation at a temperature lower or higher than 1075°C failed to produce well textured (200) NiO.

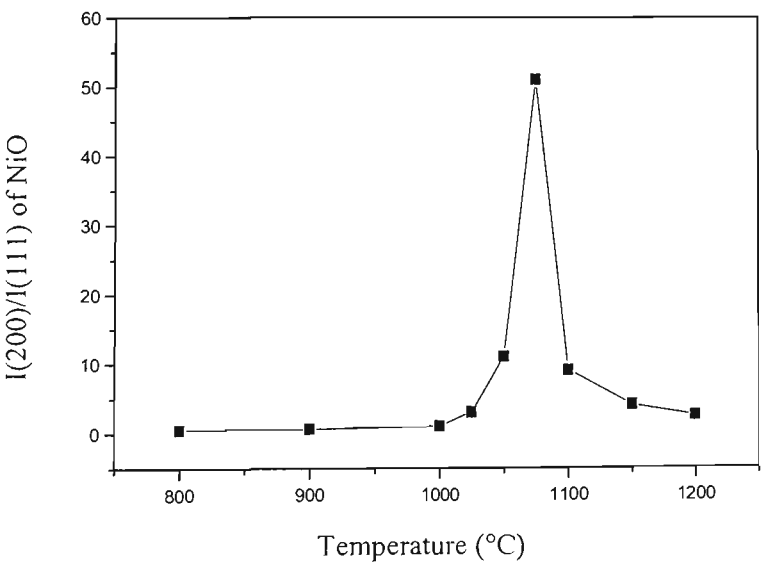

Figure 6.6 I(200)/I(111) of a NiO oxidized at different oxidation temperatures in flowing oxygen (P_{O2} ~ 1 atm) for 10min.

In order to accurately control the oxidation process, samples were put into the furnace at the oxidation temperature, and the furnace was evacuated and then flushed with pure flowing Ar as the samples were cooled. The cubic texture obtained using O_2 is better than when using air, and the degree of the c-axis texture quality defined by $I(200)/\{I(200)+I(111)\}$ is 98%.

Fig. 6.7 shows the pole figures of XRD for the (111) and (200) planes of NiO oxidized at 1075°C for 10min in flowing O_2, and it is clear that cubic texture is stronger than that for oxidized in air. **Fig. 6.8** shows the ω-scan of the same NiO layer for the (200) peak; the value of FWHM is about14°. Comparing with the FWHM value of the Ni (200) peak of 6°, the out-of-plane orientation is not as good as for other buffer layers fabricated by sputtering or PLD method. **Fig. 6.9**(a) shows the ϕ-scan of the NiO layer for the (111) plane, and the value of FWHM is about 12°. The lattice constant of Ni and NiO are 3.52Å and 4.18Å respectively, so the lattice mismatch is about 16%. Comparing with the ϕ-scan of Ni (111) for the same NiO/Ni sample, shown in ϕ-scan pattern (b), the peaks of the ϕ-scan of NiO film is at the same angle as the ϕ-scan peaks of the Ni. This proves that the epitaxial orientation in this case is <100> NiO//<100>Ni.

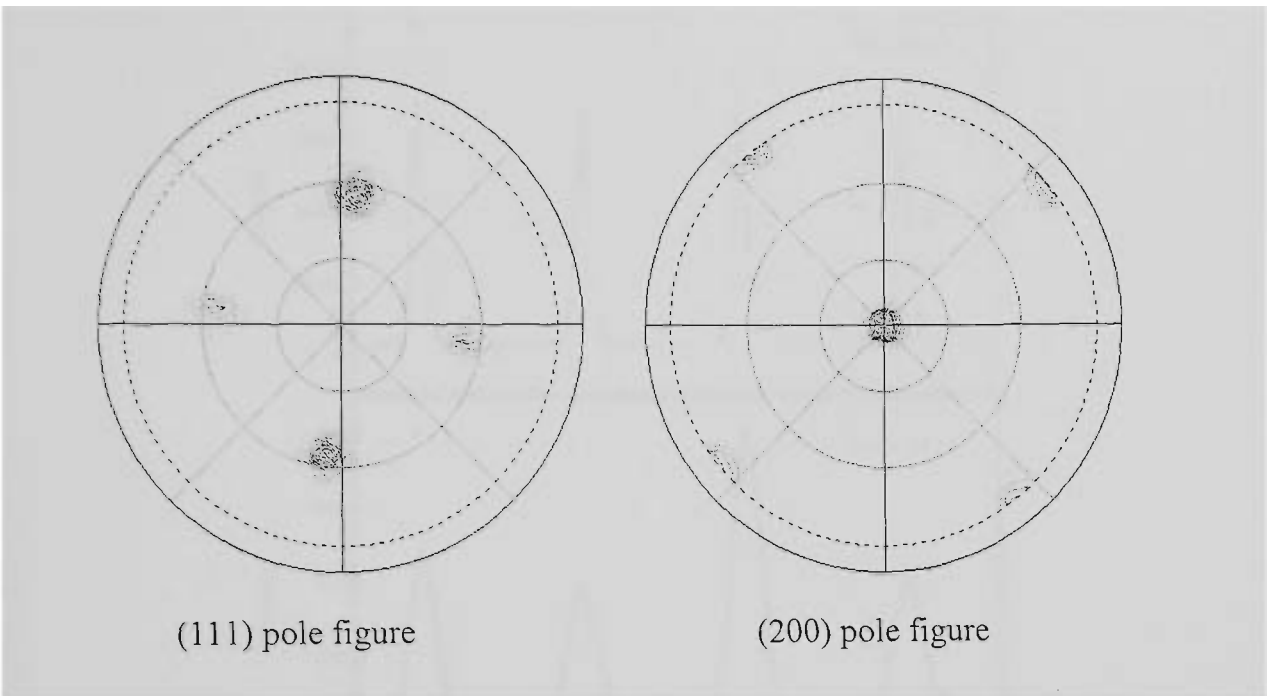

Figure 6.7 Pole figures of a NiO film oxidized in flowing oxygen (P_{O_2} ~ 1 atm).

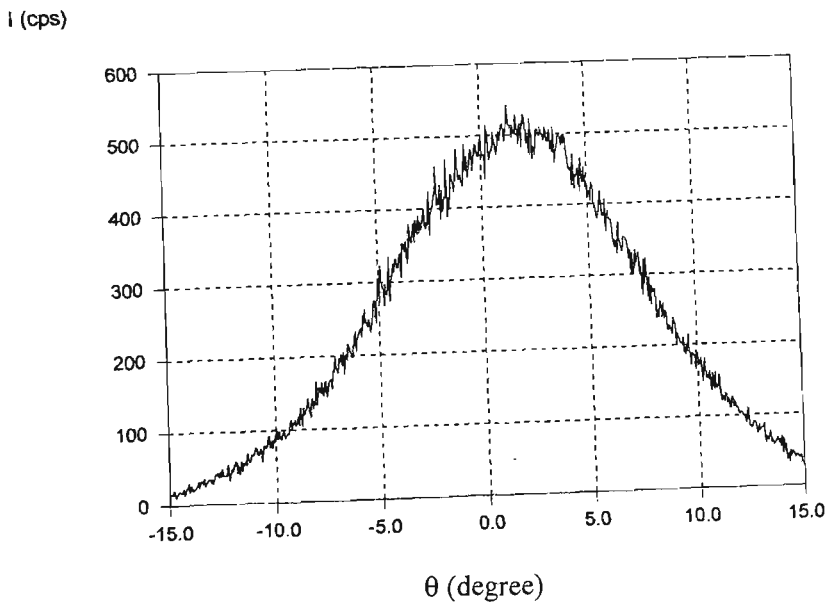

Figure 6.8 XRD ω-scan for the (111) peak of a NiO oxidized in flowing oxygen on a cubic textured Ni substrate; the FWHM value is ~ 14°.

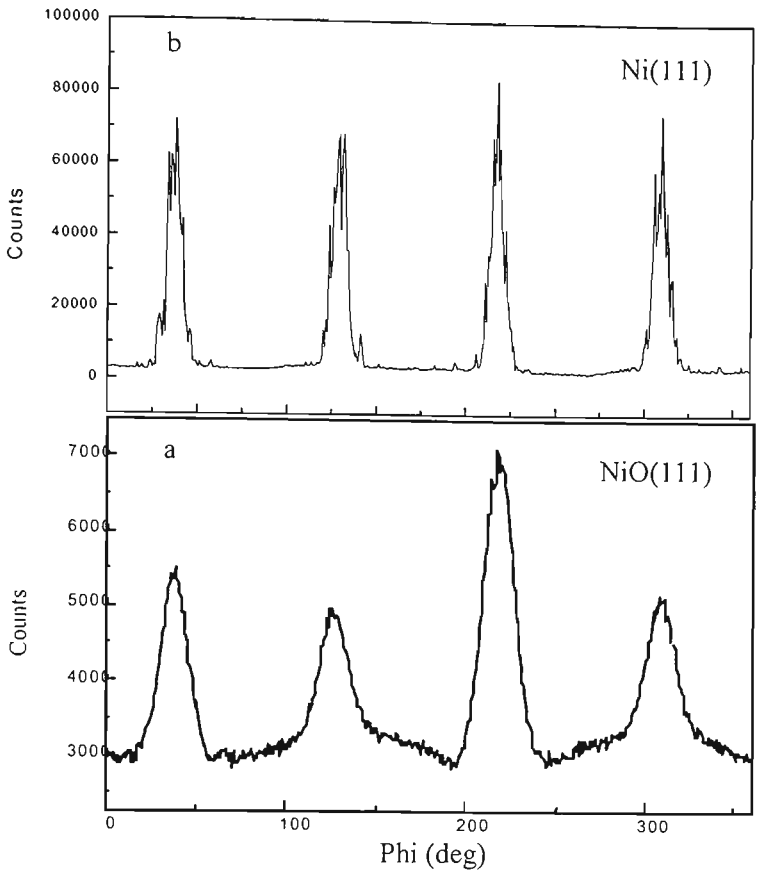

Figure 6.9 XRD ϕ-scans for the (111) peaks of a NiO/Ni sample. (a): NiO film; (b): Ni substrate. The NiO principal crystallographic axes are parallel to the in-plane Ni axes, e.g. <100>NiO//<100>NiO.

C. Oxidation in flowing Ar + 8% O_2

The purpose of using Ar+ 8% O_2 in the oxidation is to slow the process of oxidation and accurately control the oxidation parameters in order to obtain a better cubic texture. When the Ni was oxidized in flowing Ar + 8% O_2 ($P_{Ar+8\%O2}$ ~ 1 atm), the formation of (200) NiO was favourable, but with some (111) NiO present. The maximum ratio being 4:1, and the amount of (111) NiO could not be reduced by longer oxidation (~5h).

Fig.6.10 shows the XRD pole figures of the (111) and (200) planes of NiO oxidized in flowing Ar + 8% O_2, which means that the cubic texture is weak. Oxidizing under low

oxygen partial pressure did not promote epitaxial growth of (100) NiO. In fact, a significant (111) NiO peak was always present.

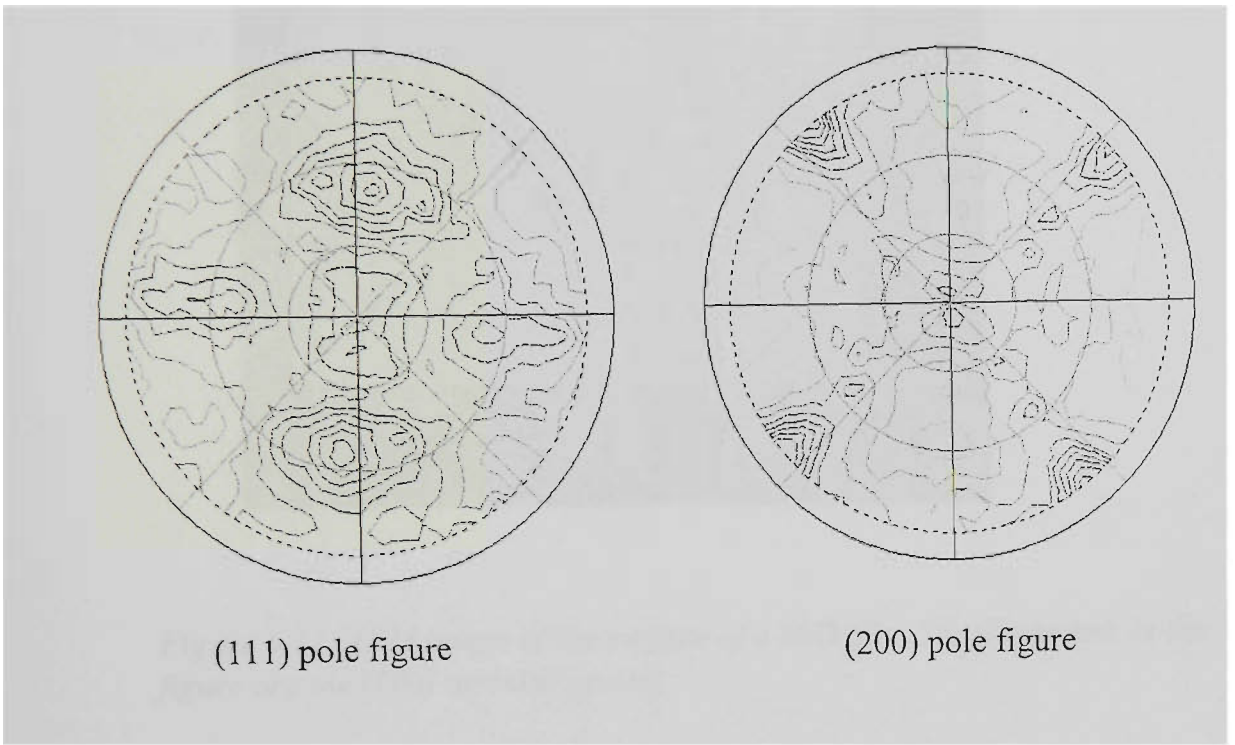

Figure 6.10 XRD pole figures of a NiO film oxidized in Ar + 8% O_2.

6.3.2. Microstructure analysis

Apart from the crystallographic orientation of the buffer layer, other properties such as surface roughness, cracks and continuous coverage of the substrate are also very important in preserving the superconducting properties of the YBCO film. Generally, the preferred orientations of NiO grown on an Ni(200) surface are NiO (111) and NiO (200). The (100) oriented NiO grain has a flat face at the film surface, and **Fig. 6.11** presents an AFM image of (200) NiO grains. In contrast, (111) grains on the surface of NiO film have a pyramidal-like shape which consists of four (111) planes (**Fig. 6.12**).

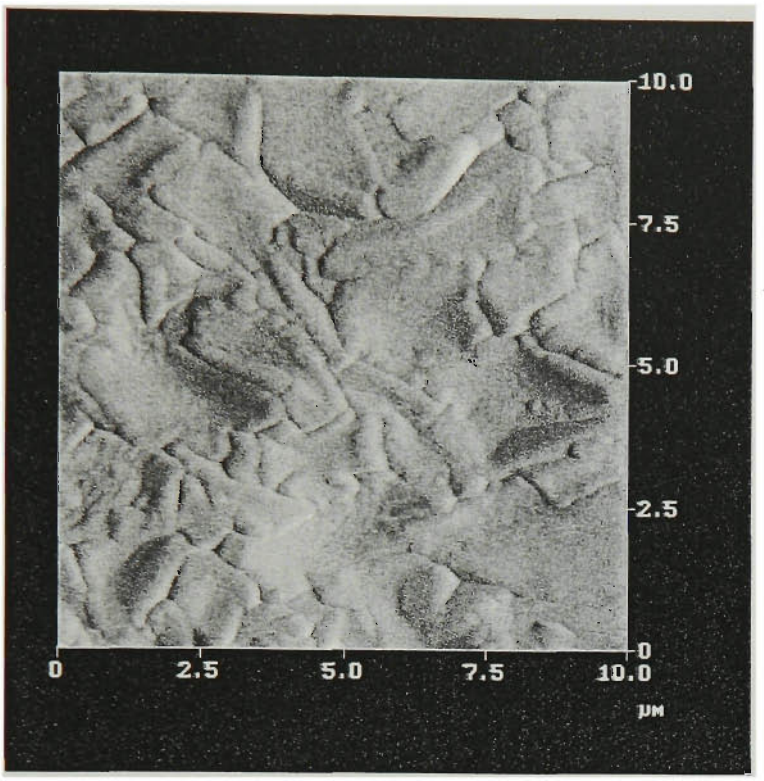

Figure 6.11 AFM image of the surface of a NiO film. The flat grains in the figure are the (100) oriented grains.

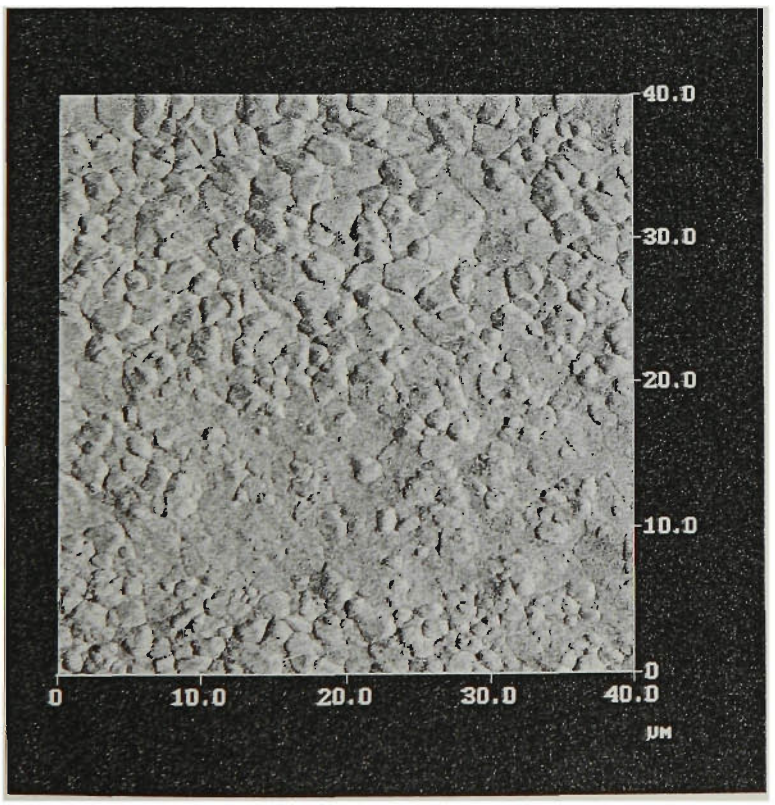

Figure 6.12 AFM image of a NiO film. The pyramid-like grains in the figure are (111) oriented grains.

For oxidation in flowing Ar + 8% O_2, the (200) and (111) orientated grains are mixed, so that the grains do not form a flat plane and the surface roughness is very high (**Fig. 6.13**). For oxidation in air and flowing oxygen (P_{O_2}~1 atm), the formation of the (200) is highly preferred. **Fig. 6.14** shows that in this case, the grains have flat faces on the top of the surface, and the surface roughness is small.

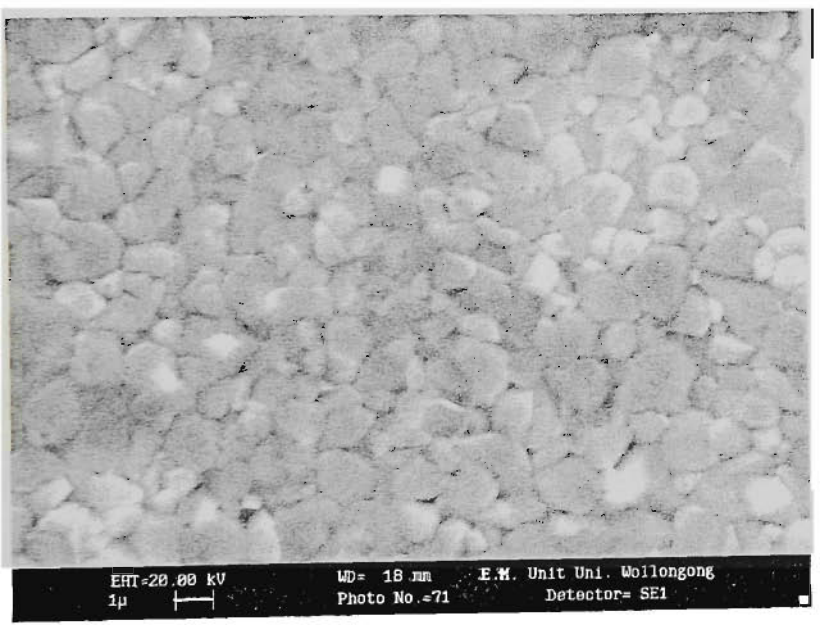

Figure 6.13 For a NiO film oxidized in flowing Ar + 8%O_2 with a low ratio of (200) to (111) peaks, the surface of the film is not flat.

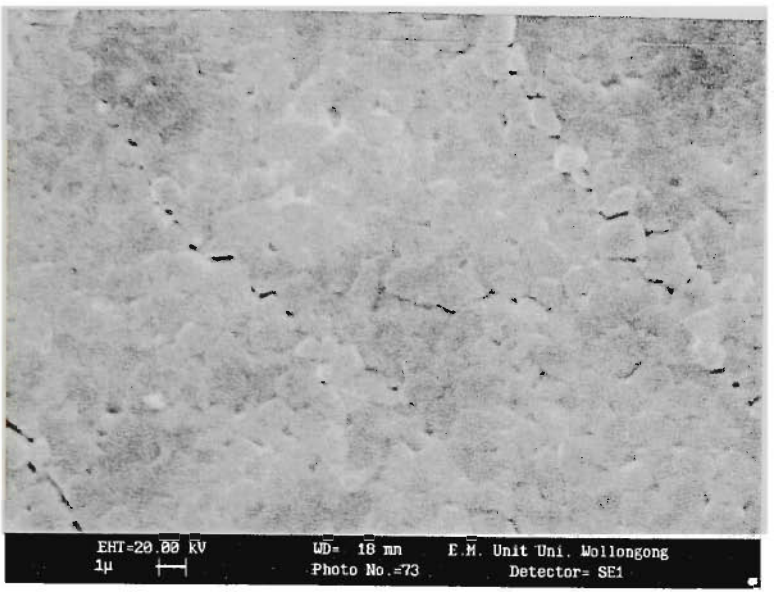

Figure 6.14 For a NiO film oxidized in flowing O_2 with a strong (200) orientation, the (200) NiO planes form large flat surfaces and grow at the expense of the other orientations.

In **Fig. 6.14**, it can be seen that there are several microcracks in the NiO film. The microcracks in NiO buffer layers provide a source for the local contamination of YBCO, since the diffusion of nickel is rapid in the vicinity of these cracks, and significantly reduces the J_c of the YBCO material. The thermal expansion coefficient of NiO is 17.1×10^{-6} K^{-1}, and this value is comparable with that of nickel ($\sim16\times10^{-6}$ K^{-1}), so that the microcracks were not caused by thermal expansion. These microcracks were caused by the stress due to the oxidation of Ni, for instance, that caused by the expanding volume with NiO formation. The microcracks can be reduced by slowly relieving the stress. Whatever atmospheres were used, in the case of a fast cooling rate from the oxidation reaction temperature, cracks often appeared in the NiO film. For very fast cooling rates, the NiO layer even exfoliates from the Ni substrate. Such a catastrophic breakdown of the NiO layer takes place when a cooling rate is higher than

approximately 100°C/min, whereas the cooling rate lower than 10°C/min can significantly reduce the microcracks. In our work the oxidation time was controlled by introducing Ar gas into the furnace, which makes the oxidation time independent of how long the sample was kept in the furnace. A continuous, non-fractured NiO layer was obtained for a sample-cooling rate of approximately 6°C/min.

The surface roughness is another problem for the surface oxidation epitaxy. It is also one of the reasons why the out-of-plane orientation of an NiO layer fabricated by SOE, as reflected by the FWHM of the ω-scan, is much worse than for buffer layers fabricated by vacuum deposition methods, such as sputtering and PLD on similar Ni substrates. This out-of-plane orientation also affects the J_c of YBCO films. The surface roughness of NiO after surface oxidation is much worse than for the original Ni substrate. Note that electro-polishing was used to polish some Ni substrates, and can reduce the surface roughness Rms from 120nm to 24nm. **Fig. 6.15** shows the AFM image of a Ni surface after the electro-polishing, and it can be seen that the surface of as-polished Ni is very smooth without grooves associated with grain boundaries on the surface of such Ni substrates. However, after the same oxidation process, the surface roughness is still very poor, similar to that for NiO oxidized from an un-polished Ni substrate. This means that the original surface roughness is not the cause of the surface roughness of NiO films.

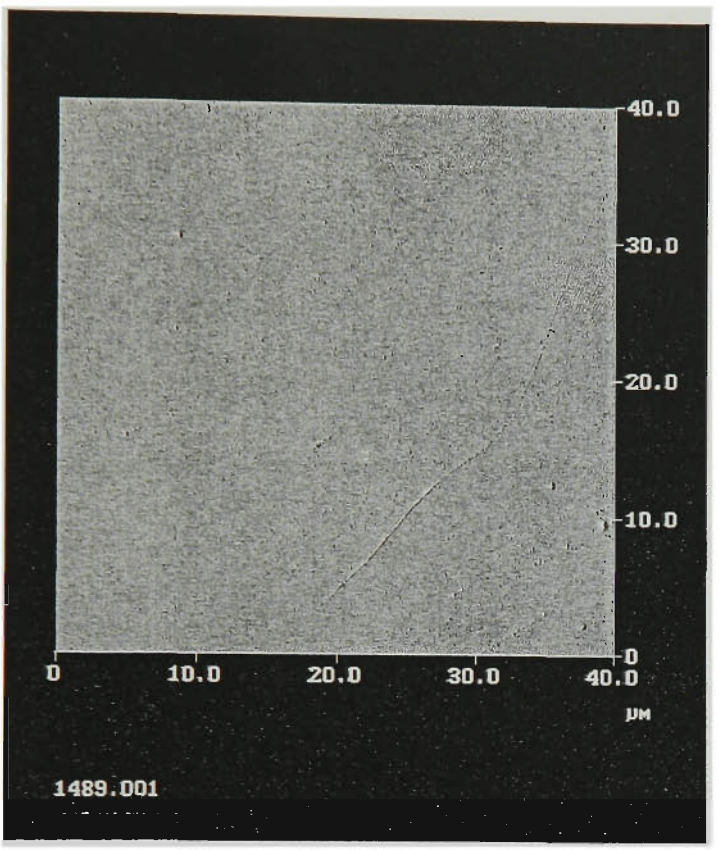

Figure 6.15 AFM image of the surface of a Ni substrate after electro-polishing.

Some of the roughness of such NiO film is caused by (111) oriented grains that have pyramid-like tops (**Fig.6.12**). Another cause of the worse surface roughness is that there are many circular spots that appear on the surface of NiO films regardless of oxidation atmosphere. **Fig. 6.16** is an optical image of a NiO film, and it shows numerous spots on the NiO surface. The diameter of the spots is ~10μ. It was once thought that such spots were caused by dust falling on the surface during oxidation in the furnace. However, the spots remained the same when the furnace environment was improved. A more accurate examination around these circular spots was carried out by AFM on a (40x40)μm^2 scan, and the result is presented in **Fig. 6.17** which is evident

that the spots represent clusters of grains which are larger than average grains of NiO. This grain coarsening takes place not only in the (x, y) plane, which corresponds to the (a, b) crystallographic plane of the NiO layer, but in the z-direction as well, leading to an increase in the roughness of the NiO layer. Moreover, these spots may cause weak-link behaviour for YBCO film grown on top of them. The specific gravities of NiO and Ni are 5.7 and 8.9 g/cm^3 respectively. When the surface of the Ni substrate is oxidized into NiO, the NiO occupies a larger volume than the Ni before oxidation. The coarse spots may be caused by a localised tension in the NiO layer, originating in the difference in volume of the NiO and Ni unit cells. A way to reduce these coarse spots is to reduce the thickness of the NiO film by the oxidation time. Compared with some reports in which the oxidation time is up to several hours [15], the oxidation time in our experiment is just about 10 min, which can make the NiO film continuous and relatively smooth. Moreover, the efficiency of the oxidation is higher.

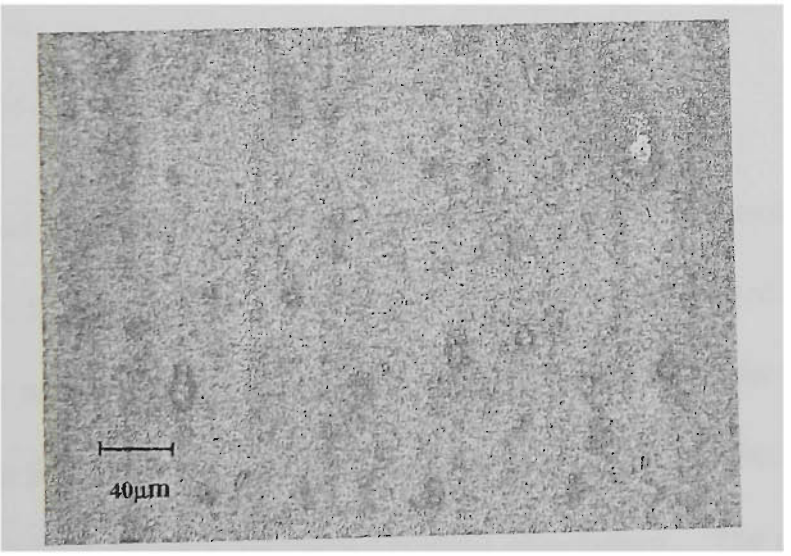

Figure 6.16 Optical microscope image of a NiO film. There are numerous spots which make the surface of the NiO rougher.

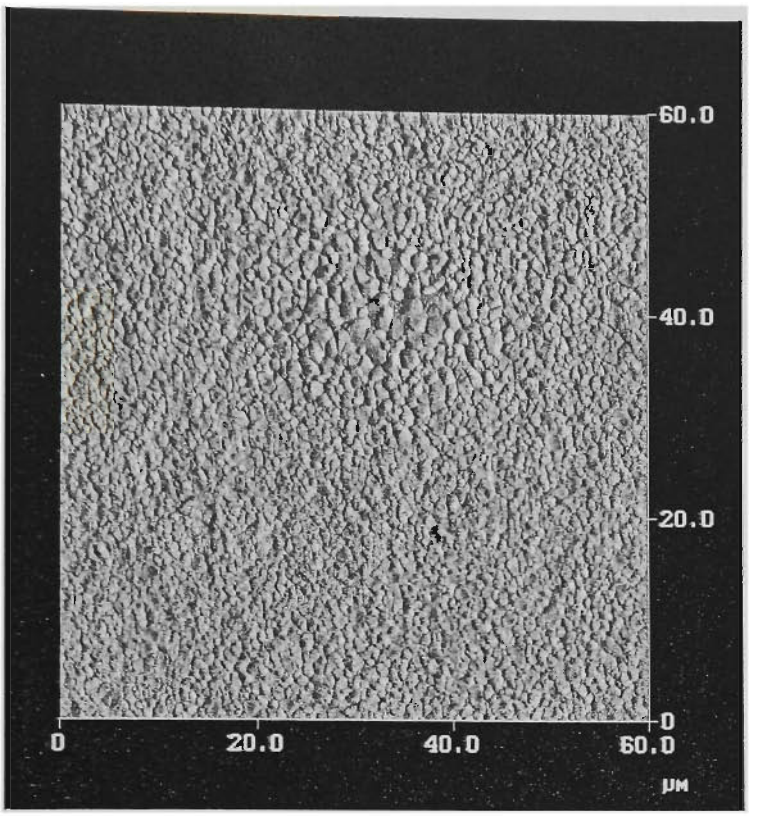

Figure 6.17 AFM image of a NiO film. It is revealed that the spots are groups of large grains.

6.4. Summary

Biaxially textured NiO films were fabricated by the surface oxidation epitaxy. Three atmospheres, air, flowing oxygen, and flowing Ar +8% O_2, were used in the oxidation process in order to improve the biaxial texture and control the surface quality of NiO film. A NiO film formed in flowing oxygen (P_{O_2}~ 1 atm) at an oxidation temperature of 1075°C for 10min has strong c-axis and a-b plane orientations. The c-axis orientation of high quality NiO films was evaluated by XRD, and the FWHM value of the ω-scan for the (111) peak was approximately 14°. XRD pole figures and ϕ-scans were used to investigate the a-b plane texture, and the FWHM value of the ϕ-scan for the NiO(111)

peak was approximately 12°. The quality of biaxially textured NiO films oxidized in air is lower than for oxidation in flowing oxygen. There was no way to obtain a strong c-axis preference in a NiO film when a Ni was oxidized in Ar + 8% O_2.

The morphologies and microdefects of NiO films were systematically investigated. The microcracks and surface roughness of NiO films are more serious than for other buffer layers deposited by vacuum deposition methods. A slow cooling rate can reduce the density of microcracks on the surface of NiO by slowly relieving the stress stored in NiO films. The more (100) oriented the grains are, the smoother the surface of the NiO film is. The increased roughness of a NiO layer is also caused by clusters of relatively larger NiO grains which form numerous circular spots on the surface of the NiO film. It is thought that these spots were caused by the relief of localised tension in the NiO layer resulting from the difference in volume of the NiO and Ni unit cells. Decreasing the thickness of the NiO film by shortening the oxidation time can reduce the density of these coarse spots on the surface of NiO films.

Chapter 6 references

1. K. Maatsumoto, Y. Niiori, I. Hirabayashi, N. Koshizuka, T. Watanabe, Y. Tanaka and M. Ikeda, 1998 Advances in Superconductivity, Vol 10, ed K Osamura and I Hirabayashi (Tokyo:Springer) p 611.
2. Z. Lockman, X. Qi, Andrey Berenov, Rainer Nast, Wilfried Goldacker and J. MacManus-Driscoll, Physica 351 (2001) 34.

3. Tomonori Watanabe, Kaname Matsumoto, Toshihiko Maeda, Toru Tanigawa, and Izumi Hirabayashi, Physica C 357-360 (2001) 914.

4. T. Watanabe, K. Matsumoto, T. Maeda, T. Tanigawa and I. Hirabayashi, Physica C 357-360 (2001) 914.

5. V. Boffa, T. Petrisor, G. Celentano, F. Fabbri, C. Annino, S. Ceresara, L. Ciontea, V. Galluzzi, U. Gambardella, G. Grimald and A. Mancini, Supercond. Sci. Technol. 13 (2000)1467.

6. H. C. Freyhardt, J. Weismann, K. Heinemann, J. Hoffmann, J. Dzick, A. Usoskin, F. Garcia-Moreno, and S. Sieves, IEEE Trans. Appl. Supercond. 7 (1997) 1426

7. A. Goyal, R. Feestra, F. A. List, M. Paranthaman, D. F. Lee, D. M. Kroeger, D. B. Beach, J. S. Morrell, T. G. Chirayil, D. T. Verebelyi, X. Cui, E. D. Specht, D. K. Christen, and P. M. Martin, JOM (1999) 19.

8. D. P. Norton, A. Goyal, J. D. Budai, D. K. Christen, D. M. Kroeger, E. D. Specht, Q. He, B. Saffian, M. Paranthaman, C. E. Klabunde, D. F. Lee, B. C. Sales, and F. A. List, Science, 274 (1996) 755.

9. A Goyal, D. F. Lee, F. A. List, E. D. Specht, R. Feenstra, M. Paranthaman, X. Cui, S. W. Lu, P. M. Martin, D. M. Kroeger, D. K. Christen, B. W. Kang, D. P. Norton, C. Park, D. T. Verebelyi, J. R. Thompson, R. K. Williams, T. Aytug and C. Cantoni, Physica C 357-360 (2001) 903.

10. A. Goyal, D. P. Norton, J. D. Budai, M. Paranthaman, E. D. Specht, D. M. Kroeger, D. K. Christen, Q. He, B. Saffian, F. A. List, D. F. Lee, P. M. Martin, C. E. Klabunde, E. Hartfield, and V. K. Sikka, Appl. Phys. Lett. 69 (1996) 1795.

11. J E Mathis, A Goyal, D F Lee, F A List, M Paranthaman, D K Christen, E.D Specht, D M Kroeger and P M Martin, Japan. J. Appl. Phys. 37 (1998) L1379.

12. K. Matsumoto, SeokBeom Kim, I Hirabayashi, T. Watanabe, N. Uno and M. Ikeda, Physica C 330 (2000) 150.

13.Wu X D et al, Appl. Phys. Lett. 67 (1995) 2397.

14. H. C. Freyhardt, J. Weismann, K. Heinemann, J. Hoffmann, J. Dzick, A. Usoskin, F. Garcia-Moreno and S. Sieves, IEEE Trans. Appl. Supercond. 7 (1997) 1426

15. K. Maatsumoto, S. B. Kim, J. G. Wen, I. Hirabayashi, T. Watanabe, N. Uno and M. Ikeda, IEEE Trans. Appl. Supercond. 9 (1999)1539

16. L. H. Germer, R. M. Stern, and A. U. MacRae, Metal surfaces ASM (1963) 287.

Chapter 7. Summary and conclusions

The main effort within the scientific community regarding buffer layers for YBCO thin films is focused on the two main fields: growth on single crystal substrates and coated conductors.

The main objective of studying CeO_2 films on single crystal YSZ substrates was to achieve a deep understanding of the growth process and mechanism in order to better control the properties of films, such as crystallinity, orientation, and surface morphology. Epitaxial CeO_2 films with a thickness of 3nm-1.3μm were analysed. For CeO_2 films deposited in an O_2 atmosphere, there is a critical thickness of about 200nm beyond which the surface roughness rapidly deteriorates. Comparing with the reported results for CeO_2 films on Al_2O_3 substrates, it can be deduced that not only the lattice mismatch between the CeO_2 film and the substrate but also the angle between the axes of the substrate appears to be important parameters for epitaxial growth of thin films.

The shape of the grains forming the background morphology of CeO_2 films deposited in O_2 at 790° is round for a film thickness less than approximately 100nm, and it progressively changes to a rectangular shape as the film thickness increases. The shape of the grains completely change to rectangular and become mutually perpendicular by 900nm thickness. The degree of c-axis orientation is related to the shape of the CeO_2 grains; the more spherical the shape of the grains is, the better the c-axis orientation and the smoothness of the CeO_2 film surface are. This correlation appears to be an intrinsic feature of the CeO_2 film, independent of the type of substrate or the deposition method.

The deposition temperature is the most important deposition parameter for the epitaxial growth of thin films. Each kind of substrate has a definite epitaxial temperature range. The epitaxial temperature range (about 20°C) for growing CeO_2 films on YSZ substrates is relatively wider, which makes it possible to study the effects of different epitaxial temperatures on the surface morphology and growth modes of CeO_2 films. By studying the orientation and the surface morphology of the CeO_2 films deposited at different temperatures, the relationship between epitaxial quality and growth mode could be analysed. The optimum epitaxial growth of a CeO_2 film is layer-by-layer growth from the beginning to the end, and lower quality epitaxial growth is layer-by-layer and then island growth. The growth mode of imperfectly c-axis oriented film is typical island growth. As the islands grow larger and become large outgrowths, the outgrowths prefer to connect to each other to form a network on the surface. For a low quality CeO_2 film which was far from epitaxial, the growth of the film was characterized by the typical terrace-ledge-kink growth mode of cubic crystal.

A systematic study has shown that there are many singular outgrowths, linear outgrowths and linear grooves on the surface of the CeO_2 film with the height of the singular outgrowths much larger than the height of the linear outgrowths and the depth of the grooves. We directly observed that some linear outgrowths are correlated with the polishing scratches on the YSZ substrate, although the thickness of the CeO_2 films is much larger than the depth of the scratches. It is believed that the stress stored at the polishing scratch is the reason for this correlation. The annealing of YSZ substrates at high temperature (>1100°C) can significantly reduce the density of linear outgrowths. On the other hand, the large singular outgrowths are often located along the linear

grooves, which means that the linear grooves store even more stress than the linear outgrowths. The most efficient way of reducing the roughness is to reduce the large singular outgrowths by means of reducing the liner grooves.

We deposited CeO_2 films on single crystal YSZ substrates by PLD using an Ar + 10% H_2 atmosphere. The effects of H_2 on CeO_2 films were studied. Firstly, we found that a deposition using Ar + 10% H_2 can enlarge the epitaxial temperature range, and furthermore, significantly reduce the epitaxial temperature. Pure c-axis CeO_2 films were grown over a substrate temperature range of 775 - 805°C using an O_2 atmosphere, whereas a pure c-axis orientation was obtained for substrate temperatures between 350°C and 775°C using an Ar + 10% H_2 atmosphere. But the c-axis orientation of the CeO_2 films deposited using O_2 is better than that using Ar + 10% H_2 as confirmed by the FWHM of the ω-scans.

Secondly, the morphologies of the CeO_2 films produced in O_2 and Ar+10%H_2 atmospheres and examined by AFM are remarkably different in terms of outgrowth formation. Consequently, the roughness of the former is larger than the roughness of the latter, and it can be deduced that the mobility of species during deposition of a CeO_2 film is smaller when using Ar + 10% H_2 than when using O_2. Epitaxial thin film deposition using an atmosphere including H_2 is quite a new technique and has some advantages, such as low temperature growth and a smooth surface for the CeO_2 films.

A key component of the RABiTS technique is the fabrication of buffer layers on cubic textured Ni substrates. The best buffer layer architecture involves the use of a CeO_2 film

deposited under a reducing atmosphere as the first layer of a multi-layered buffer. In our research, CeO_2 films were deposited on cubic textured Ni substrates by PLD using Ar + 10% H_2. The relationship between the texture of the CeO_2 films and the deposition conditions was analyzed by adjusting deposition temperature, deposition rate, deposition pressure, and the distance between the target and the substrate. The optimum deposition conditions are: deposition temperature 395°C; pulsed laser at 3Hz and 500mJ; Ar + 10% H_2 pressure of 100mTorr. Besides the other parameters, the relative distance between the substrate and the plasma plume was found to be an important parameter. Although the size of the plume depends on the deposition pressure, at about 5 mm distance beyond the plume the deposited species are stoichiometric, and the energy of the deposited species is suitable for epitaxial growth. The degree of the c-axis orientation of the optimum CeO_2 film is about 95.8%, and the FWHM of an XRD ω-scan and a ϕ-scan are 4.9° and 12°, respectively. The shift of angles of ϕ-scans between CeO_2 films and their Ni substrates proves that there is a epitaxial relationship of <110> CeO_2//<100>Ni, which means the CeO_2 principal crystallographic axes are rotated 45° relative to the in-plane Ni (100) axes, i.e. the growth of the CeO_2 film on the cubic textured Ni (100) substrate is in agreement with near-coincidence site lattice match modes. The deposition procedure of first depositing CeO_2 film up to 10nm at 3Hz, then depositing CeO_2 film at 1Hz up to 100nm can reduce the density of cracks and make the cracks narrow.

Biaxially textured NiO films were fabricated by the surface oxidation epitaxy. Three atmospheres, air, flowing oxygen, and flowing Ar +8%O_2, were used in the oxidation process. The optimum deposition process is in flowing oxygen (P_{O2}~ 1 atm) at an

oxidation temperature of 1075°C for 10min. NiO films have strong c-axis and a-b plane orientations. The degree of the c-axis orientation for an optimum film is about 98%, and the FWHM value of a ω-scan for the (111) peak was 14°. XRD pole figures and ϕ-scans were used to investigate the a-b plane texture, and the FWHM value of a ϕ-scan of the NiO(111) peak was 12° about the optimum film. The quality of the biaxially textured NiO films oxidized in air is lower than for oxidation in flowing oxygen. It is impossible to obtain a strong c-axis preference in a NiO film when Ni was oxidized in Ar + 8% O_2.

The morphology and microdefects of NiO films were systematically investigated. Usually the surface quality of the NiO films is lower than for other buffer layers deposited by vacuum deposition methods. A slow cooling rate can reduce the density of microcracks on the surface of NiO by slowly relieving the stress stored in NiO films. The surface roughness is related to the texture of a NiO film; the more (100) oriented the grains are, the smoother the surface of the NiO films is. The high roughness in a NiO layer is also caused by clusters of relatively large NiO grains which form numerous circular spots on the surface of the NiO film. It is thought that these spots are caused by the relief of localised tension in the NiO layer resulting from the difference in volume of a NiO and a Ni unit cells. Decreasing the thickness of the NiO film by shortening the oxidation time can reduce the density of these coarse spots on the surface of the NiO films.

List of publications during PhD study period (from 1999 to 2002)

1. **D. Q. Shi**, M. Ionescu, T. M. Silver, S. X. Dou "Relationship between epitaxial deposition and growth modes of CeO_2 films", accepted by Physica C.
2. **D. Q. Shi**, M. Ionescu, J. McKinnon, W. M. Chen, S. X. Dou, "Relationship between orientation of CeO_2 films and surface morphology", Advances in Cryogenic Engineering 48(2002) 519.
3. **D. Q. Shi**, M. Ionescu, J. McKinnon, W. M. Chen, S. X. Dou, "Research of surface oxidation epitaxy of NiO films on cube textured Ni tapes", Advances in Cryogenic Engineering 48 (2002) 525.
4. J. McKinnon, M. Ionescu, **D. Q. Shi**, and S. X. Dou, " On the growth mechanisms of thin films produced by pulsed laser deposition", Advances in Cryogenic Engineering 48 (2002) 547.
5. W. M. Chen, H. K. Liu, X. K. Fu, Y. C. Guo, **D. Q. Shi**, and S. X. Dou, "Effect of various mechnical deformation techniques on pinning force densities for Ag/Bi-2223 tapes", Advances in Cryogenic Engineering , 48 (2002) 314.
6. **D. Q. Shi**, M. Ionescu, J. McKinnon, and S. X. Dou, "Growth orientation and surface morphology of CeO_2 films deposited by PLD using different deposition atmospheres", Physica C 356 (2001) 304-310.
7. W. M. Chen, **D. Q. Shi**, X. K. Fu, H. K. Liu, T. Silver and S. X. Dou, "Effect of various intermediate deformation techniques on J_c and grain texture for Ag/Bi-2223 tapes", Journal of Superconductivity 14 (2001) 537-541.